ScuDo
Scuola di Dottorato ~ Doctoral School
WHAT YOU ARE, TAKES YOU FAR

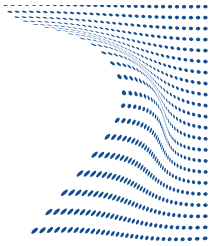

Higher-order layer-wise models for the progressive damage and impact analysis of composite structures

Manish Hassan Nagaraj

Doctoral Dissertation
Doctoral Program in Mechanical Engineering (33° Cycle)

Supervisors
Prof. Erasmo Carrera
Prof. Marco Petrolo

Politecnico di Torino
January 2021

Declaration

I hereby declare that the contents and organisation of this dissertation constitute my own original work and does not compromise in any way the rights of third parties, including those relating to the security of personal data.

Manish Hassan Nagaraj
Politecnico di Torino
January 2021

Acknowledgements

First and foremost, I would like to thank Professor Erasmo Carrera for his guidance throughout the course of my PhD career. His knowledge and insight always motivated and inspired me during my research activities. His door has always been open for me, and I sincerely appreciate him taking the time to help me throughout the course of my research. I would also like to thank Professor Marco Petrolo for his supervision over the past three years. He has always been available to help me whenever I was stuck with a particular problem, and his insights and suggestions went a long way in solving them. I would like to extend my heartfelt gratitude to both of them for presenting me with so many amazing opportunities – well beyond what one would normally expect during their doctoral studies – as well as for their patience, understanding and support, which made my entire journey through the thorny path of a PhD a very enjoyable one.

I would like to thank the amazing people at the MUL2 Group, both current and former, for helping create a fun, enjoyable and productive workplace environment. I would like to gratefully acknowledge the helpful support of Prof. Alfonso Pagani, Dr. Enrico Zappino and Dr. Matteo Filippi. I would like to thank my colleagues Rodolfo Azzara, Iman Babaei, Raj Bharathi, Ehsan Daneshkhah, Nasim Fallahi, Michele Delicata, Daniel Guisa and Marco Enea. I have been extremely fortunate to share an office with some exceptional people over the past three years – Ibrahim Kaleel, Guohong Li, Alberto Garcia de Miguel, Riccardo Augello and Alberto Racionero – and I am very grateful for all the great times we shared. In particular, I am indebted to Ibrahim for all his help and support at the commencement and during the course of my PhD.

I would like to thank Professors Anoush Poursartip and Reza Vaziri for hosting me as a visiting researcher at the Composites Research Network, The University of British Columbia. I would like to especially thank Dr. Hannes Reiner and Prof. Vaziri for their invaluable help during my stay at UBC, leading to a very successful and fruitful research collaboration. I would also like to thank Prof. Brian Falzon for hosting me as a visiting researcher at the Advanced Composites Research Group, Queen's University Belfast.

I would like to thank Project ICONIC – Improving the crashworthiness of composite structures – under whose framework I carried out my research activities. ICONIC has been

funded by the European Union under its Horizon-2020 Research Program, in the form of the Marie Skłodowska-Curie Actions Innovative Training Networks grant (MSCA-ITN-721256), and this funding is gratefully acknowledged.

I am immensely grateful to my parents for providing me with so many opportunities, and ensuring I received a world-class education. None of this would have been possible without their support. Finally, I would like to thank Nikkitha for always being there for me, and for being the light at the end of the tunnel. I wouldn't have succeeded without you, my Goobey Mari.

Abstract

The progressive damage modelling of fibre-reinforced composites is a challenging task owing to the various types of failure mechanisms as well as their interactions. Damage arising due to impact loads on composite structures is of practical interest in the aerospace industry, since such loads can occur frequently during the service life of the composite aerostructure, leading to barely visible impact damage. The use of computational approaches to such a class of problems is likewise challenging, and often involves significant computational effort.

The objective of the present work is the development of a computationally efficient numerical framework for the impact analysis of fibre-reinforced composite structures. The numerical model is developed using higher-order structural theories obtained using the Carrera Unified Formulation (CUF), where additional expansion functions of various types and orders are used to improve the kinematics of classical finite elements. Such an approach leads to 1D and 2D models which provide solutions that are comparable to 3D-FEA, at a fraction of the corresponding computational effort. The current work uses Lagrange polynomials to define the cross-section of 1D elements, and through the thickness of 2D elements, leading to a layer-wise modelling approach. A nonlinear explicit dynamics solver, *CUF-Explicit*, has been developed by combining CUF theories with the central difference explicit time integration scheme. This framework is used for highly nonlinear dynamics problems such as impact analysis. A two-step sequential global-local technique has been developed, which interfaces the CUF-based numerical platform with commercial finite element codes. Various capabilities such as contact modelling and progressive damage modelling have been developed within the CUF framework as part of the present work. The node-to-node and node-to-surface techniques are used for contact surface discretisation, while the contact constraints are enforced using penalty and Lagrange multiplier approaches. Progressive damage of unidirectional fibre-reinforced composites is modelled using the CODAM2 material model, which is based on continuum damage mechanics. A series of numerical assessments are presented to validate and verify the capability of each development.

The contact and damage modelling capabilities are combined in the CUF-Explicit framework, leading to a CUF-based numerical platform for the progressive damage analysis of composites subjected to low-velocity impact loads. A series of numerical assessments are presented for the verification and validation of the proposed numerical approach for impact problems, and demonstrate the capabilities and advantages of layer-wise CUF models, compared to 3D-FEM, for accurate and computationally efficient impact analysis.

Table of contents

List of figures

List of tables

Chapter 1

Introduction

1.1 Motivation

Fibre-reinforced composites are an important class of material systems in the aerospace sector in current time, primarily due to their impressive material properties such as high specific strength and stiffness. Since the introduction of glass and carbon-fibre reinforced plastics in the manufacture of aircraft equipment in the early 1960s [89], the advantages and potential of fibre-reinforced composites, as engineered materials with customisable elastic properties, were recognised and considerable effort was expended to incorporate them in aircraft construction. By the 1980s, several secondary composite aerostructures were developed and deployed into service in civilian aircraft [63]. With improvements in manufacturing processes and increased confidence in the use of fibre-reinforced composites, such materials continue to be used for the construction of a larger proportion of aircraft components, including primary aerostructures. Notable among this are the Boeing 787-Dreamliner and the Airbus A350-XWB, modern civilian aircraft with over 50% of the airframe made of composite materials.

A leading factor towards the widespread adoption of fibre-reinforced composites in the aerospace sector is the alarming rate of climate change over the past century. Modern means of transportation, relying on fossil fuels, contribute greatly to the release of greenhouse emissions [107, 52]. It is estimated that aviation currently contributes to about 2.4% of global CO_2 emissions, with an increase of 32% over the period 2013-2018 [59]. Aviation is also a steadily growing sector, with an average annual growth of over 7%, leading to a doubling of air traffic approximately every 15 years, as per data by the International Civil Aviation Organization (ICAO) [66]. These two factors lead to air transportation being a leading source of greenhouse emissions over the next few decades. Acknowledging this issue, the European Union has set highly ambitious aims calling for the reduction of CO_x and NO_x emissions by 75% and 90%, respectively [48]. The most practical approach of realising these goals,

even partially, is by reducing the aircraft weight so as to reduce its fuel consumption. Fibre-reinforced composites, due to their impressive material properties, are thus ideal materials for the construction of lighter aircraft without compromising on its structural strength and stiffness. Composite airframes can achieve emission reductions of about 20%, based on aircraft life cycle assessments estimates [140]. Advanced composite material systems thus offer an attractive solution to reduce structural weight while ensuring structural integrity of the airframe and hence passenger safety, and this is the reason for their increasing popularity in the aerospace industry.

In spite of the immense popularity of composite materials in the aerospace sector, evidenced by its deployment in modern commercial aircraft, their full potential has not yet been realised. This is primarily due to the complex nature of such material systems, and the uncertainty associated with their complete characterisation under various loading and environmental conditions experienced during the service lifetime of an aircraft. Such issues lead to conservative designs with higher margins of safety, leading to a limited exploitation of composite materials. The aerospace industry typically favours the building block approach [124], which was originally developed for metallic airframes and involves the physical testing of aircraft components from the smallest to largest scales in a sequential manner, and continues the application of this philosophy to composite airframes. Furthermore, current aircraft certification standards rely heavily on experimental testing. Such approaches lead to extensive costs and development times, when applied to composite structures, owing to their significantly large design space. Current practices and design philosophy therefore leads to very limited outcomes for a complete utilisation of composite material systems for aerostructures.

In recent years, the deficiencies of existing design approaches have been addressed, in part, by the use of virtual testing. Such an approach involves the numerical simulation of the composite structure, typically starting from the lowest level of the building block, in an attempt to significantly reduce the amount of physical testing required during the design phase [98]. Virtual testing has been made possible, in large, due to the availability and affordability of computational resources and infrastructures in modern times. Virtual testing of composite structures, as a design tool, requires a good understanding of the various damage and failure mechanisms associated with such material systems, to be able to develop a robust and accurate platform which can be used to preform a reliable analysis. The development of such numerical tools is a very challenging task, and has been the subject of active research for the past few decades. The prevalence of virtual testing tools has also given rise to methodologies such as *Integrated Computational Materials Science and Engineering* (ICME), an integrated approach that combines materials, manufacturing process and structural design to result in optimised design cycles with reduced developmental costs [38, 33]. Another recent methodology is the

concept of *Digital Twin*, which involves the use of high-fidelity simulations that reflect the state of a physical system. The computational models are generally enhanced with data obtained from the physical system, such as real-time sensor data as well as historical data. *Digital Twin* is therefore a technology which aims at a strong integration of the virtual and physical spaces, with the aim of using high-fidelity virtual models to aid in the life-cycle management of the physical system [139]. In addition to its popularity in the manufacturing sector, this technology has strong implications in the aerospace industry, and can be utilised in making better decisions with regards to maintenance of the aerostructure, especially when composite structures are involved, leading to higher safety and reliability over its life-cycle [113, 55].

The largest bottleneck, by far, to the successful adoption of virtual testing methodologies, is the immense computational costs associated with the high-fidelity simulation of industrial-scale structures. Composite damage models necessitate a refined - often 3D - discretisation of the structural domain, primarily to obtain accurate 3D stress and strain fields which constitute important inputs to the nonlinear material models [112]. Such refined discretisations, coupled with computationally intensive damage models, quickly increase the computational overheads required for high-fidelity nonlinear analysis to prohibitive levels, even with the availability of modern computing power. This presents a major drawback in the use of numerical tools during the design phase of composite structures, since lack of sufficient model fidelity leads to a low accuracy of the simulation results. A hard compromise is made between accuracy and computational costs, especially when considering large-scale composite structures, leading to limited success of computational approaches applied to structural design and analysis. This critical issue is well recognised by the research community, and considerable efforts have been made over the last decades to address the issue of computational efficiency, leading to the development of a variety of computational techniques.

Some of the earliest efforts involved the development of global-local techniques, in which the global structure is modelled with low-fidelity, and a high-fidelity discretisation is reserved for the critical regions of the global structure. The domains usually considered for local analysis consist of stress raisers such as holes, cut-outs, concentrated loads etc. In general, two meshes of highly contrasting quality are used to model the global and local regions, and are connected at the interface using a variety of techniques, the most common being tie constraints. Such techniques were popular in the 80s and 90s for linear analysis, when computing power was still severely limited [87, 145–147]. The approach was quickly extended to nonlinear analysis, especially involving material plasticity [95, 39, 74, 54]. While modern computing power is sufficiently advanced to forego such cost-saving techniques to the referenced applications, the global-local approach is still relevant in current times, for progressive damage analysis of composites, as evidenced by the works of [2, 105]. Similar to global-local approaches,

solid/shell coupling techniques have also been successfully employed in the nonlinear analysis of composite structures. In this technique, shells are used to model the global structure, and 3D solid elements are used in the region where nonlinearity is expected to occur. Solid/shell coupling has been used, for instance, to investigate delamination of composite laminates and disbonding of stiffened composite panels by Krueger and co-workers [78, 77].

An alternative philosophy to address issues of computational costs is the use of refined reduced-dimensional numerical models. Classical 1D (beam) theories – such as Timoshenko Beam Theory (TBT) [141] and Euler-Bernoulli Beam Theory (EBBT) [41] – and 2D (plate/shell) theories – such as Reissner-Mindlin plate theory [120] and Kirchhoff theory [76] – often face severe limitations due to the kinematic assumptions made in their formulation. Such shortcomings lead to the poor resolution of kinematic fields in the cross-section of 1D models, and through the thickness of 2D models, rendering them unsuitable for many classes of nonlinear problems which require an accurate 3D resolution of the stress and strain fields. A large body of works available in the literature deals with techniques and approaches to improve the kinematics of 1D and 2D structural theories, often by the use of additional functions to describe the kinematic field. Relatively straightforward means of improving beam kinematics include the introduction of shear correction factors to classical beam theories [142, 60]. A framework for refined beam models developed in recent years is the Generalised Beam Theory (GBT). In this approach, cross-sectional deformation modes are used to describe the kinematics of the beam [128, 129]. This has been successfully extended to the physical and geometrical nonlinear analysis of thin-walled structures [56, 57]. The Variational Asymptotic Beam Section (VABS) approach converts the 3D problem of elasticity into a 1D beam analysis and a 2D cross-section analysis. Asymptotic methods are used to refine the beam theory, using a characteristic parameter derived from the structural geometry (for instance, section thickness) to define the series expansion [29, 157]. Similarly, a significant amount of effort has been expended in the development of refined 2D theories, particularly for the accurate evaluation of through-thickness effects. The First-Order Shear Deformation Theory (FSDT) is a very popular kinematic approximation for the development of 2D elements in commercial finite element software, but is considered to be a classical theory based on the works of Reissner [120] and Mindlin [92]. While this theory takes transverse shear effects into account, it leads to constant shear stresses through the plate thickness, limiting its application to multilayered structures such as composites. Techniques to improve through-thickness kinematics are generally grouped together as Higher-Order Theories (HOT). Significant contributions have been made by Reddy towards the development of higher-order 2D theories [108, 111, 109, 110]. Other 2D theories are available in the works of Palazotto [101].

A generalised framework to generate higher-order structural theories with a variable kinematic description was introduced by Carrera, and is known as the Carrera Unified Formulation (CUF). Originally developed as a method to obtain 2D structural theories [19, 20], CUF has been developed into a numerical framework for the derivation of classical and higher-order 1D (beam) and 2D (plate/shell) structural theories in a fully generalised manner, without the need for ad-hoc modifications of the framework [21]. The formulation makes use of 2D expansion functions and 1D thickness functions to describe the cross-section and thickness kinematics of 1D and 2D models, respectively, leading to a 3D description of field variables and results which are comparable to full 3D models in accuracy, but at significantly reduced computational effort [35].

Over the past two decades, Carrera and co-workers have applied CUF models to a wide variety of structural and multifield problems. The applications include the free vibration analysis of composite beams and plates [156, 158], aeroelastic and flutter analysis of composite aerostructures [43, 9], and problems involving rotordynamics [44, 45]. CUF theories have also been successfully applied to multifield problems [27, 83], such as the thermo-mechanical and hygrothermal analysis of multilayered structures [84, 32], and the dynamic analysis of beams with piezo-patches [159]. Other applications include biomechanical analysis [25], and the analysis of functionally graded compact and thin-walled beams [46, 37]. In recent years, CUF has been extended to the analysis of nonlinear problems, such as geometrically nonlinear and post-buckling analysis [100, 99] and elastoplastic analysis [26, 104], of compact and thin-walled beams. The latest works include the development of a high-fidelity micromechanics framework based on 1D-CUF models [72, 73], and its extension to a multiscale platform for the linear and nonlinear analysis of composite structures [70, 71].

1.2 Aim of the thesis

The current work aims to employ CUF models to investigate composite structures subjected to impact loads. Fibre-reinforced laminates are generally susceptible to transverse loads due to their multi-layered nature. Low-velocity impact of composite aerostructures is thus a critical issue since it results in barely-visible impact damage (BVID), often in the form of internal delaminated plies which are not discernible during visible inspection, and severely reduces the strength and stiffness of composite structures. Such impact events are relatively common during the service life of an aircraft, occurring for instance due to tool drop during maintenance, hail or bird strike while in flight, or even the presence of runway debris during take-off or landing. Low-velocity impact of composite aerostructures is thus an important issue which should be considered during the design and development phases. While numerical techniques have been

successfully used to model impact events and the consequent progressive damage in composite laminates, the problem is highly nonlinear in nature and requires considerable computational effort. Therefore, the primary objective of this thesis is to develop a numerical platform for the progressive damage and low-velocity impact analysis of composite structures in a computationally efficient manner. The explicit time integration scheme is used in the current work, considering the transient dynamic nature of the impact problem. The numerical framework thus combines explicit time integration schemes with higher-order structural theories derived from CUF. The development of such a platform also involves the implementation of contact discretisation and enforcement algorithms, as well as composite material models to account for progressive damage. The following provides an overview of the historic development and state-of-art of computational contact modelling, progressive damage analysis, and low-velocity impact analysis.

Numerical modelling of contact mechanics

The contact phenomenon appears frequently in the field of structural mechanics due to the interaction of various components within a structural system. Applications where contact is relevant include the interaction of systems such as meshing gear teeth, forming processes, indentation tests for material characterisation, as well as impact assessments. In numerical modelling and analysis, it constitutes a class of system nonlinearity, stemming from the change in boundary conditions during the course of interaction of multiple bodies. As such, it is an important aspect for the numerical modelling of impact, since the response of the impacted structure is directly influenced by the contact forces evaluated by the contact algorithm applied in the analysis. Contact is thus an important phenomenon and its accurate modelling constitutes a crucial aspect of the development of reliable tools for numerical structural analysis.

Contact mechanics has been investigated for the past several decades, and significant research effort has been expended, leading to the development of various contact modelling techniques for use in structural analysis. However, contact modelling is one of the most difficult issues in computational mechanics, and remains a topic of current research [106]. Contact models vary significantly in terms of complexity of formulation and implementation, as well as accuracy of the results. The earliest works on the numerical modelling of contact, within the context of the finite element method, relied on node-to-node approaches. In such techniques, contact is enforced at the nodal level, and can thus be implemented in a straight-forward manner in FE codes [51, 133]. Node-to-node contact algorithms constitute the simplest techniques for contact modelling, however they are limited in terms of applicability. Contact enforcement at the nodal level necessitates mesh compatibility of the contacting surfaces, which may be

impractical for structural-scale analysis. They are also limited to geometrically linear analysis due to the underlying kinematic assumptions within the contact algorithm.

The limitations of node-to-node schemes led to the development of surface-based contact models, where contact is enforced over the element surface instead of a discrete nodal point. Applying the concept of surface contact to existing node-based approaches resulted in node-to-surface contact models, where the contact surface pairs are discretised with nodes and surfaces, respectively. Contact is enforced by constraining a contact node from penetrating a target surface [62, 151]. The advantage of such techniques is that nodal compatibility of the contact surfaces is no longer required, leading to greater flexibility in the discretisation of the components of the structure. Classical node-to-surface algorithms are also termed as single-pass techniques, since the only penetration check performed is that between nodes of the contacting body and the surface of the target body. The penetration of the target body nodes through the contact body surface, while possible, is not checked or taken into account. This limitation means that single-pass techniques may not be suitable for certain structural configurations, and can fail the contact patch test [102]. Such limitations to the node-to-surface algorithm can be ameliorated by the use of two-pass techniques, where the algorithm commences identically to the single-pass technique in the first phase, while the definition of the contact and target bodies is interchanged during the second phase, ensuring penetration checks are performed for both contact and target surface nodes. A disadvantage of this approach is that the definition of two sets of constraints for the same contact pair often leads to over-constraining of the system.

The issues related to node-to-surface algorithms led to the use of fully surface-based contact models. Such techniques enforce contact constraints in an integral (weak) manner over the surface of the contacting bodies [130, 102, 160]. An instance of surface-based techniques is the mortar method, originally developed as a method to resolve domain decomposition problems, where the contact surface discretisation of the target body is used in the interpolation of the constraints between the contact pair [106, 7, 90, 47].

A major issue with the numerical analysis of contact problems, especially with finite element techniques, is the necessity of a refined discretisation of the contact surfaces, in order to maintain accuracy of the results. Coarser meshes, even though sufficient for the structural analysis, may introduce errors during contact detection and enforcement, leading to a large divergence from the correct solution. The requirement of such refined discretisation, in addition to the inherent nonlinearity of contact problems, can lead to very high computational costs associated with the analysis. The costs can further increase when other sources of nonlinearity, such as physical or geometrical, are considered. An area of current research is to develop contact models for specific classes of problems so as to reduce the computational costs without compromising on the accuracy of the solution. For instance, Wriggers and co-workers developed extensive

theories and models for the case of beams in contact [131, 152, 161, 85, 94]. Other recent advances in contact modelling approaches involve the use of node-based contact algorithms in combination with various techniques to ensure nodal compatibility of non-matching meshes at the contact interface. This approach to contact modelling aims to take advantage of the simplicity and computational efficiency of node–to-node approaches while simultaneously addressing their limitations. Examples of this approach include the use of variable-node elements [75], using polyhedral elements with sub-dividable polygonal faces [67], and the use of virtual contact elements that can act as an interface between two interacting surfaces [150]. These methods typically convert the original non-matching meshes into equivalent discretisations with compatible contact surfaces, such that node-to-node-contact algorithms may be directly applied.

Progressive damage modelling

The progressive damage analysis of fibre-reinforced composites is an extremely challenging task owing to the various failure modes that occur under the applied loading conditions, as well as the interactions between these modes. Composite failure modes are phenomenologically quite complex, and translating them into a numerical material model, while retaining the physics of the damage progression and its effect on structural integrity, is not straightforward. The numerical modelling of progressive damage in composites is thus an active area of research, as evidenced by the amount of scientific literature generated over the past few decades [97, 116].

Computational models to simulate progressive damage in fibre-reinforced composites are generally classified under two groups: discrete damage models (DDM) and continuum damage models (CDM). Discrete approaches involve explicitly describing matrix cracks within the composite, leading to a physically realistic and accurate representation of the fracture process in composite materials, as well as the interactions of the various failure mechanisms. While such models are highly accurate, they involve significant computational costs. This renders them infeasible for the high-fidelity analysis of industrial-scale composite structures. DDM techniques typically involve the kinematic enrichment of the numerical model to account for the presence of discontinuities across the crack, within the finite element mesh. A popular approach is the use of the eXtended-Finite Element Method (x-FEM). For instance, regularised x-FEM was used to discretely model matrix cracks and their interaction with delamination, and was applied to the strength prediction of open-hole composite laminates [137]. The x-FEM approach to discrete modelling was also utilised for the progressive damage analysis of glass-fibre reinforced composites under tension [143]. The regularised x-FEM technique has been successfully applied to compressive damage analysis, such as static bearing failure of laminated composites [65]. Another technique for discrete modelling involves the use of

cohesive models, based on the Cohesive Zone Method (CZM) originally introduced by Dugdale [40] and Barenblatt [4], to account for both intralaminar matrix cracks as well as delamination between consecutive plies. Discrete damage models based on cohesive interface elements have been applied to the progressive damage analysis of laminates under tensile loads, and the interaction between matrix cracks and delamination [61, 136]. This approach has also been used to model compressive damage, for instance the compression after impact (CAI) analysis of CFRP laminates [123]. Recently, the floating node/phantom node method has emerged as a technique to discretely model discontinuities with the composite laminate [117, 30, 114].

The high computational costs of discrete damage models poses a significant limitation in their use, especially for large-scale composite structures. Continuum damage models, on the other hand, are relatively simple in terms of implementation, and have lower computational overheads when compared to fully discrete approaches. For this reason, composite material models based on continuum damage mechanics are currently very prevalent in the literature dealing with the progressive damage analysis of composites. In continuum-based techniques, the cracks within the matrix of the composite are smeared out within the volume of the finite element, and their effects are represented by damage parameters which affect the stiffness of the material point within the global structure. The process of smearing out the crack ensures continuity of the mesh, thereby avoiding computationally expensive discontinuity handling techniques, and leading to an improvement in the efficiency of continuum models. However, a major drawback of the technique is a strong mesh dependency, since the crack width depends on the height of the finite element. The issue of mesh dependency is generally addressed via the use of the crack-band theory [6], where the constituent fracture energy is scaled using a suitable length parameter, usually derived from the dimensions of the finite element.

From initial works on continuum damage modelling, such as those of Ladaveze et al. [79] and Matzenmiller et al. [88], this approach has been applied to a wide set of applications in the composite structural analysis, ranging from the study of size-effects in composite laminates [15], to the failure analysis of CFRP pressure vessels [144]. The inherent issues with computational compressive damage modelling, as well as the overheads involved, renders CDM-based models the predominant approach for the progressive damage analysis of composite structures loaded in compression [134, 1, 122]. The most popular approach for the progressive damage analysis of composite laminates, while judiciously considering the compromise between costs and accuracy, is a mixed-approach where damage within the individual ply is modelled using continuum damage mechanics-based approaches, whereas delamination between plies is modelled using cohesive interface elements. Such an approach has been used to investigate progressive damage and delamination growth in hybrid composite joints [53], and for the failure analysis of notched composite laminates [132].

Low-velocity impact modelling

The issue of low-velocity impact and the resulting barely-visibly impact damage (BVID), especially delamination growth, makes it a very important design problem from a practical standpoint. For this reason, the investigation of composite laminates subjected to low-velocity impact has been an active area of research over the past decade. While a considerable amount of experimental work has been done in the past to evaluate composite behaviour under impact loads [16, 31, 3, 86], the difficulties and expense of detailed test campaigns render computational approaches an attractive alternative tool for low-velocity impact investigations. Numerical models for impact analysis are generally grouped according to the type of material model used to evaluate damage within the composite. Discrete damage models typically use cohesive interface elements to account for intralaminar matrix cracks, as well as for delamination progression. The advantage of this approach is that it can accurately model the interactions between matrix cracks and delamination [81, 36], which is a crucial issue when considering progressive damage and failure of composites under impact loads. A numerical framework based on discrete interface elements was developed by Bouvet and co-workers to accurately model low-velocity impact problems [11, 12]. Other examples of discrete models for impact analysis include [126, 135].

The prohibitive computational costs of discrete modelling approaches lead to the popularity of continuum damage mechanics-based damage models for impact analysis. CDM approaches are usually paired with cohesive interlaminar surfaces to model delamination, resulting in a combined approach which is capable of accurately modelling intra- and interlaminar damage in a cost-effective manner. Several works concerning the impact analysis of composite laminates using this approach, as well as its extension to compression after impact (CAI), have been reported in the literature in recent years [58, 42, 138, 127]. In spite of the relative computational efficiency of CDM approaches, the overall computational time for impact analysis can still be rather prohibitive, on the order of several hours to several days on modern HPC systems [58, 138]. Several techniques have been used to reduce the computational costs of such analyses, chiefly via the use of global/local method. For instance, Riccio and co-workers used 3D discretisations of differing refinement to model the global structure and the local impact region, using tie constraints to link the two disparate meshes at the interface [121, 17]. Sun and Hallett used a similar approach, where the global structure is meshed with low-fidelity shell elements while the the impact region is meshed with high-fidelity 3D solid elements, with tie constraints to connect the two meshes [135].

The primary objective of the present work is to investigate the capabilities of the Carrera Unified Formulation (CUF) as a computationally efficient numerical platform for the progressive damage analysis of fibre-reinforced composites subjected to impact conditions. The combined

damage modelling approach is used, where intralaminar damage is evaluated using continuum damage mechanics-based material models, while delamination is modelled by the insertion of cohesive elements between consecutive plies. The present work utilises the COmposite DAMage (CODAM) material model to evaluate damage initiation and propagation. The CODAM model was initially developed as a sublaminate-level material model based on continuum damage mechanics [148], and successfully used in the analysis of braided composite tubes [91]. The 2^{nd} generation CODAM model, CODAM2, considers equivalent stress-strain responses in the principal ply directions to determine fracture behaviour at the laminate level [50, 49]. Recent versions of the CODAM2 model use a stress-based formulation where failure initiation is determined using Hashin failure theory, and is implemented as the MAT219 material card in the commercial FE solver LS-DYNA [115, 125]. The stress-based CODAM2 model is the version which has been implemented in the CUF framework as part of the current work. Cohesive elements are used to model delamination onset and growth, following the mixed-mode cohesive constitutive formulation developed by Camanho and co-workers [14], and has been successfully integrated with 1D-CUF models for the investigation of delamination in composite laminates under static loading [69].

1.3 Outline

The thesis is composed of the following chapters which describe the development of a platform, using higher-order layer-wise structural numerical models, for the progressive damage analysis of fibre-reinforced composite laminates subjected to low-velocity impact.

Chapter 2 introduces the Carrera Unified Formulation (CUF), and describes an implicit nonlinear framework based on the Newton-Raphson scheme, as well as an explicit dynamics solver based on explicit time integration, where the structural modelling exploits higher-order beam and plate theories generated using CUF. A free-edge analysis of a stiffened composite panel is also presented to motivate the advantages of higher-order structural models in accurate stress analysis, when compared to standard 3D FE approaches.

Chapter 3 describes a 2-step global-local approach wherein CUF models are interfaced with the commercial FE solver ABAQUS. A detailed description of the global-local process is provided, where displacements are extracted from low-fidelity ABAQUS models of the global structure, and applied as prescribed boundary conditions to the high-fidelity local CUF model, to obtain accurate and computationally efficient results in the region of interest. Both linear and nonlinear problems are investigated with this approach to demonstrate its advantages.

Chapter 4 focuses on the development of contact modelling capabilities within the CUF framework. In particular, the node-to-node and node-surface contact discretisation schemes

are described, with Lagrange multiplier and penalty methods used to enforce the contact constraints. The combination of node-to-node discretisation and the penalty method is applied to a set of static contact problems and solved using implicit solution schemes, while the node-surface contact discretisation with Lagrange multiplier enforcement is applied to dynamic contact/impact problems and is solved using explicit time integration. The forward increment Lagrange multiplier technique, required when Lagrange contact constraints are used in explicit schemes, is also described in detail.

Chapter 5 describes progressive damage analysis in CUF using continuum damage mechanics-based approaches. A detailed description of the CODAM2 material model and its formulation is provided, for both tensile and compressive progressive damage. Techniques such as the use of bilinear fibre softening curves for the accurate damage modelling of composites loaded in compression, is described in detail. A series of validation cases are presented, of composite laminates loaded in tension and in compression, to demonstrate the capabilities of the CUF models.

Chapter 6 deals with the CUF approach to handling impact problems. Specifically, the implementation and development outcomes of Chapter 4 and Chapter 5 within an explicit setting, i.e. CUF-Explicit, are combined to result in a numerical platform based on higher-order structural theories for the progressive damage analysis of fibre-reinforced composites subjected to low-velocity impact. The verification and validation of the CUF platform is demonstrated using reference numerical and experimental data.

Chapter 7 presents a summary of the present work, and some concluding remarks to highlight the major outcomes of the thesis. Some research avenues are proposed as topics for future investigations, based on the developments achieved during the scope of the current work.

Appendix A lists the journal articles and conference proceedings which resulted during the course of the present work.

Chapter 2

Higher-order theories for structural analysis

This chapter introduces the Carrera Unified Formulation (CUF) and its application in the development of higher-order 1D models within a finite element framework. The various classes of interpolation functions, used in CUF to enrich the structural kinematics, are described in detail. A numerical example is presented to motivate the need for high-order theories for the analysis of composite structures, which highlights the capabilities of CUF models. The solution techniques used for nonlinear analysis, both implicit and explicit, are described in detail.[1]

2.1 The Carrera Unified Formulation

The Carrera Unified Formulation (CUF) is a generalised hierarchical framework to derive higher-order 1D (beam) and 2D (plate, shell) structural theories. The fundamental concept of the framework is the introduction of expansion functions, in addition to standard finite element interpolation functions, to enrich the kinematic description of the beam cross-section and plate/shell thickness. This approach leads to 1D and 2D CUF models which are similar to 3D-FEA in terms of solution accuracy, but require considerably less computational effort [21]. The current section provides a brief description of the formulation for the case of 1D models, while the 2D formulation can be developed analogously. Consider a generalised beam element, as shown in Fig. 2.1. Considering 1D-CUF models, first introduced by Carrera and Giunta

[1] Parts of this chapter have been published in the following:

1. de Miguel, A. G., Kaleel, I., Nagaraj, M. H., Pagani, A., Petrolo, M. & Carrera, E. (2018). Accurate evaluation of failure indices of composite layered structures via various FE models. Composites Science and Technology, 167, 174-189.

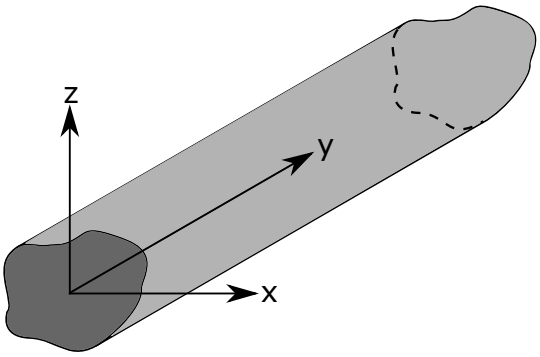

Fig. 2.1 A generalised beam element oriented along the y-axis.

[23], the displacement field of the beam is defined as

$$\mathbf{u}(x,y,z) = F_\tau(x,z)\mathbf{u}_\tau(y), \tau = 1,2,\ldots M \tag{2.1}$$

where $F_\tau(x,z)$ is the expansion function which acts on the beam section, and defines the cross-section kinematics of the numerical model. M denotes the number of polynomial terms in the expansion function, while $\mathbf{u}_\tau(y)$ denotes the generalised axial displacements. The use of expansion functions at the cross-section of 1D models results in a full 3D displacement field, and subsequently a 3D strain and stress tensor. The parameters F_τ and M are provided by the user as inputs, and define the structural theory used in the model. A variety of basis functions, such as exponential, trigonometric, or harmonic, can be used as expansion functions without the need for ad-hoc modification of the formulation [22]. Two classes of expansion functions have emerged in recent years as ideal choices due to their various capabilities - the Taylor Expansion (TE) [24] and Lagrange Expansion (LE) classes [28]. The current works exploits these two classes, with a specific focus on the use of the LE class for nonlinear structural analysis. The following sections provide a detailed description of the TE and LE classes.

2.1.1 Taylor Expansion

The Taylor Expansion (TE) class considers the Taylor series of the kind $x^i z^i$ as cross-sectional expansion functions F_τ. This results in a hierarchical basis function, where the polynomial order N is user-defined. For instance, the first-order Taylor expansion (N=1), containing 9 terms, is given below

$$\begin{aligned} u_x &= u_{x_1} + xu_{x_2} + zu_{x_3} \\ u_y &= u_{y_1} + xu_{y_2} + zu_{y_3} \\ u_z &= u_{z_1} + xu_{z_2} + zu_{z_3} \end{aligned} \tag{2.2}$$

Classical beam theories can be obtained as special cases of the first-order theory by the selective removal of certain terms. For instance, Timoshenko Beam Theory (TBT), containing 5 terms, is obtained from Eq. 2.2 as

$$\begin{aligned} u_x &= u_{x_1} \\ u_y &= u_{y_1} + x u_{y_2} + z u_{y_3} \\ u_z &= u_{z_1} \end{aligned} \tag{2.3}$$

The use of TE leads to the Equivalent Single Layer (ESL) approach to modelling of laminated composites. Further details of the use of Taylor Expansion in CUF is available in [24].

2.1.2 Lagrange Expansion

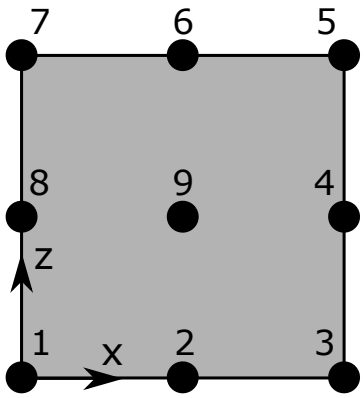

Fig. 2.2 The L9 9-node quadratic cross-section Lagrange element.

The Lagrange Expansion (LE) class uses Lagrange polynomials as the basis functions to describe the cross-section kinematics. In CUF, LE polynomials are implemented in the form of cross-section elements, termed Ln, where n denotes the number of nodes in the element. As an example, the 9-node quadratic Lagrange expansion element (L9) is shown in Fig. 2.2. The corresponding nodal interpolation functions, based on Lagrange polynomials, are written as

$$\begin{aligned} u_x &= \sum_{i=1}^{9} F_i(x,z) \cdot u_{x_i}(y) \\ u_y &= \sum_{i=1}^{9} F_i(x,z) \cdot u_{y_i}(y) \\ u_z &= \sum_{i=1}^{9} F_i(x,z) \cdot u_{z_i}(y) \end{aligned} \tag{2.4}$$

where i refers to the node number, and $u_{x_i}, u_{y_i}, u_{z_i}$ are the translational degrees of freedom for the node i. The use of LE functions results in purely translational degrees of freedom in the global system. This offers an advantage over TE class, where higher-order degrees of freedom do not have a physical meaning. Furthermore, local refinement of the cross-section is possible by increasing the number of Lagrange elements. The use of LE leads to the Component-Wise (CW) approach, where individual components of the structure can be explicitly modelled. For the case of laminated composites, this leads to a Layer-Wise (LW) model, where each lamina is modelled with one or more Lagrange elements. Further details on the application of Lagrange polynomials to improve cross-section kinematics in CUF is available in [28].

2.2 Finite Element Formulation

The stress and strain tensors are written in vector notation as

$$\begin{aligned} \boldsymbol{\sigma} &= \{\sigma_{xx}, \sigma_{yy}, \sigma_{zz}, \sigma_{xy}, \sigma_{xz}, \sigma_{yz}\} \\ \boldsymbol{\varepsilon} &= \{\varepsilon_{xx}, \varepsilon_{yy}, \varepsilon_{zz}, \varepsilon_{xy}, \varepsilon_{xz}, \varepsilon_{yz}\} \end{aligned} \tag{2.5}$$

where $\boldsymbol{\varepsilon}$ is the linear strain tensor. The strain-displacement relation is

$$\boldsymbol{\varepsilon} = \mathbf{B} \cdot \mathbf{u} \tag{2.6}$$

with $\mathbf{B}$, the linear differentiation operator, defined as

$$\mathbf{B} = \begin{bmatrix} \frac{\partial}{\partial x} & 0 & 0 \\ 0 & \frac{\partial}{\partial y} & 0 \\ 0 & 0 & \frac{\partial}{\partial z} \\ \frac{\partial}{\partial y} & \frac{\partial}{\partial x} & 0 \\ \frac{\partial}{\partial z} & 0 & \frac{\partial}{\partial x} \\ 0 & \frac{\partial}{\partial z} & \frac{\partial}{\partial y} \end{bmatrix}$$

The constitutive relation is given as

$$\boldsymbol{\sigma} = \bar{\mathbf{C}}\boldsymbol{\varepsilon} \tag{2.7}$$

where $\bar{\mathbf{C}}$ is the 6×6 material matrix. In case of material nonlinearity, the material model provides the material matrix based on the system state. Standard 1D finite elements, with nodal shape functions N_i, are used to discretise the beam along its axis. This leads to the following

3D definition of the displacement vector:

$$\mathbf{u}(x,y,z) = F_\tau(x,z)N_i(y)\mathbf{u}_{\tau i} \tag{2.8}$$

The use of 2D expansion functions $F_\tau(x,z)$ in combination with 1D shape functions $N_i(y)$ is schematically shown in Fig. 2.3. The choice of the axial shape functions N_i is independent of the choice of the cross-sectional expansion functions F_τ, leading to significant flexibility in the structural modelling. The present work employs 1D finite elements based on standard Lagrange polynomials of various polynomial orders. The available 1D elements, along with the nodal interpolation functions, are shown in Fig. 2.4.

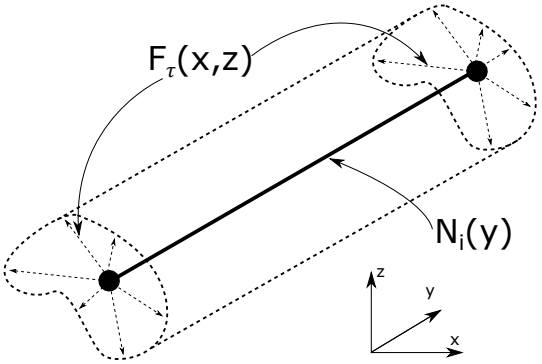

Fig. 2.3 1D CUF model within the finite element framework.

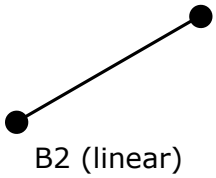

$$\left.\begin{aligned} N_1 &= \tfrac{1}{2}(1-\xi) \\ N_2 &= \tfrac{1}{2}(1+\xi) \end{aligned}\right\} \begin{aligned} \xi_1 &= -1 \\ \xi_2 &= 1 \end{aligned}$$

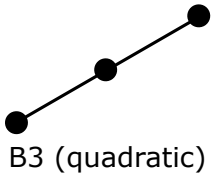

$$\left.\begin{aligned} N_1 &= \tfrac{1}{2}\xi(1-\xi) \\ N_2 &= -(1-\xi)(1+\xi) \\ N_3 &= \tfrac{1}{2}\xi(1+\xi) \end{aligned}\right\} \begin{aligned} \xi_1 &= -1 \\ \xi_2 &= 0 \\ \xi_3 &= 1 \end{aligned}$$

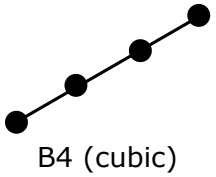

$$\left.\begin{aligned} N_1 &= -\tfrac{9}{16}(\xi+\tfrac{1}{3})(\xi-\tfrac{1}{3})(\xi-1) \\ N_2 &= \tfrac{27}{16}(\xi-1)(\xi-\tfrac{1}{3})(\xi+1) \\ N_3 &= -\tfrac{27}{16}(\xi+1)(\xi+\tfrac{1}{3})(\xi-1) \\ N_4 &= \tfrac{9}{16}(\xi+\tfrac{1}{3})(\xi-\tfrac{1}{3})(\xi+1) \end{aligned}\right\} \begin{aligned} \xi_1 &= -1 \\ \xi_2 &= -1/3 \\ \xi_3 &= 1/3 \\ \xi_4 &= 1 \end{aligned}$$

Fig. 2.4 Beam elements along with their nodal shape functions [5].

Weak form of the boundary value problem

The equilibrium equation, considering the balance of linear momentum, is written as

$$\sigma_{ij,j} + b_i = \rho \ddot{u}_i, \forall\, i,j = 1,2,3 \tag{2.9}$$

where $\boldsymbol{\sigma}$ is the Cauchy stress tensor, $\mathbf{b}$ is the vector of body forces, ρ is the mass density and $\ddot{\mathbf{u}}$ is the second partial time derivative of the displacement. According to the Principle of Virtual Displacements (PVD), for a body in equilibrium, the total internal virtual work is equal to the total external virtual work [5]. This is written in equation form as

$$\int_\Omega \delta u_i \rho \ddot{u} d\Omega + \int_\Omega \delta \varepsilon_{ij} \sigma_{ij} d\Omega = \int_\Omega \delta u_i b_i d\Omega + \int_\Gamma \delta u_i t_i d\Gamma \tag{2.10}$$

where the terms on the left hand side refer to the virtual variation of the work due to inertial loads and internal strain energy, respectively, while the term on the right hand side is the virtual variation of the work due to external loads. The virtual variation of the internal strain energy can be written in matrix form as

$$\delta L_{int} = \int_V \delta \boldsymbol{\varepsilon} \boldsymbol{\sigma} dV = \int_V \delta \boldsymbol{\varepsilon} \bar{\mathbf{C}} \boldsymbol{\varepsilon} dV \tag{2.11}$$

The linear strain-displacement relation (Eq. 2.6) is reformulated using Eq. 2.8 as

$$\boldsymbol{\varepsilon} = \mathbf{B}_{\tau i} \mathbf{u}_{\tau i} \tag{2.12}$$

where

$$\mathbf{B}_{\tau i} = \begin{bmatrix} N_i F_{\tau,x} & 0 & 0 \\ 0 & N_{i,y} F_\tau & 0 \\ 0 & 0 & N_i F_{\tau,z} \\ 0 & N_i F_{\tau,z} & N_{i,y} F_\tau \\ N_i F_{\tau,z} & 0 & N_i F_{\tau,x} \\ N_{i,y} F_\tau & N_i F_{\tau,x} & 0 \end{bmatrix}$$

Similarly, the virtual form of the strain tensor is expressed as

$$\delta \boldsymbol{\varepsilon} = \mathbf{B}_{sj} \delta \mathbf{u}_{sj} \tag{2.13}$$

This leads to the following form of the virtual variation of the internal strain energy

$$\delta L_{int} = \delta \mathbf{u}_{sj} \int_V \mathbf{B}_{sj}^T \bar{\mathbf{C}} \mathbf{B}_{\tau i} dV\ \mathbf{u}_{\tau i} \tag{2.14}$$

$$\delta L_{int} = \delta \mathbf{u}_{sj} \mathbf{k}_{ij\tau s} \mathbf{u}_{\tau i} \tag{2.15}$$

where, $\mathbf{k}_{ij\tau s}$ is called the Fundamental Nucleus (FN) of the structural stiffness matrix, and is a 3×3 matrix of the following form

$$\mathbf{k}_{ij\tau s} = \begin{bmatrix} k^{xx}_{\tau sij} & k^{xy}_{\tau sij} & k^{xz}_{\tau sij} \\ k^{yx}_{\tau sij} & k^{yy}_{\tau sij} & k^{yz}_{\tau sij} \\ k^{zx}_{\tau sij} & k^{zy}_{\tau sij} & k^{z}_{\tau sij} \end{bmatrix} \tag{2.16}$$

As an example, the first two terms of the FN are expanded below

$$\begin{aligned} k^{xx}_{\tau sij} = &(\bar{C}_{11} F_{s,x} N_j + \bar{C}_{51} F_{s,z} N_j + \bar{C}_{61} F_s N_{j,y}) F_{\tau,x} N_i \\ &+(\bar{C}_{15} F_{s,x} N_j + \bar{C}_{55} F_{s,z} N_j + \bar{C}_{65} F_s N_{j,y}) F_{\tau,z} N_i \\ &+(\bar{C}_{16} F_{s,x} N_j + \bar{C}_{56} F_{s,z} N_j + \bar{C}_{66} F_s N_{j,y}) F_{\tau} N_{i,y} \end{aligned} \tag{2.17}$$

$$\begin{aligned} k^{xy}_{\tau sij} = &(\bar{C}_{12} F_{s,x} N_j + \bar{C}_{52} F_{s,z} N_j + \bar{C}_{62} F_s N_{j,y}) F_{\tau} N_{i,y} \\ &+(\bar{C}_{14} F_{s,x} N_j + \bar{C}_{54} F_{s,z} N_j + \bar{C}_{64} F_s N_{j,y}) F_{\tau,z} N_i \\ &+(\bar{C}_{16} F_{s,x} N_j + \bar{C}_{56} F_{s,z} N_j + \bar{C}_{66} F_s N_{j,y}) F_{\tau,x} N_i \end{aligned} \tag{2.18}$$

The remaining terms of the FN can be derived in an analogous manner. Following the structure of the derivation of the virtual internal strain energy, the virtual variation of the inertial loads can be defined as

$$\delta L_{ine} = \delta \mathbf{u}_{sj} \int_V N_j F_s \rho \mathbf{I} N_i F_\tau dV \ddot{\mathbf{u}}_{\tau i} = \delta \mathbf{u}_{sj} \mathbf{m}_{\tau sij} \ddot{\mathbf{u}}_{\tau i} \tag{2.19}$$

where $\mathbf{m}_{\tau sij}$ is the fundamental nucleus of the mass matrix, and can be evaluated in a manner similar to that of the structural stiffness. The virtual variation of the work due to external loads is defined as

$$\delta L_{ext} = \int_V \delta \mathbf{u}^T \mathbf{g} dV + \int_S \delta \mathbf{u}^T \mathbf{q} dS + \int_l \delta \mathbf{u}^T \mathbf{r} dl + \delta \mathbf{u}^T P_m \tag{2.20}$$

where $\mathbf{g}$ is the body force acting on the volume V, $\mathbf{q}$ is the surface force acting on the surface S, $\mathbf{r}$ is the line force acting on a line l, and P_m is a point force acting at a point m. The equation can be rewritten as

$$\delta L_{ext} = \delta \mathbf{u}_{sj} \left\{ \int_V N_j F_s \mathbf{g} dV \int_S N_j F_s \mathbf{q} dS + \int_l N_j F_s \mathbf{r} dl + N_j F_s P_m \right\} = \delta \mathbf{u}_{sj} \mathbf{p}_{sj} \tag{2.21}$$

The global stiffness and mass matrices, as well as the global force vector, can be obtained by the assembly of the corresponding FN, by looping over the indices $\tau, s =, 2, \ldots M$ and

$i, j = 1, 2, \ldots p+1$, as shown below

$$\mathbf{K} = \sum_{n=1}^{n_{elem}} \sum_{i,j=1}^{p+1} \bigcup_{\tau,s=1}^{M} \mathbf{k}_{\tau sij} \tag{2.22}$$

$$\mathbf{M} = \sum_{n=1}^{n_{elem}} \sum_{i,j=1}^{p+1} \bigcup_{\tau,s=1}^{M} \mathbf{m}_{\tau sij} \tag{2.23}$$

$$\mathbf{P} = \sum_{n=1}^{n_{elem}} \sum_{j=1}^{p+1} \bigcup_{s=1}^{M} \mathbf{p}_{sj} \tag{2.24}$$

where **K**, **M** and **P** are the global stiffness matrix, mass matrix, and external force vector, respectively. The symbol $\sum$ denotes the assembly operation that sums the contribution of the finite elements, and $\bigcup$ is the analogous CUF assembly operator. The assembly operation used to obtain the global stiffness matrix, starting from the 3×3 FN, is schematically shown in Fig. 2.5. A detailed description of CUF structural theories and their finite element formulation, along with the role of the FN in the global assembly procedure, is discussed in [21].

2.3 Motivation for the use of high-order structural theories

Certain classes of structural problems, notably the analysis of fibre-reinforced laminates, often necessitate a full 3D analysis to obtain an accurate 3D stress field. The complete stress tensor is often required for progressive damage and delamination analysis of composite structures, and as such, tend to have significant computational costs when modelled using standard numerical approaches. The use of 3D-FEA is particularly demanding, due to aspect ratio constraints of the finite element. In such cases, CUF-based higher-order structural theories offer a computationally-efficient alternative to standard numerical modelling approaches. CUF models are able to resolve the full 3D stress field with an accuracy approaching that of 3D-FE, at vastly reduced computational costs. The use of Lagrange Expansion (see Section 2.1.2) leads to a layer-wise modelling approach, which is well-suited for the case of composite laminates. The capabilities and efficiency of 1D-CUF models, compared to 3D finite elements, is demonstrated via the following numerical example.

The structure consists of a composite panel stiffened with a composite trapezoidal stringer, as shown in Fig. 2.6. The geometry of the structure is derived from the works of Bisagni et al. [10]. The structure spans 240 mm in length, and is subjected to tensile loading. The material system used in the assessment is IM7/8552 unidirectional carbon-fibre reinforced plastic, whose elastic properties are given in Table 2.1. The skin is constructed of a 1 mm thick

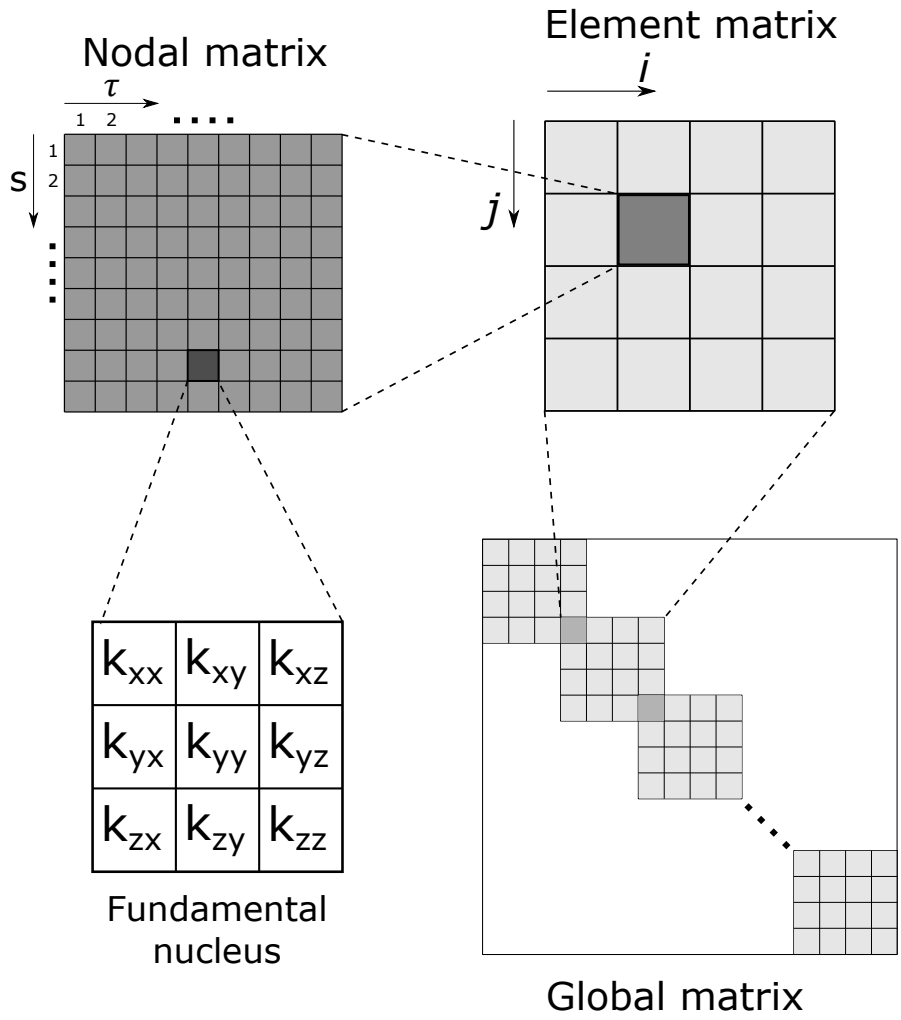

Fig. 2.5 Assembly of the global stiffness matrix from the fundamental nucleus.

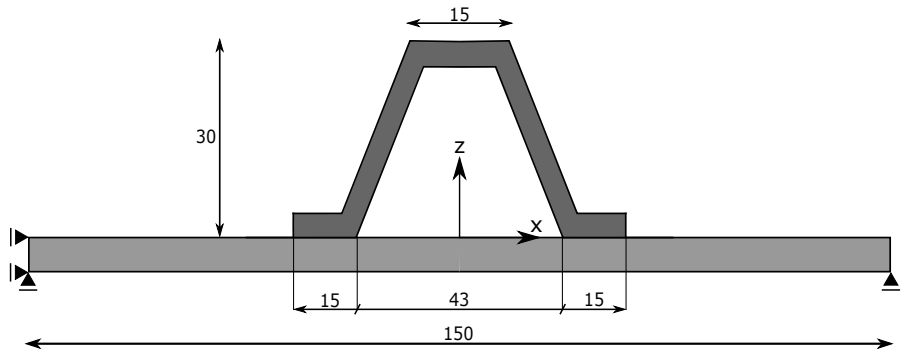

Fig. 2.6 Sectional view of the composite panel stiffened with a trapezoidal stringer.

quasi-isotropic $[45/90/-45/0]_s$ laminate, while the stiffener has a $[-45/0/45/0/45/0/-45]$ stacking sequence with a 0.875 mm laminate thickness. The objective of the current assessment is the evaluation of free-edge stresses of the composite structure, and to compute the failure indices at the free-edge, following Hashin's criteria for failure initiation[64]. The mixed-mode quadratic criterion is used to evaluate a delamination index [13]. The analysis is performed on the composite structure using 1D-CUF models, and reference 3D-FE models are developed in ABAQUS for comparison. Model information of the various approaches, including details on the discretisation and analysis times, is given in Table 2.2.

The free-edge interlaminar stresses through the thickness of the composite panel and stiffener,

Table 2.1 Mechanical properties of the IM7/8552 material system.

Material	E_1 [GPa]	E_2 [GPa]	E_3 [GPa]	G_{12} [GPa]	G_{13} [GPa]	G_{23} [GPa]	ν_{12}	ν_{13}	ν_{23}
IM7/8552	165.0	9.0	9.0	5.6	5.6	2.8	0.34	0.34	0.5

Table 2.2 Model details for the free-edge analysis of the stiffened composite panel.

Model	Discretization	DOF	CPU Time [s]
CUF-LW$_1$	10 B4 - 355 L9 (1 L9 per ply)	142,476	161
CUF-LW$_2$	10 B4 - 710 L9 (2 L9 per ply)	277,326	478
ABQ-3D$_1$	705,600 C3D8 (1 elem per ply)	2,422,749	760
ABQ-3D$_2$	1,411,200 C3D8 (2 elem per ply)	4,560,150	3,764

i.e. the point A [x = 36.5, y = 120.0], are shown in Fig. 2.7, while the matrix tension and delamination failure indices at the same point are plotted in Fig. 2.8. Similarly, the interlaminar stress components and failure indices at the free-edge of the panel, i.e. the point B [x = 75.0, y = 120.0], are in Fig. 2.9 and Fig. 2.10, respectively. The following comments are made:

1. The 1D-CUF models are able to accurately capture the interlaminar stress fields through the thickness, at the free-edge of the composite, as seen in Fig. 2.7 and Fig. 2.9.

2. The lack of sufficient through-thickness refinement in the 3D-FE models leads to an under-prediction of the interlaminar stresses, and consequently the failure indices (see Fig. 2.8 and Fig. 2.10), at the interface between the composite panel and stiffener.

3. The 1D-CUF models are about 16x smaller in terms of computational size (DOF), and need approximately 7x less analysis time than refined 3D-FE models, for corresponding solution accuracy. This demonstrates the capability and computational efficiency of 1D-CUF models in the accurate stress analysis of laminated composite structures.

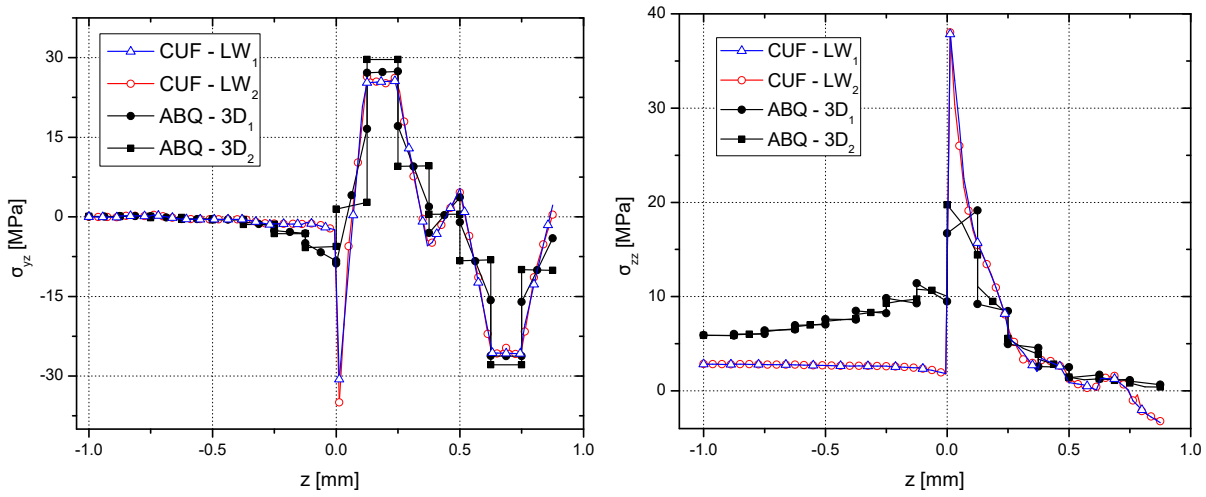

(a) σ_{yz} (b) σ_{zz}

Fig. 2.7 Free-edge interlaminar stresses through the thickness of the stiffener and panel.

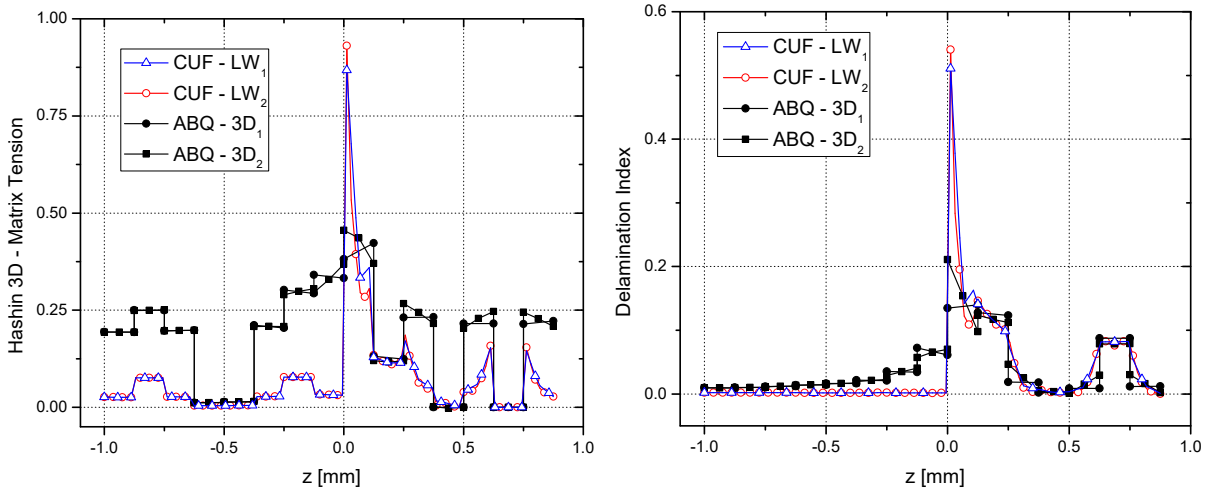

(a) Hashin 3D - Matrix Tension (b) Delamination Index

Fig. 2.8 Through-thickness failure Indices at the free-edge of the panel and stiffener (point A).

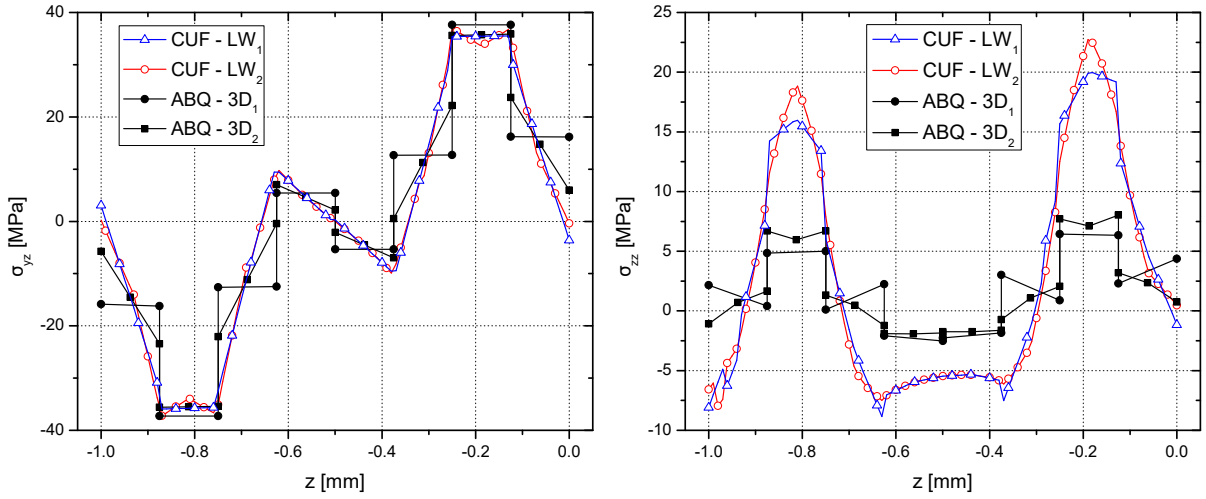

(a) σ_{yz} (b) σ_{zz}

Fig. 2.9 Free-edge interlaminar stresses through the thickness of the composite panel.

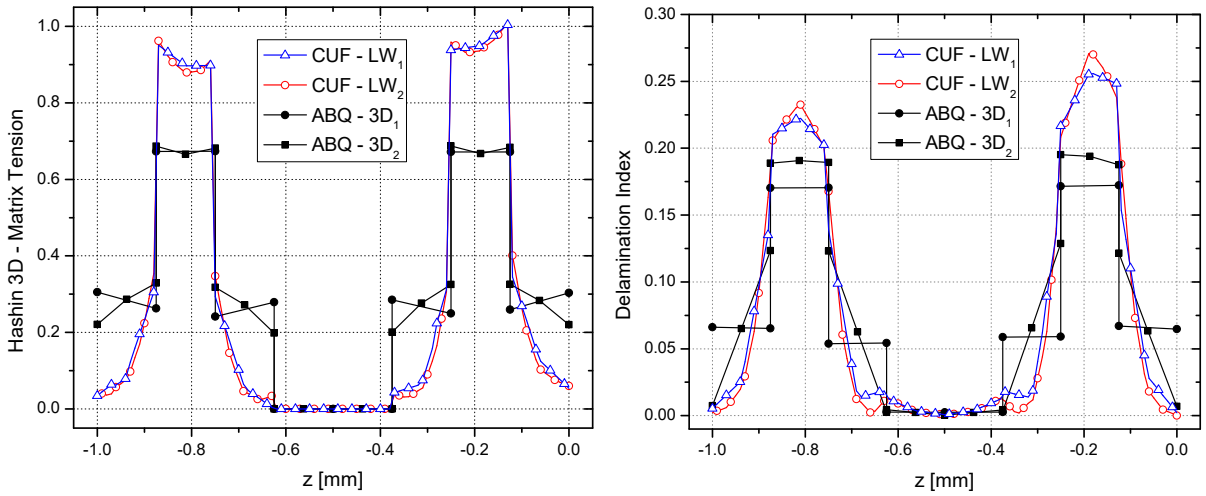

(a) Hashin 3D - Matrix Tension (b) Delamination Index

Fig. 2.10 Through-thickness failure Indices at the free-edge of the composite panel (point B).

2.4 Nonlinear structural analysis in CUF

Material and structural behaviour is often nonlinear in nature, and the accurate numerical simulation of such materials and structures necessitates nonlinear analysis. Approaches for the solution of nonlinear problems can be broadly classified under two categories - (i) Implicit methods and (ii) explicit methods. The following sections provide a detailed description of both analysis approaches as implemented within the CUF framework.

2.4.1 Implicit solution techniques

Implicit solution techniques are effective methods to solve quasi-static nonlinear structural problems, such as those involving material and/or geometrical nonlinearity, as well as problems concerning nonlinear boundary conditions, such as contact. The quasi-static nature leads to the following form of the global governing equation

$$\mathbf{K}(\mathbf{u}) \cdot \mathbf{u} = \mathbf{F}_{ext} \tag{2.25}$$

where $\mathbf{K}(\mathbf{u})$ is the nonlinear global stiffness matrix which depends on the type of nonlinearity present in the system, while $\mathbf{u}$ and $\mathbf{F}_{ext}$ are the global displacement and external force vectors, respectively. The equilibrium equation, neglecting dynamic forces, is given by

$$\mathbf{F}_{int}(\mathbf{u}) - \mathbf{F}_{ext} = \mathbf{0} \tag{2.26}$$

where $\mathbf{F}_{int}(\mathbf{u})$ is the internal force vector, which is a function of the global displacement vector. Based on the notation used in Section 2.2, Eq. 2.26 can be written in terms of CUF fundamental nuclei as

$$\mathbf{k}^{s}_{ij\tau s}\mathbf{u}_{\tau i} - \mathbf{p}_{js} = 0 \tag{2.27}$$

where $\mathbf{k}^{s}_{ij\tau s}$ is the FN of the secant stiffness matrix. The current work uses the Newton-Raphson (NR) incremental-iterative scheme for the implicit analysis of the nonlinear problem. In this technique, the applied external load (or prescribed displacement) is parametrised by a multiplicative factor λ, see Fig. 2.11(a), such that the following equilibrium holds

$$\mathbf{F}_{int}(\mathbf{u}) - \lambda_n \mathbf{F}_{ext} = \mathbf{0} \tag{2.28}$$

where λ_n is the load scaling factor at the pseudo-time instant t_n. The NR scheme involves an iterative process to find the converged solution $\mathbf{u}_{n+1}$, starting from the known solution $\mathbf{u}_n$. The

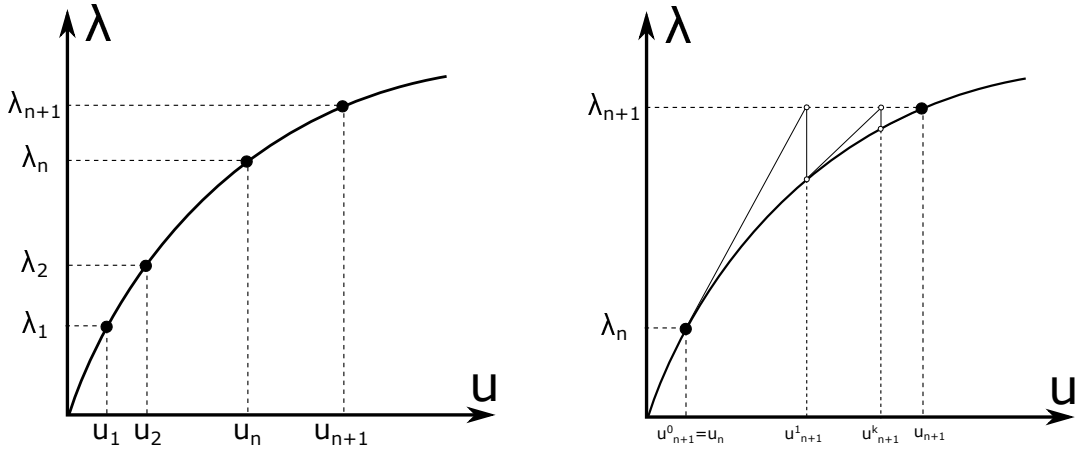

Fig. 2.11 The incremental-iterative Newton-Raphson method for implicit analysis. (a) Incrementation of external load with the λ parameter, and (b) Iterations within an increment to find the converged solution u_{n+1}.

Taylor series expansion of the internal force vector at the time t_{n+1}, $\mathbf{F}_{int}(\mathbf{u}_{n+1})$, is given as [5]

$$\mathbf{F}_{int}(\mathbf{u}_{n+1}^{k+1}) = \mathbf{F}_{int}(\mathbf{u}_{n+1}^{k}) + \frac{\partial \mathbf{F}_{int}(\mathbf{u}_{n+1}^{k})}{\partial \mathbf{u}_{n+1}^{k}}(\mathbf{u}_{n+1}^{k+1} - \mathbf{u}_{n+1}^{k}) + \frac{1}{2}\frac{\partial^2 \mathbf{F}_{int}(\mathbf{u}_{n+1}^{k})}{\partial \mathbf{u}_{n+1}^{k\,2}}(\mathbf{u}_{n+1}^{k+1} - \mathbf{u}_{n+1}^{k})^2 + \cdots \tag{2.29}$$

where k is the iteration index for the load increment $[n, n+1]$. Considering only the linear terms of the expansion in Eq. 2.29, the linearised equilibrium equation based on an incremental-iterative approach is obtained as

$$\mathbf{F}_{int}(\mathbf{u}_{n+1}^{k+1}) = \mathbf{F}_{int}(\mathbf{u}_{n+1}^{k}) + \frac{\partial \mathbf{F}_{int}(\mathbf{u}_{n+1}^{k})}{\partial \mathbf{u}_{n+1}^{k}}\Delta\mathbf{u}; \quad \Delta\mathbf{u} = (\mathbf{u}_{n+1}^{k+1} - \mathbf{u}_{n+1}^{k}) \tag{2.30}$$

where $\Delta\mathbf{u}$ is the incremental displacement, and the tangent stiffness matrix, $\mathbf{K}^T$, is defined as

$$\mathbf{K}^T = \frac{\partial \mathbf{F}_{int}(\mathbf{u}_{n+1}^{k})}{\partial \mathbf{u}_{n+1}^{k}} \tag{2.31}$$

which can be written in compact form, using CUF notation, as

$$\mathbf{k}_{ij\tau s}^T \Delta\mathbf{u}_{\tau i} = \phi_{js} \tag{2.32}$$

where $\mathbf{k}_{ij\tau s}^T$ is the FN of the tangent stiffness matrix, and ϕ_{js} is the residual force vector of unbalanced forces. The full NR approach is considered in the present work, where the tangent

stiffness matrix is computed for each iteration within the given load increment, see Fig. 2.11(b), but has the advantage of quadratic convergence rates. A flowchart showing the sequence of implicit nonlinear analysis in CUF, using the full Newton-Raphson approach, is shown in Fig. 2.12.

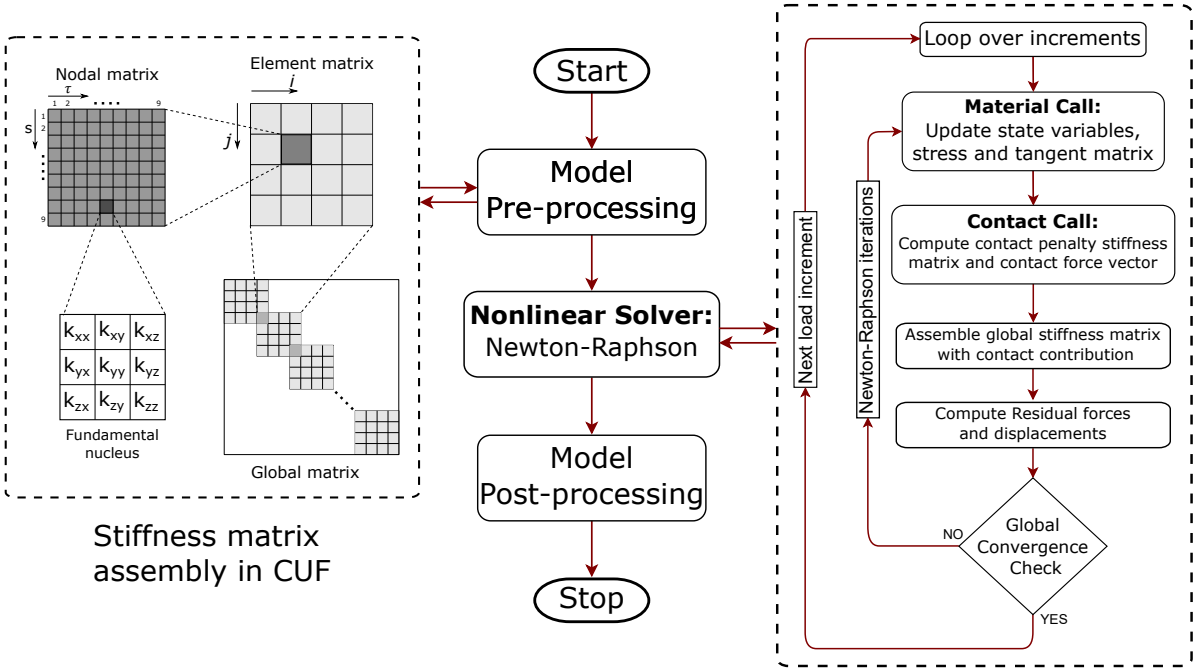

Fig. 2.12 Flowchart depicting the sequence of steps during an implicit analysis in CUF.

2.4.2 Explicit solution techniques

Explicit solution techniques are effective approaches to solving time-dependent problems, such as, for instance, impact problems. Such techniques involve the discretisation of the dynamic equation of motion. The use of explicit time integration schemes is particularly beneficial to solving highly nonlinear and dynamic problems, especially ones involving composite damage, in terms of convergence of the global solution. Implicit solution techniques to progressive damage analysis of fibre-reinforced composites often run into convergence issues, leading to a lack of a solution. Explicit time integration schemes typically do not suffer from these problems, due to the inherent framework of the technique. The semi-discrete balance of momentum is written as

$$\mathbf{M}\ddot{\mathbf{a}}^{t+\Delta t} = \mathbf{F}_{ext}^{t+\Delta t} - \mathbf{F}_{int}^{t+\Delta t} \tag{2.33}$$

where $\mathbf{M}$ is the mass matrix, $\mathbf{F}_{ext}$ is the external force vector, and $\mathbf{F}_{int}$ is the internal force vector. The solution of Eq. 2.33 is obtained via the central-difference time integration scheme

[34]. The velocity within a time step is approximated at its mid-interval as follows

$$\dot{\mathbf{u}}^{t+\frac{1}{2}\Delta t} = \frac{\mathbf{u}^{t+\Delta t} - \mathbf{u}^{t}}{\Delta t} \tag{2.34}$$

where $\mathbf{u}$ and $\dot{\mathbf{u}}$ are the displacement and velocity vectors, respectively. Δt represents the length of the time interval. Equation 2.34 can be reformulated to obtain the updated displacements

$$\mathbf{u}^{t+\Delta t} = \mathbf{u}^{t} + \Delta t\ \dot{\mathbf{u}}^{t+\frac{1}{2}\Delta t} \tag{2.35}$$

The new displacements are then used to update the strains, and consequently, the stress fields. From the updated stress tensor, the internal force vector $\mathbf{F}_{int}^{t+\Delta t}$ can be calculated as

$$\mathbf{F}_{int}^{t+\Delta t} = \int_{V} \mathbf{B}^{T} \boldsymbol{\sigma}^{t+\Delta t}\ dV \tag{2.36}$$

where $\mathbf{B}^{T}$ is the transpose of the $\mathbf{B}$ matrix, previously defined in Section 2.2. The updated acceleration can be determined from Eq. 2.33 as

$$\ddot{\mathbf{u}}^{t+\Delta t} = \mathbf{M}^{-1}\{\mathbf{F}_{ext}^{t+\Delta t} - \mathbf{F}_{int}^{t+\Delta t}\} \tag{2.37}$$

The mid-interval velocity at the next time interval, to be used in Eq. 2.35, can be obtained from the acceleration

$$\dot{\mathbf{u}}^{t+\frac{3}{2}\Delta t} = \dot{\mathbf{u}}^{t+\frac{1}{2}\Delta t} + \Delta t\ \ddot{\mathbf{u}}^{t+\Delta t} \tag{2.38}$$

The solution of the first time-step, at $t = 0$, requires the initial mid-interval velocity $\dot{\mathbf{u}}^{\frac{1}{2}\Delta t}$. This can be computed based on the following assumption

$$\dot{\mathbf{u}}^{\frac{1}{2}\Delta t} = \dot{\mathbf{u}}^{0} + \frac{1}{2}\Delta t\ \ddot{\mathbf{u}}^{0} \tag{2.39}$$

where $\dot{\mathbf{u}}^{0}$ and $\ddot{\mathbf{u}}^{0}$ are the initial velocity and accelerations of the system, respectively, and depend on the prescribed initial conditions.

Lumped mass matrix

The solution of Eq. 2.37 requires the inversion of the global mass matrix, which can quickly become a massive bottleneck for the analysis as the DOF of the system increases. This issue is eliminated by replacing the full (consistent) mass matrix with a lumped version, i.e. the lumped mass matrix, which is a diagonal matrix. The inversion of a diagonal matrix is trivial in terms of computational effort, and its use in Eq. 2.37 results in a simple vector multiplication.

The current work uses the row-summing method to obtain the lumped mass matrix, where the diagonal terms are computed according to

$$M_{ii}^{lumped} = \sum_{j} M_{ij} \tag{2.40}$$

The central difference explicit time integration, due to it inherent conditional stability, requires a time-step Δt, which is lower than a critical threshold $\Delta t_{critical}$. This value is determined using the highest frequency of the system ω_{max}, as shown below

$$\Delta t_{critical} = \frac{2}{\omega_{max}} \tag{2.41}$$

where ω_{max} is calculated using power iteration techniques, examples of which may be found in [103]. The explicit time integration scheme based on the central difference method is summarised in Table 2.3. A flowchart depicting the solution process using explicit time integration is presented in Fig. 2.13.

Table 2.3 The central-difference time integration scheme [34].

Initialise $\mathbf{u}^0$ and $\dot{\mathbf{u}}^0$
Evaluate lumped mass matrix $\mathbf{M}$
Compute initial mid-interval velocity: $\dot{\mathbf{u}}^{\frac{1}{2}\Delta t} = \dot{\mathbf{u}}^0 + \frac{1}{2}\Delta t\ \ddot{\mathbf{u}}^0$

For each time increment:
1. Evaluate new displacements: $\mathbf{u}^{t+\Delta t} = \mathbf{u}^t + \Delta t\ \dot{\mathbf{u}}^{t+\frac{1}{2}\Delta t}$
2. Compute displacement increment: $\Delta\mathbf{u} = \mathbf{u}^{t+\Delta t} - \mathbf{u}^t$
3. At each integration point:
$\rightarrow$ Compute updated strains: $\boldsymbol{\varepsilon}^{t+1} = \boldsymbol{\varepsilon}^t + \mathbf{B}\Delta\mathbf{u}$
$\rightarrow$ Compute updated stress: $\boldsymbol{\sigma}^{t+1} = \mathbf{C}^{sec}\boldsymbol{\varepsilon}^{t+1}$
4. Compute internal force vector: $\mathbf{F}_{int}^{t+\Delta t} = \int_V \mathbf{B}^T\boldsymbol{\sigma}^{t+\Delta t}\ dV$
5. Compute new accelerations: $\ddot{\mathbf{u}}^{t+\Delta t} = \mathbf{M}^{-1}\{\mathbf{F}_{ext}^{t+\Delta t} - \mathbf{F}_{int}^{t+\Delta t}\}$
6. Compute new mid-interval velocities: $\dot{\mathbf{u}}^{t+\frac{3}{2}\Delta t} = \dot{\mathbf{u}}^{t+\frac{1}{2}\Delta t} + \Delta t\ \ddot{\mathbf{u}}^{t+\Delta t}$

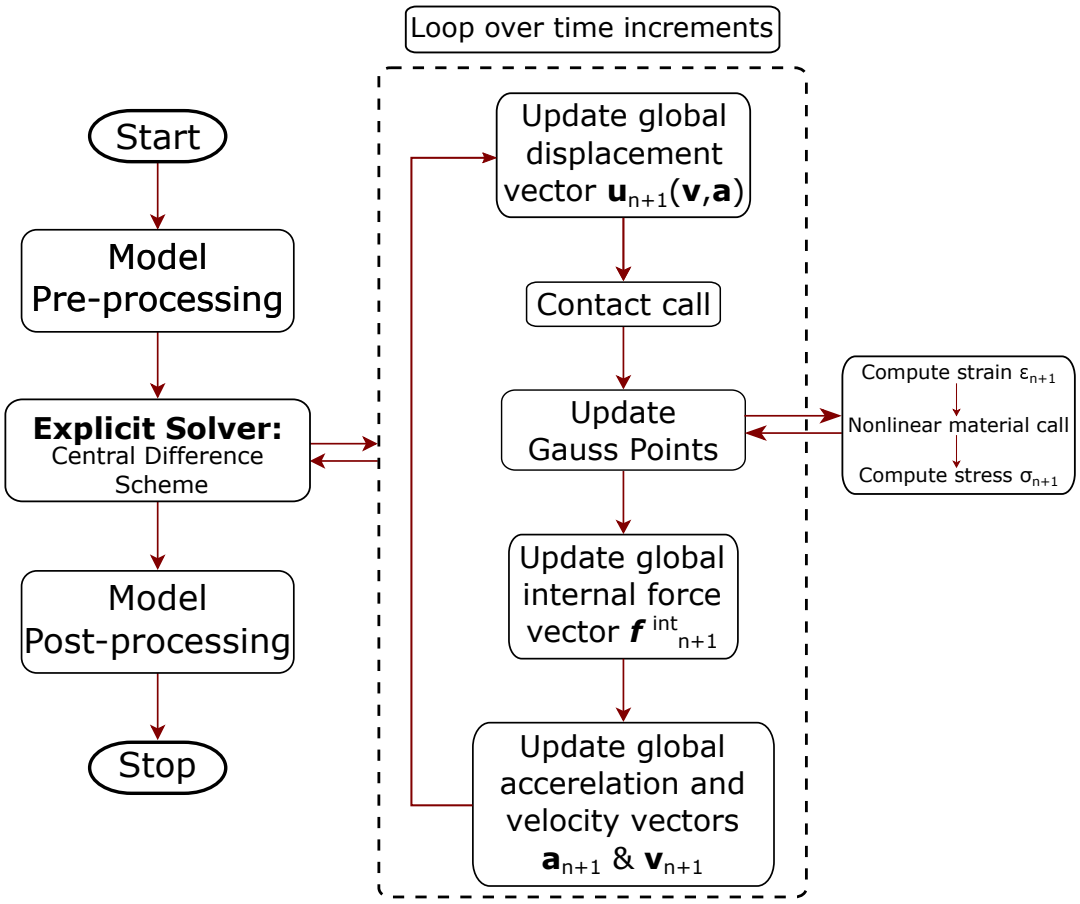

Fig. 2.13 Flowchart depicting the sequence of steps during an explicit analysis in CUF.

Chapter 3

Global-local Analysis

This chapter introduces the global-local approach to improve the computational efficiency of the numerical analysis, by developing a low-fidelity model of the global structure, and considering a high-fidelity model only for critical regions where accurate results are required. In particular, a two-step analysis procedure is described where the MUL^2 code based on CUF theories is interfaced with a commercial finite element code, ABAQUS. The former is used for the high-fidelity analysis of the critical region of interest, while the latter is used to generate a low-fidelity model of the global structure. A series of assessments, considering both linear and nonlinear material behaviour, is presented to demonstrate the global-local technique.[1]

3.1 Introduction

The high-fidelity analysis of composite structures invariably necessitates a highly refined finite element model, especially when interlaminar stress and strain fields are of interest, which leads to unfeasible computational overheads. Global-local analysis is a widely used approach to reduce computational costs without compromising on the numerical accuracy of the solution. Such techniques, in general, consist of using a relatively coarse finite element mesh to model the global structure, while a refined mesh is used in smaller regions of interest. These critical areas are usually points of stress concentration such as holes, cut-outs, free-edges in laminates,

[1] Parts of this chapter have been published in the following:

1. Petrolo, M., Nagaraj, M. H., Kaleel, I., & Carrera, E. (2018). A global-local approach for the elastoplastic analysis of compact and thin-walled structures via refined models. Computers & Structures, 206, 54-65.
2. Carrera, E., Fiordilino, G. A., Nagaraj, M., Pagani, A., & Montemurro, M. (2019). A global/local approach based on CUF for the accurate and efficient analysis of metallic and composite structures. Engineering Structures, 188, 188-201.

regions under concentrated loads etc. Such a process usually results in two boundary value problems, with various techniques used to interface them. One approach to interfacing the global and local problems is a two-step sequential analysis, where the global and local analyses are performed separately, with an intermediate processing step to transfer the global results as inputs to the local analysis. Another approach is concurrent in nature, where the global and local regions are meshed with different levels of refinement. This process leads to an incompatible mesh at the global-local interface, which requires the use of techniques such as mesh tie constraints. Other methods include the sub-modelling approach of ABAQUS, in addition to similar techniques available in commercial software. A schematic representation of the first type of the global-local technique, i.e. using a 2-step sequential approach, is shown in Fig. 3.1.

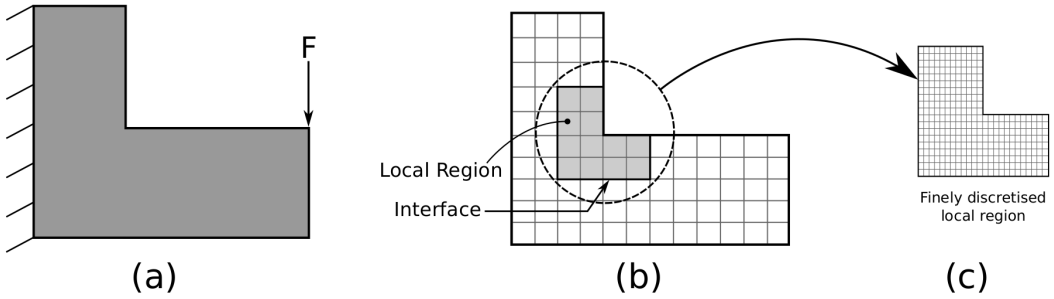

Fig. 3.1 The 2-step global-local technique. (a) The analysed structural problem, (b) low-fidelity global mesh with highlighted local region, and (c) high-fidelity local mesh.

3.2 The 2-step Global-local approach using CUF

The global-local technique developed in the current work is based on the 2-step approach, where a low-fidelity global model is developed in ABAQUS, a commercial FE code. The corresponding local analysis is performed using CUF models based on higher-order structural theories. The global displacements at the global-local interface, from the initial low-fidelity global analysis of the full structure, are extracted using python scripts and applied as displacement boundary conditions on the local CUF model. A high-fidelity analysis of the critical sub-regions of the structure is then carried out, without expending additional computational resources for the high-fidelity analysis of the remaining structure. Since 3D models are considered in the ABAQUS global analysis, and the CUF models for the local analysis exploit the Component-Wise approach based on Lagrange expansions, only translational degrees of freedom are involved throughout the entire process which makes the displacement transfer

straightforward. Furthermore, interpolation functions are used during the transfer of global displacements as local boundary conditions, so that incompatible global and local meshes can be used. The displacement transfer process between ABAQUS and CUF is schematically shown in Fig. 3.2. It is pointed out that unlike the standard two-step procedure shown in Fig. 3.1, where the local analysis is based on refining the mesh via the use of smaller elements (*h*-refinement), the current approach uses higher-order theories of structures generated using CUF to refine the local model (*p*-refinement). The following sections describe a series of numerical assessments on the application of the global-local approach towards the linear and physically nonlinear analysis of metallic and composite structures.

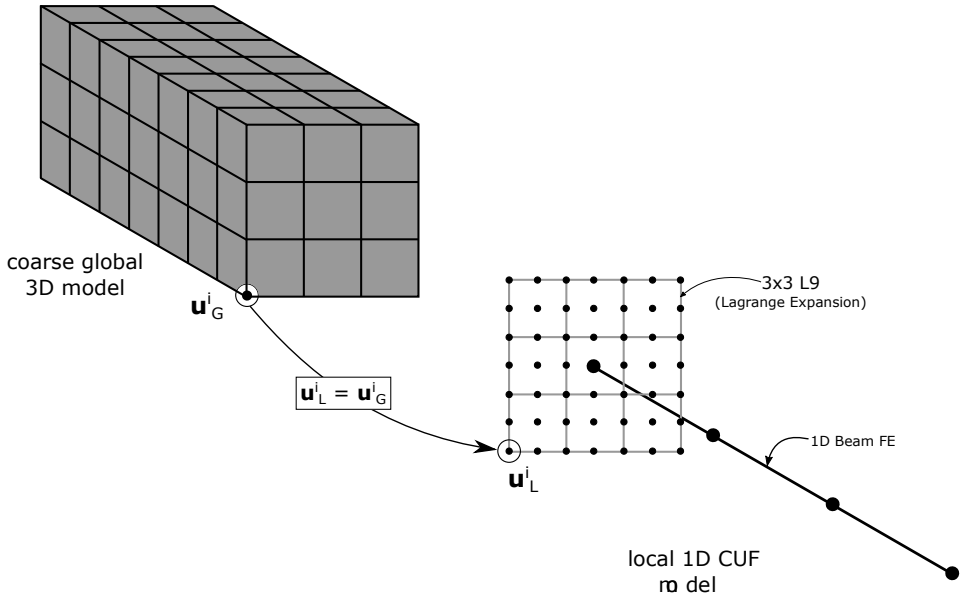

Fig. 3.2 The displacement transfer process between the global and local models.

3.3 Linear analysis with global-local techniques

3.3.1 Open-hole tension test

This numerical assessment considers an open-hole specimen subjected to a tensile load. The structure is shown in Fig. 3.3, where the critical region in the vicinity of the hole, highlighted in dark grey, is considered for the local analysis. The structure is composed of an isotropic material, with Young's modulus E = 200 GPa and Poisson's ratio $\nu = 0.30$. The global structure is clamped at one end, and a displacement $u_y = 0.025$ m is prescribed on the opposite edge. The structure is analysed using the global-local technique described in Section 3.2, where a low-fidelity 3D-FE model is first developed in ABAQUS, and the global displacements thus

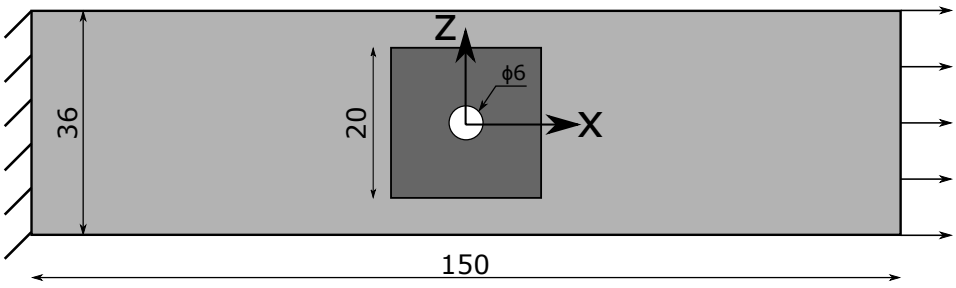

Fig. 3.3 The open-hole tensile specimen with the critical region for local analysis highlighted.

obtained are extracted from the global-local interface, to be applied as boundary conditions for the local CUF model. The global low-fidelity model is shown in Fig. 3.4, where the nodes at the interface are highlighted. The critical region near the hole is then analysed using a high-fidelity CUF model. The axial stress σ_{xx} along the z-axis is plotted in Fig. 3.5, along with the results obtained by a high-fidelity 3D-FE analysis for reference. The von Mises stress distribution, in the region of the hole, is shown in Fig. 3.6. Details of the various numerical models are provided in Table 3.1. The following comments are made:

1. The use of the global-local approach by interfacing ABAQUS and CUF models leads to accuracy of solutions comparable to that of 3D-FE, as seen in Fig. 3.5.

2. The global-local approach leads to a multi-fold reduction in both the size of the problem, in terms of degrees of freedom of the model, as well as computational cost in terms of the time required for the solution.

3. The local CUF analysis is able to accurately capture the stress distributions in the critical regions of the structure, as seen in Fig. 3.6, without expending computational effort towards the high-fidelity modelling of the global structure.

The above results verify the proposed global-local approach, and demonstrate its capability in the efficient and accurate analysis of structures.

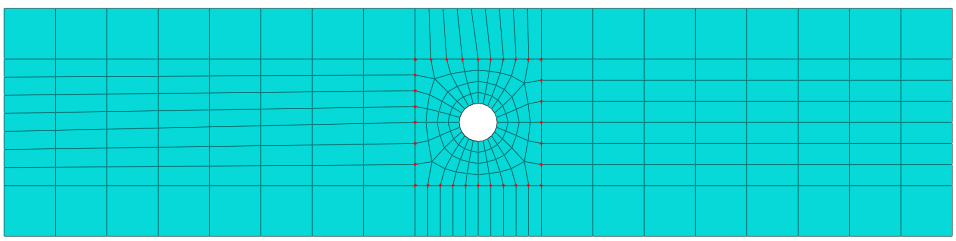

Fig. 3.4 Low-fidelity global 3D-FE model with the global-local interface highlighted.

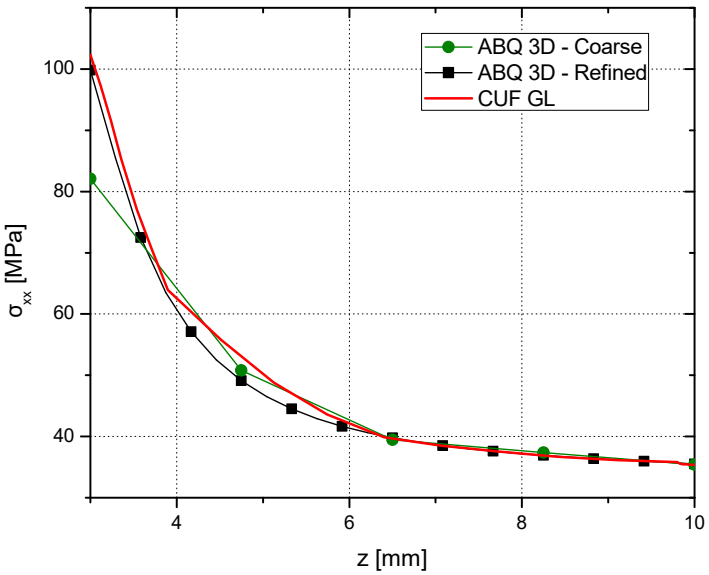

Fig. 3.5 Axial stress σ_{xx} along the z-axis of the open-hole tensile specimen.

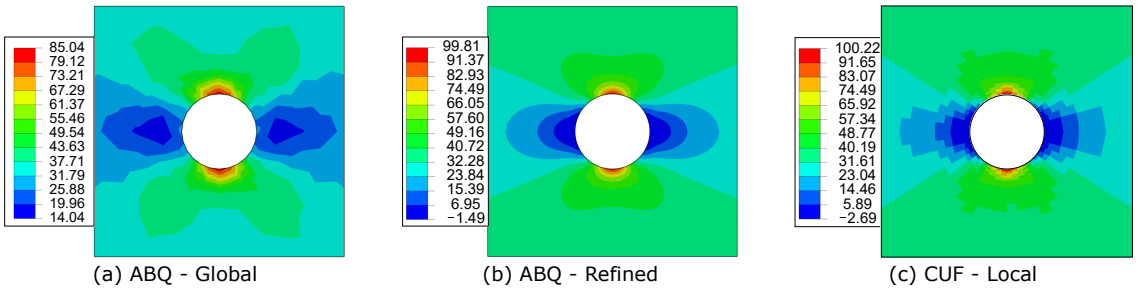

Fig. 3.6 von Mises stress distribution near the hole.

Table 3.1 Model details for the global-local analysis analysis of the open-hole tensile specimen.

Model	Discretisation	DOF	Time (s)
ABAQUS-Refined	31,416 C3D8	113,904	94
Global-Local Analysis			
ABAQUS-Global	510 C3D8	2,709	2
CUF-Local	1 B4-112 L9	5,760	1

3.3.2 Failure index evaluation of a stiffened composite panel

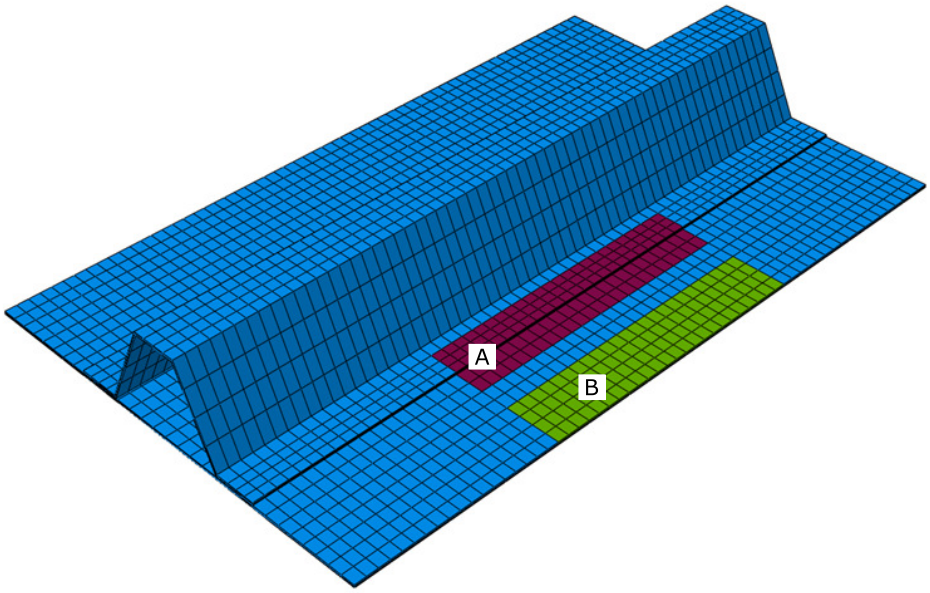

Fig. 3.7 Low-fidelity global mesh of the stiffened composite panel with highlighted regions for local analysis (a) Local region around the stiffener free-edge, and (b) local region around the panel free-edge.

The current example applies the global-local technique to the free-edge stress analysis of the stiffened composite structure previously described in Section 2.3. Two regions are considered for the local high-fidelity CUF analysis, encompassing the free-edge of the skin and the stringer. The low-fidelity global ABAQUS model, with the highlighted regions for local analysis, has been shown in Fig. 3.7. The structure is first modelled using a low-fidelity mesh in ABAQUS, and the displacements are used as input boundary conditions for the local high-fidelity analysis in CUF. The free-edge interlaminar stress fields σ_{yz} and σ_{zz}, for the stringer and the skin, have been plotted in Fig. 3.8 and Fig. 3.9, respectively. Failure indices based on Hashin's criteria for matrix failure and the the quadratic delamination criteria have also been calculated from the 3D stress results in a post-processing step. The failure indices at the free-edge of the stringer and the skin have been plotted in Fig. 3.10 and Fig. 3.11, respectively. Reference numerical results obtained using CUF and 3D-FEA, previously presented in Section 2.3, have also been included in the above plots for comparison. Details of the discretisation used and associated computational costs for the numerical analyses have been tabulated in Table 3.2. The following observations are made:

1. The local analysis performed using CUF models is able to evaluate stress fields, and consequently failure indices, with an accuracy equal to that of the reference global high-fidelity CUF models.

2. The global-local approach requires about 16x less computational time when compared to the global CUF model, demonstrating the computational savings that can be achieved by the proposed technique.

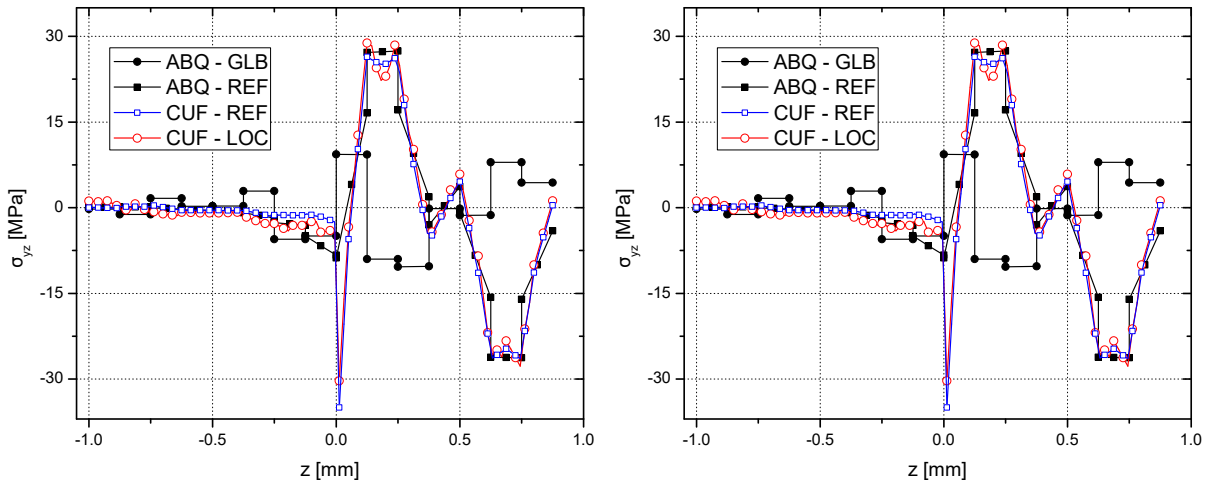

(a) σ_{yz} (b) σ_{zz}

Fig. 3.8 Free-edge interlaminar stresses through the thickness of the composite stiffener.

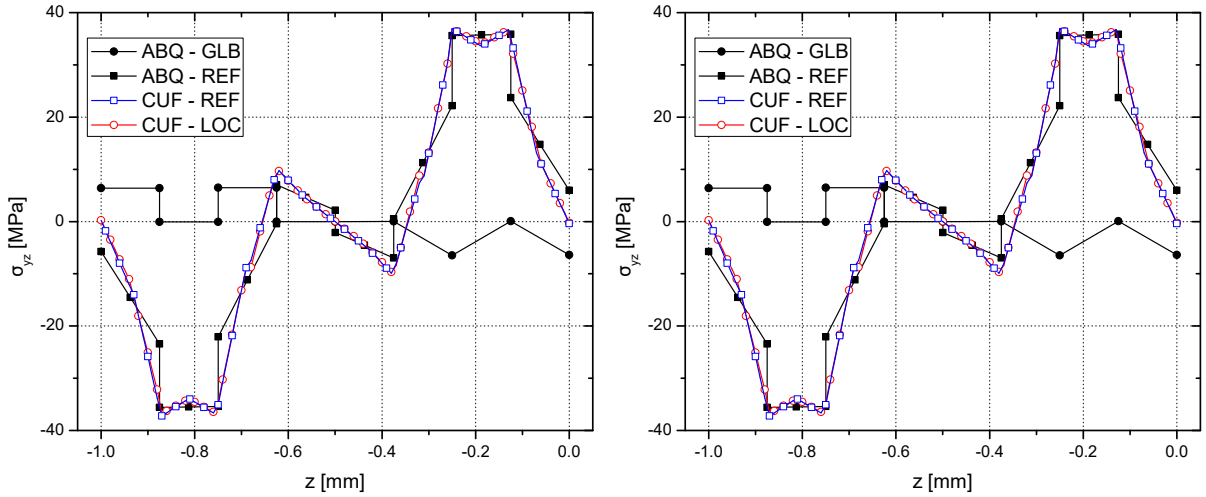

(a) σ_{yz} (b) σ_{zz}

Fig. 3.9 Free-edge interlaminar stresses through the thickness of the composite panel.

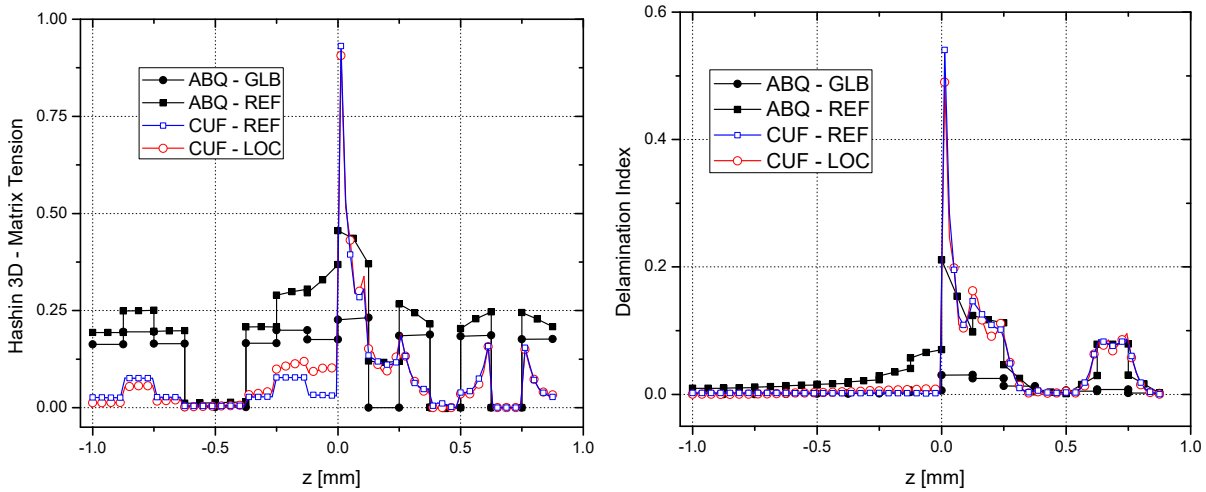

(a) Hashin 3D - Matrix tension (b) Delamination index

Fig. 3.10 Failure indices evaluated at the free-edge of the composite stiffener.

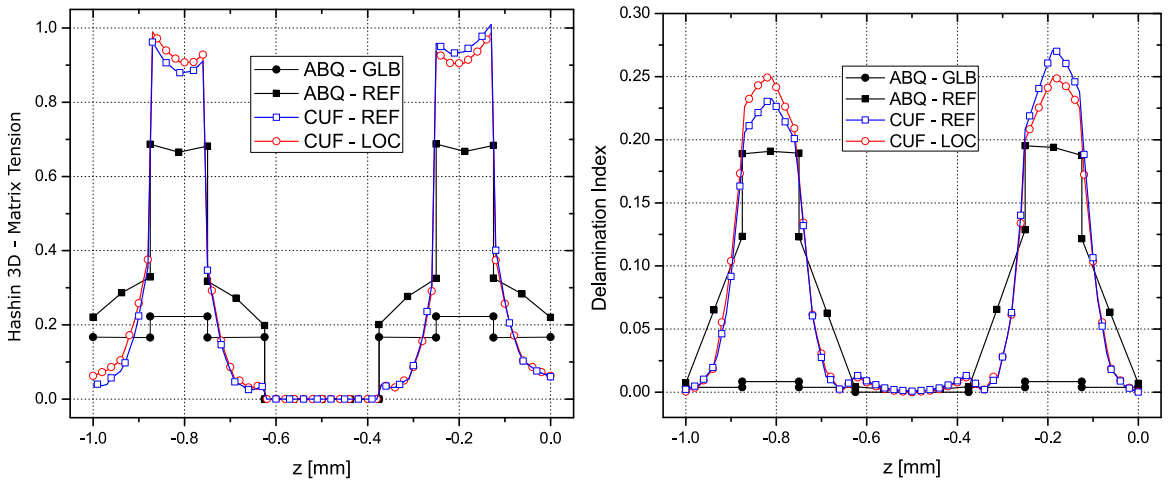

(a) Hashin 3D - Matrix tension (b) Delamination index

Fig. 3.11 Failure indices evaluated at the free-edge of the composite panel.

Table 3.2 Model details for the global-local analysis of the stiffened composite panel.

Model	Element Type	DOF	Time (s)
Reference			
ABAQUS-3D [35]	8-noded brick (C3D8)	4,560,150	3,764
CUF-LW [35]	710 L9-10 B4	277,326	478
Global-Local Analysis - Local Region A			
ABAQUS-3D	8-noded brick (C3D8)	81,801	8
CUF-LW	112L9-6 B4	28,215	25
Global-Local Analysis - Local Region B			
ABAQUS-3D	8-noded brick (C3D8)	81,801	8
CUF-LW	92L9-6 B4	24,909	22

3.4 Nonlinear analysis with global-local techniques

3.4.1 Elastoplastic analysis of cantilever beam under bending

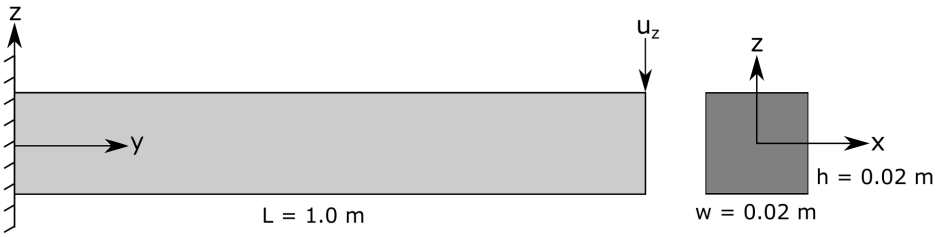

Fig. 3.12 Elastoplastic analysis of compact-section cantilever beam.

The present numerical example demonstrates the application of global-local analysis to nonlinear structural problems, where the nonlinearity stems from the elastoplastic behaviour of the material. A cantilever beam spanning 1 m in length is considered, with a compact square cross-section of edge length W = 0.02 m. One end is clamped, and a vertical displacement u_z = 0.1 m is applied at the tip, as seen in Fig. 3.12. The beam is composed of an isotropic elastoplastic material with Young's modulus E = 210 GPa, Poisson's ratio ν = 0.30, and initial yield stress σ_y = 210 MPa. Perfect plasticity has been assumed for the current assessment. Reference global solutions are obtained using a variety of structural theories available in CUF, as well as 3D-FE analysis in ABAQUS. The global-local approach is then used, in which a low-fidelity nonlinear analysis is first performed in ABAQUS, to estimate the extent of plastic growth. This is then used to determine the domain of the structure to be considered for the local

analysis. Based on the global analysis, the span y = [0, 0.25] of the beam has been modelled in CUF for the local high-fidelity analysis. The vertical deflection u_z along the y-axis is shown in Fig. 3.13, while the axial stress σ_{yy} along the z-axis of the beam at the point [y = 0.016] is shown in Fig. 3.14. The computational cost of each model, along with a summary of the results, is given in Table 3.3. The following comments are made

1. The results obtained by the global-local approach are in excellent agreement with reference 3D-FE and CUF results, thus verifying the capability of the approach towards nonlinear structural analysis.

2. The global-local approach allows for a high-fidelity nonlinear analysis of the plastic zone in a computationally efficient manner, requiring approximately 44x fewer degrees of freedom compared to a refined 3D-FE analysis of the entire structure.

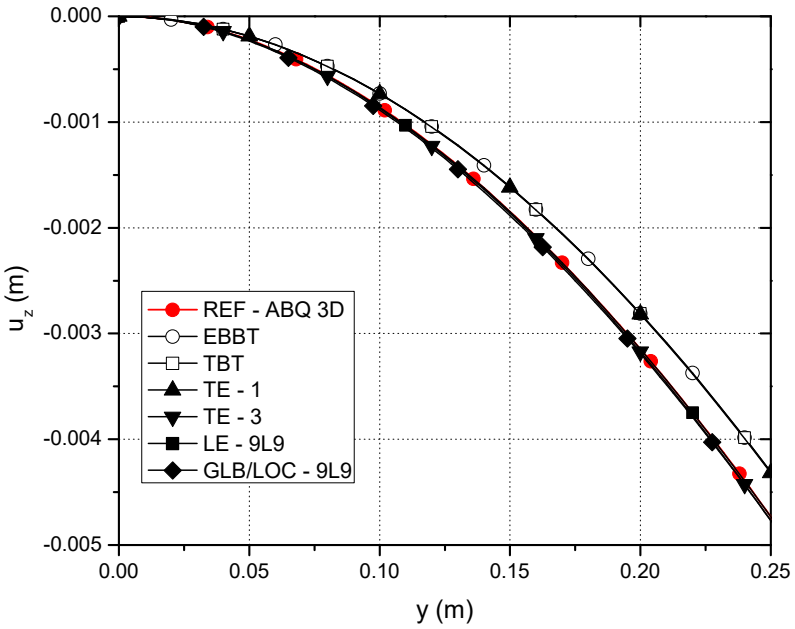

Fig. 3.13 Vertical deflection u_z of the cantilever beam (local region).

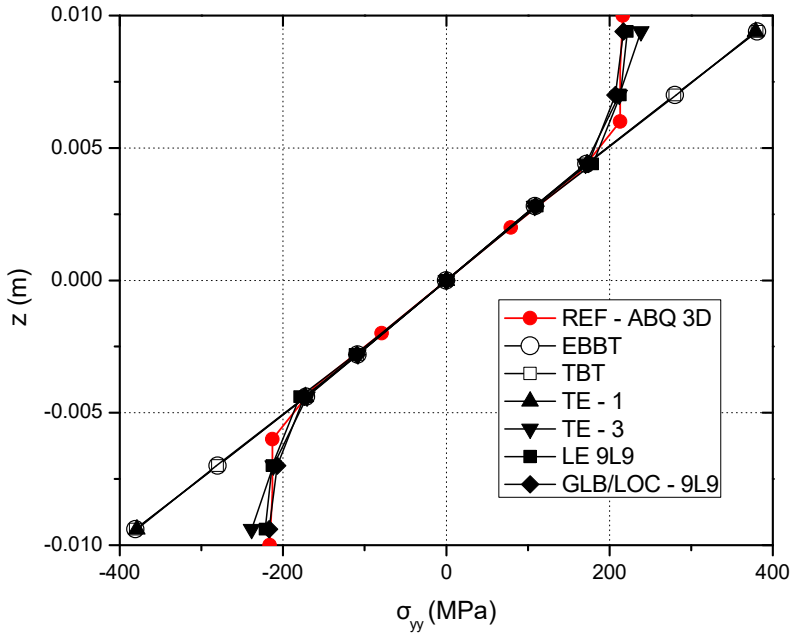

Fig. 3.14 Axial stress σ_{yy} through the thickness (y = 0.016 m) of the cantilever beam (local region).

Table 3.3 Computational costs and predicted results of the numerical approaches used in the analysis of the elastoplastic cantilever beam.

	DOF	u_z (mm)		σ_{yy} (MPa)
		y = 0.1	y = 0.5	x = 0.0, y = 0.1, z = 0.01
Reference				
ABAQUS-3D	694,023	-0.86	-16.21	214.4
CUF (40B4 along y-axis)				
EBBT	363	-0.73	-15.64	353.05
TBT	605	-0.73	-15.64	353.05
TE - 1	1089	-0.73	-15.65	352.68
TE - 3	3630	-0.87	-16.27	217.39
LE - 4L9	9075	-0.83	-16.21	215.59
LE - 9L9	17,787	-0.86	-16.21	216.3
Global-Local Analysis				
Global - ABQ-3D	6840	-0.86	-16.25	236.6
Local - 1D-CUF (20B4-9L9)	8967	-0.89	–	216.1

3.5 Discussion

A 2-step sequential global-local technique is presented where the academic MUL^2 code is interfaced with the commercial FE solver ABAQUS. An initial low-fidelity model of the global structure is developed and analysed in ABAQUS, and the obtained displacements are used as prescribed boundary conditions for the high-fidelity local CUF model of the required critical zones. The capabilities of the global-local technique is demonstrated using a series of numerical assessments. The first assessment is the tensile test of an open-hole isotropic plate. The global-local technique accurately captures the stress field at the region near the hole, and provides over a two order of magnitude reduction in the computational cost of the problem. The technique is then applied to the failure index evaluation of the stiffened composite panel, previously presented in Section 2.3. Two local CUF models are developed for the global-local analysis, considering the free-edge of the stringer and the panel, respectively. The free-edge stresses, and the subsequently calculated failure indices at the free-edge, are found to be in excellent agreement to single-step high-fidelity CUF analysis, whereas 3D-FE requires prohibitive levels of mesh refinement to approach the solutions predicted by the CUF models. The global-local approach provides an approximately $16x$ improvement in computational time when compared to global CUF models, and about $125x$ with respect to global 3D-FE models, demonstrating the potential of such techniques towards computationally efficient high-fidelity analysis. Finally, the global-local approach is applied to the elastoplastic analysis of a compact-section cantilever beam. The obtained results correlate very well with reference solutions based on global high-fidelity CUF and 3D-FE models, thus verifying the applicability of the proposed approach towards nonlinear problems. Furthermore, the global-local approach achieves a $44x$ reduction in the computational size of the problem, compared to full-scale 3D-FE approaches. The proposed global-local technique thus has potential as a powerful tool to obtain high-fidelity solutions in a computationally efficient manner.

Chapter 4

Contact modelling in the CUF framework

This chapter introduces the concept of computational contact mechanics, and the implementation of contact algorithms in the CUF framework. The formulation and implementation of the node-to-node and node-to-surface contact discretisation schemes are described, along with the penalty and the Lagrange multiplier approach to contact enforcement. A series of numerical assessments is presented to demonstrate the capability of the CUF framework in handling quasi-static contact problems, using implicit solution techniques, as well as dynamic contact/impact problems, analysed using explicit solution techniques.[1]

4.1 Node-to-node contact

Consider two distinct structures Ω_i, i = 1,2, as shown schematically in Fig. 4.1. Two distinct points $\mathbf{X}_1$ and $\mathbf{X}_2$ which are initially on the boundary of the respective bodies, enter into a state of contact under the deformation φ. The position of the points $\mathbf{X}_i$ in the current configuration is

$$\mathbf{x}_i = \mathbf{X}_i + \mathbf{u}_i;\ i = 1,2 \tag{4.1}$$

where $\mathbf{u}_i$ is the displacement of the reference point $\mathbf{X}_i$. When the two bodies are in contact, the two points become coincident, i.e. $\mathbf{x}_1 = \mathbf{x}_2$. Contact between two surfaces can be taken into consideration either through the application of geometric constraints, or via the use of

[1] Parts of this chapter have been published in the following:

1. Nagaraj, M. H., Kaleel, I., Carrera, E. & Petrolo, M. (2020). Contact analysis of laminated structures including transverse shear and stretching. European Journal of Mechanics-A/Solids, 80, 103899.

2. Nagaraj, M. H., Kaleel, I., Carrera, E. & Petrolo, M. (2020). Nonlinear analysis of compact and thin-walled metallic structures including localized plasticity under contact conditions. Engineering Structures, 203, 109819.

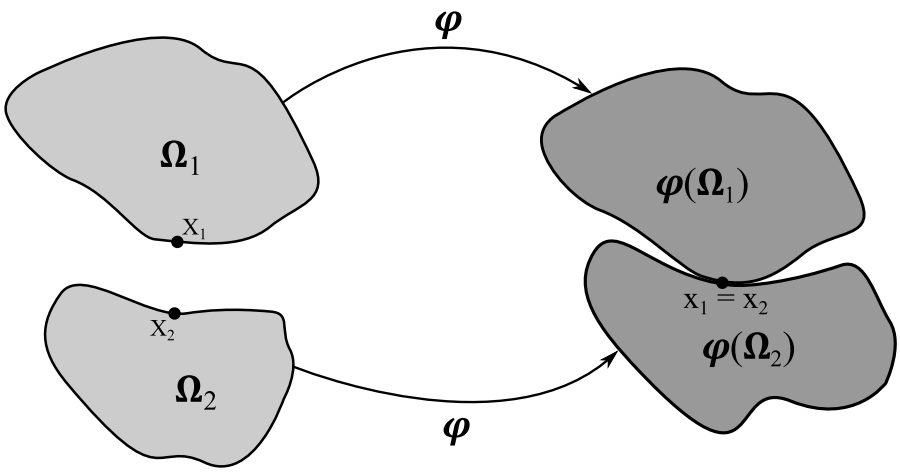

Fig. 4.1 Schematic representation of node-to-node contact.

constitutive laws at the contact interface [149]. In the current work, geometrical constraints have been considered, where a non-penetration condition is used to prevent the penetration of one body into the other. Such a condition is given in the form of a gap function g_N which is defined as

$$g_N = (\mathbf{x}_2 - \mathbf{x}_1) \cdot \mathbf{n}_1 \geq 0 \tag{4.2}$$

where $\mathbf{n}_1$ is the normal vector with respect to Ω_1. Assuming geometrically linear kinematics, the gap function given in Eq. 4.2 can be reformulated as

$$g_N = [(\mathbf{X}_2 + \mathbf{u}_2) - (\mathbf{X}_1 + \mathbf{u}_1)] \cdot \mathbf{n}_1 \geq 0 \tag{4.3}$$

$$= [(\mathbf{X}_2 - \mathbf{X}_1) + (\mathbf{u}_2 - \mathbf{u}_1)] \cdot \mathbf{n}_1 \geq 0 \tag{4.4}$$

which results in the following form of the gap function

$$g_N = (\mathbf{u}_2 - \mathbf{u}_1) \cdot \mathbf{n}_1 + g_{init} \geq 0 \tag{4.5}$$

where the initial gap between the two points in the reference configuration, g_{init}, is given by

$$g_{init} = (\mathbf{X}_2 - \mathbf{X}_1) \cdot \mathbf{n}_1 \tag{4.6}$$

In such an approach, the system enters into a state of contact when the gap function $g_N = 0$. The normal component of the stress field relates to the contact pressure p_N, and is obtained as a consequence of the contact constraint, i.e., it is not computed directly via constitutive equations. The contact pressure is equal and opposite for the two bodies at the point of contact. This leads

to a set of Kuhn-Tucker type equations in the following form

$$g_N \geq 0,\ p_N \leq 0,\ g_N p_N = 0 \tag{4.7}$$

which in the context of constraint-based frictionless contact are termed as Hertz-Signorini-Moreau conditions [149].

Weak form of the node-to-node contact BVP

According to the principle of virtual work, the equilibrium equation for a static structural problem is given by

$$\delta L_{int} = \delta L_{ext} \tag{4.8}$$

This remains the same even for the case of static contact problems, except for the addition of a contact term δL_c, which signifies the variation of the work done due to contact. However, since the contact term arises due to the non-penetration condition (see Eq. 4.5), which is an inequality, the resulting variational form is also an inequality and is given by

$$\delta L_{int} \geq \delta L_{ext} + \delta L_c \tag{4.9}$$

This inequality introduces a nonlinearity to the problem, even when both material and geometrical linearity are considered. Therefore cases involving contact constitute a class of nonlinear problems based on nonlinear boundary conditions. In the current work, the nonlinear problem arising from contact constraints is implicitly solved using the Newton-Raphson method, described previously in Section 2.4.1. Furthermore, the penalty method is considered for the enforcement of the contact constraint using a variational approach. Based on the penalty approach, the work due to contact is defined as

$$L_c = \frac{1}{2}\int_{\partial\Omega_c} \varepsilon_N g_N^2 dA \tag{4.10}$$

where ε_N is the penalty parameter for normal contact, and $\partial\Omega_c$ is the contact surface. The virtual variation is then given by

$$\delta L_c = \int_{\partial\Omega_c} \varepsilon_N g_N \delta g_N dA \tag{4.11}$$

Finite element formulation of node-to-node contact

In the node-to-node formulation, the contact constraints are enforced at the nodal level, for a given node pair. This approach to contact discretisation requires nodal compatibility at the contact interface i.e. matching meshes for the two bodies in contact, and is valid for the case of geometrical linear theory, where infinitesimal deformations ensure that the nodes remain aligned in the deformed configuration. Considering the penalty approach to contact enforcement, the global equilibrium is defined by

$$[\mathbf{K}+\mathbf{K}^p]\mathbf{u} = \bar{\mathbf{F}} \tag{4.12}$$

where $\mathbf{K}^p$ is the contact penalty stiffness matrix, and is an addition to the structural stiffness matrix $\mathbf{K}$. The global contact penalty stiffness matrix is formed by the assembly of the penalty stiffness terms for a given node pair i, which is given by

$$\mathbf{k}_i^p = \varepsilon_N \mathbf{n}_i^T \mathbf{n}_i \tag{4.13}$$

where $\mathbf{n}_i = \{n_x, n_y, n_z\}$ is the unit normal vector for the node pair i. The correct estimation of ε_N is critical since it should be large enough to enforce the contact constraint to an acceptable level of accuracy, while at the same time not so large as to cause ill-conditioning of the stiffness matrix. In the current work, the following estimation of the penalty parameter has been used [96]

$$\varepsilon_N \leq \frac{min(\mathbf{K})}{\sqrt{N \cdot t}} \tag{4.14}$$

where $min(\mathbf{K})$ represents the smallest coefficient of the global stiffness matrix, N is the degrees of freedom of the global system, and t is the round-off error, which is in the order of 10^{-17} for the current work where double precision has been used. Equation 4.14 is used to update the value of ε_N at the start of every increment of the nonlinear solution. The contact pressure at the contact region takes the form of a nodal force for the case of node-to-node contact. Such a nodal contact force $\mathbf{F}_i^c$ for the node pair i is a consequence of enforcing the contact constraint g_N between the nodes, and can be written from Eq. 4.11 as

$$\mathbf{F_i^c} = \varepsilon_N g_N \mathbf{n} \tag{4.15}$$

The contact force term is added to the external force vector $\mathbf{F}_{ext}$, and the resulting vector represents the right hand side of Eq. 4.12

$$\bar{\mathbf{F}} = \mathbf{F}^c + \mathbf{F}_{ext} \tag{4.16}$$

4.2 Node-to-surface contact

Node-to-node contact algorithms, as the simplest contact discretisation schemes, are easy to implement within finite element codes. However, they have several restrictions such as the requirement for nodal compatibility of the contacting surfaces as well as being unsuitable for large deformation contact. These points highlight the need for more sophisticated types of contact discretisation. One such type of intermediate complexity is the node-to-surface algorithm where contact at one surface is enforced at a nodal level, while contact on the other surface is enforced at a surface level i.e. the enforcement is carried out in an integral sense over the entire surface of the contact element. The node-to-surface scheme considered in the current work is used to model contact within the context of impact analysis, and is thus implemented for use within explicit time integration schemes. Furthermore, the Lagrange multiplier approach is used to enforce contact at the node-surface pair, and the use of such a contact model within explicit time integrations schemes necessitates a modification to the Lagrange multiplier algorithm to ensure non-singularity of the system. This approach was first developed by Carpenter et al. [18], and is termed the Forward Increment Lagrange Multiplier technique. This method is described in detail in the following sections.

Forward increment Lagrange multiplier

The dynamic contact/impact analyses presented in this thesis make use of the node-surface contact discretisation scheme, where the contact constraints are enforced using the forward increment Lagrange multiplier algorithm, following the works of Carpenter et al. [18]. It can be shown that the system of equilibrium equations with Lagrange multipliers becomes singular for a fully explicit analysis. A modification is thus necessary to use this approach in combination with central-difference schemes, whereby the constrained displacements at time t_{n+1} are coupled with the Lagrange multiplier values at time t_n. The term *forward increment* stems from this modification, and ensures that the system remains non-singular. According to this approach, the incremental equation of motion is written as

$$\mathbf{M}\ddot{\mathbf{u}}_n + \mathbf{F}_{int}(\mathbf{u}_n, \dot{\mathbf{u}}_n) + \mathbf{G}_{n+1}^T \boldsymbol{\lambda}_n = \mathbf{F}_{ext} \tag{4.17}$$

subject to

$$\mathbf{G}_{n+1}[\mathbf{u}_{n+1} + \mathbf{X}] = \mathbf{0} \tag{4.18}$$

where $\mathbf{M}$ is the lumped mass matrix, and the contact constraint matrix is denoted by $\mathbf{G}$. The vector of Lagrange multipliers is given by $\boldsymbol{\lambda}$, and represent contact force terms. Equations 4.17

and 4.18 are explicitly integrated, leading to

$$\mathbf{u}_{n+1} = \mathbf{u}^*_{n+1} + \mathbf{u}^c_{n+1} \tag{4.19}$$

where

$$\dot{\mathbf{u}}_n = \frac{1}{\Delta t}[\mathbf{u}_n - \mathbf{u}_{n-1}] \tag{4.20}$$

$$\mathbf{u}^*_{n+1} = \Delta t^2 \mathbf{M}^{-1}[\mathbf{F}_{ext} - \mathbf{F}_{int}] + 2\mathbf{u}_n - \mathbf{u}_{n-1} \tag{4.21}$$

$$\boldsymbol{\lambda}_n = [\Delta t^2 \mathbf{G}_{n+1}\mathbf{M}^{-1}\mathbf{G}^T_{n+1}]^{-1}\mathbf{G}_{n+1}\{\mathbf{u}^*_{n+1} + \mathbf{X}\} \tag{4.22}$$

$$\mathbf{u}^c_{n+1} = -\Delta t^2 \mathbf{G}^T_{n+1}\boldsymbol{\lambda}_n \tag{4.23}$$

To obtain the incremental solution of Eqs. 4.19-4.23, a trial displacement increment ($\mathbf{u}^*_{n+1}$) is first used, where the influence of the contact forces ($\boldsymbol{\lambda}$) are ignored. The position vector ($\mathbf{x}^*_{n+1} = \mathbf{u}^*_{n+1} + \mathbf{X}$) of the contact nodes is then evaluated, which is used to check for penetration. The constraint matrix (see Eq. 4.24) is then computed, and used in Eq. 4.22 to determine the Lagrange multipliers. Equation 4.23 is then used to compute $\mathbf{u}^c_{n+1}$, the displacement increment due to contact forces, and subsequently to update the displacement vector (Eq. 4.19). A detailed derivation of the forward increment Lagrange multiplier technique is available in [18].

Finite element formulation of node-to-surface contact

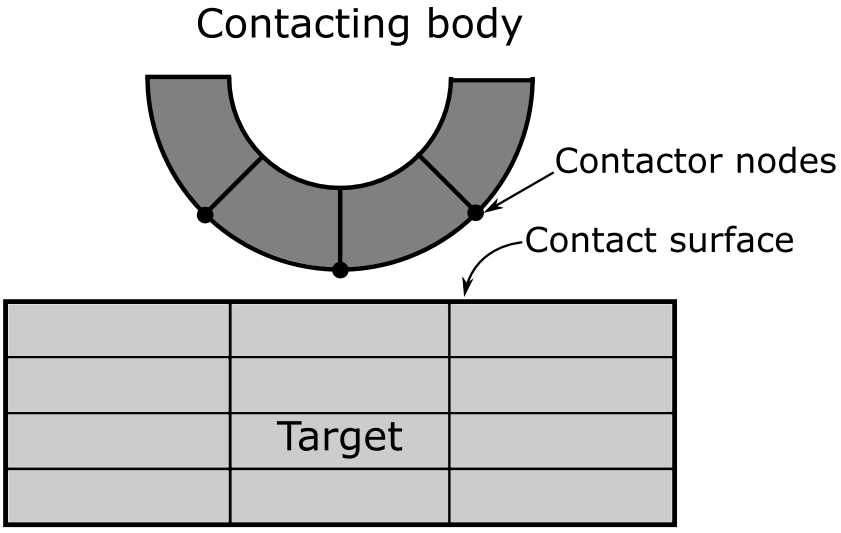

Fig. 4.2 Node-surface contact discretisation.

In node-to-surface contact discretisation schemes, the contact surface of the target body is discretised using 2D elements, whereas the contactor surface makes use of contact nodes,

as seen in Fig. 4.2. In other words, the target body enforces contact in an integral sense over the 2D contact surface domain, while the contactor body enforces contact in a discrete manner at the contact nodal points. For the current node-to-surface contact approach, the constraint matrix **G** is defined as

$$\mathbf{G} = \begin{bmatrix} N_1 & 0 & 0 & \dots & N_m & 0 & 0 & -1 & 0 & 0 \\ 0 & N_1 & 0 & \dots & 0 & N_m & 0 & 0 & -1 & 0 \\ 0 & 0 & N_1 & \dots & 0 & 0 & N_m & 0 & 0 & -1 \end{bmatrix} \tag{4.24}$$

where N refers to the nodal shape functions of the finite element at the contact surface, and m is the number of nodes in the element. The discrete contact constraints at the contactor surface nodes are represented by [[-1]], and are inserted at the right end of the **G** matrix, as seen in Eq. 4.24. A local contact search is performed to associate a given contactor node with the required target contact surface element, and the corresponding contact point on the surface element is determined by the closest point projection technique [62, 8].

4.3 Numerical assessments of static contact problems

4.3.1 Indentation of a doubly-clamped sandwich beam

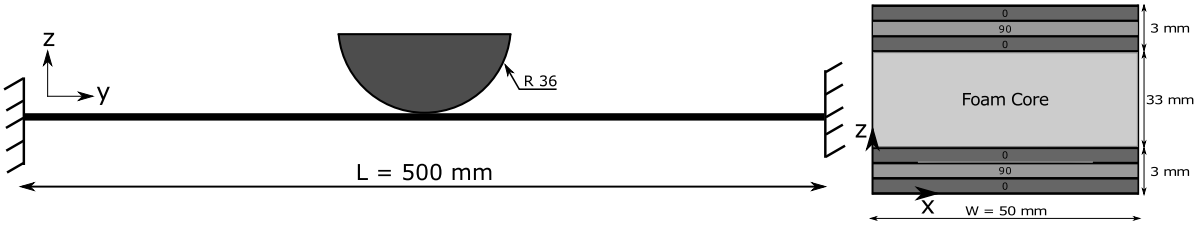

Fig. 4.3 Indentation of a doubly-clamped sandwich beam.

The numerical assessment considers a sandwich beam clamped at both ends, and indented by a hemispherical indenter at its midspan. The sandwich beam consists of a foam core and [0/90/0] composite face-sheets. A schematic view of the structure, along with the geometrical dimensions, is shown in Fig. 4.3. The foam core is composed of an isotropic elastic material with Young's modulus E = 35 MPa, and Poisson's ratio $\nu = 0.33$. The face-sheet is made of Glass-fibre/Polyester, and its elastic properties are listed in Table 4.1. The indenter is considered to be a rigid body. 1D-CUF models are developed using the layer-wise approach (LW), while reference 3D-FEA solutions are obtained from ABAQUS. Details of the various numerical models are summarised in Table 4.2. The axial deformation and the axial stress σ_{yy} are plotted in Fig. 4.4 and Fig. 4.5, respectively. The axial displacement and stress plots also include

solutions obtained using classical beam theories such as EBBT and TBT. The through-thickness interlaminar shear stress σ_{yz} at y = 150 mm is shown in Fig. 4.6. 2D maps of the normal strain component ε_{zz}, on the sandwich cross-section at the beam midspan (y = 250 mm), is shown in Fig. 4.7, while that of the axial stress σ_{yy} is shown in Fig. 4.8. Some important observations are enumerated in the following:

1. The current example demonstrates the capability of 1D-CUF models in handling contact problems. The use of refined beam theories lead to accurate displacement (Fig. 4.4) and stress (Fig. 4.5) solutions, comparable to 3D-FE. Conversely, classical beam theories are unable to accurately solve contact problems due to their kinematic limitations.

2. 1D-CUF models, using Lagrange expansion functions, are able to account for through-thickness deformations and transverse stretching, as seen in Fig. 4.7. They are also able to accurately compute interlaminar stress components, which requires 3D-FEA considering standard modelling approaches.

3. The use of 1D models leads to a 17x reduction in the DOF and 3x speed-up in the analysis time, when compared to refined 3D-FEA, demonstrating the computational efficiency of the CUF framework.

Table 4.1 Material properties of the glass-fibre/polyester laminated composite material.

Material	E_1 [GPa]	E_2 [GPa]	E_3 [GPa]	G_{12} [GPa]	G_{13} [GPa]	G_{23} [GPa]	ν_{12}	ν_{13}	ν_{23}
Glass fibre-Polyester	25.8	8.7	8.7	3.5	3.5	2.4	0.34	0.34	0.47

Table 4.2 Model details for the contact analysis of the sandwich beam under indentation.

Model	Sandwich beam discretisation	DOF	CPU Time (s)
Reference 3D-FEA			
ABQ3D - Coarse	11,200 C3D8R, 1 element per ply	45,408	40
ABQ3D - Medium	44,800 C3D8R, 2 elements per ply	153,300	320
ABQ3D - Refined	80,000 C3D8R, 4 elements per ply	261,675	832
ABQ3D - Quadratic	14,000 C3D20R, 1 element per ply	201,504	396
CUF Layer-Wise Theory			
CUF - LW	10 B4 - 32 L9, 1 element per ply	14,229	279

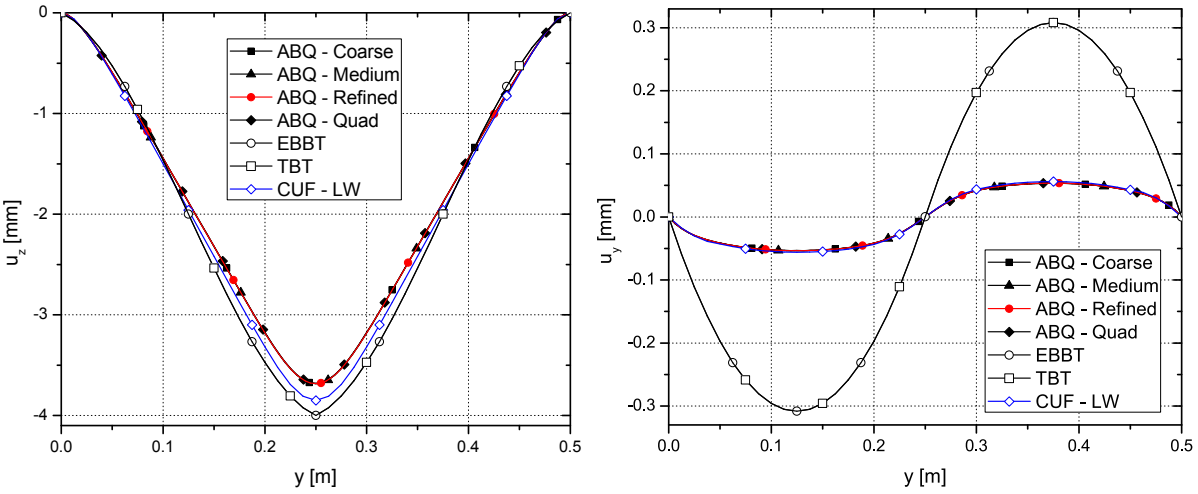

(a) Vertical deflection u_z (b) Axial displacement u_y

Fig. 4.4 Axial deformation of the doubly-clamped sandwich beam under indentation.

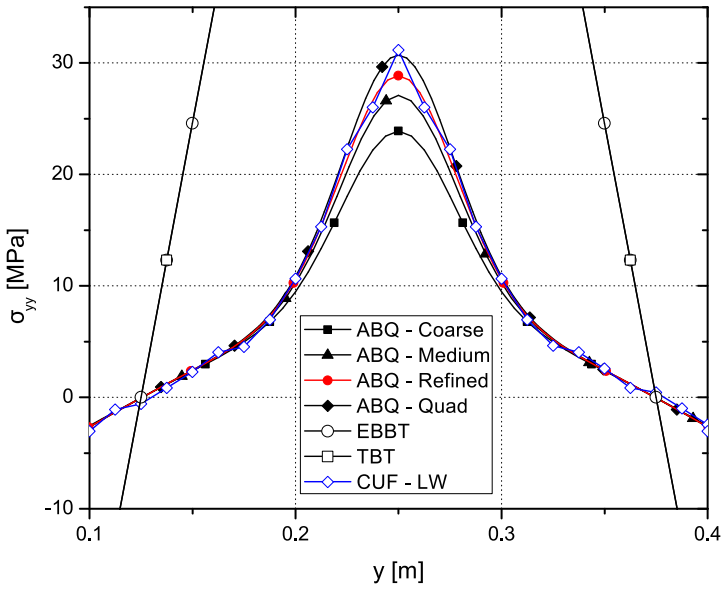

Fig. 4.5 Axial stress σ_{yy} along the axis of the doubly-clamped sandwich beam under indentation.

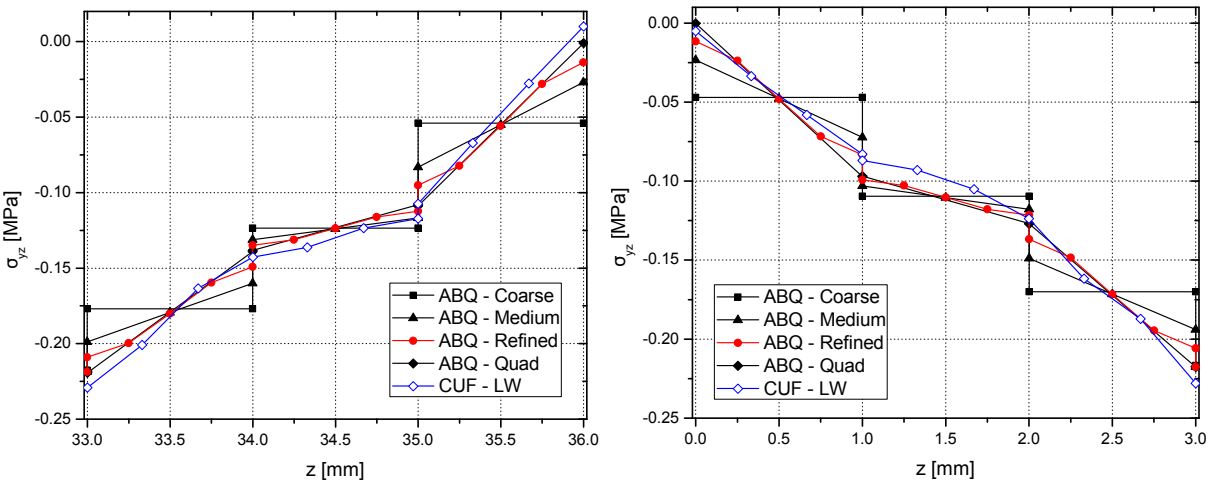

(a) top face-sheet (b) bottom face-sheet

Fig. 4.6 Interlaminar shear stress σ_{yz} though the thickness at the top and bottom face-sheets of the doubly-clamped sandwich beam (y = 150 mm).

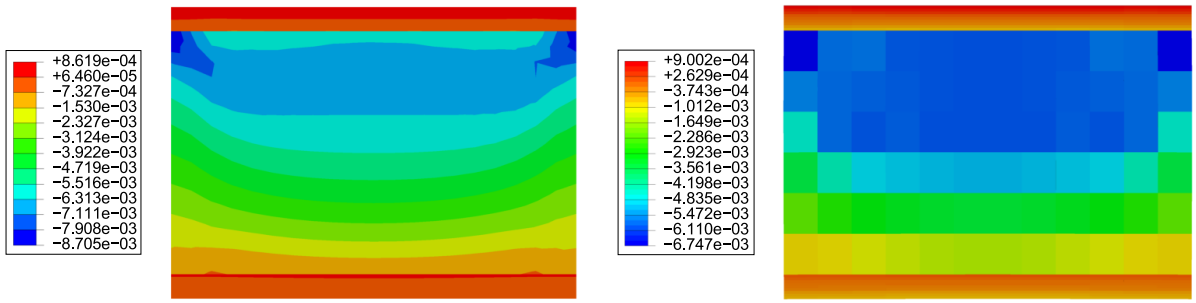

(a) ABQ - Refined (b) CUF - LW

Fig. 4.7 Distribution of strain component ε_{zz} of the sandwich cross-section at the beam midspan (y = 250 mm).

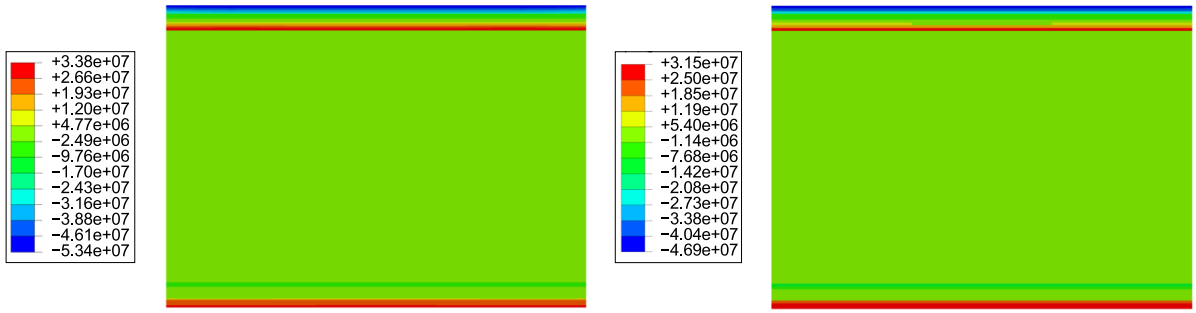

(a) ABQ - Refined (b) CUF - LW

Fig. 4.8 Distribution of stress component σ_{yy} of the sandwich cross-section at the beam midspan (y = 250 mm).

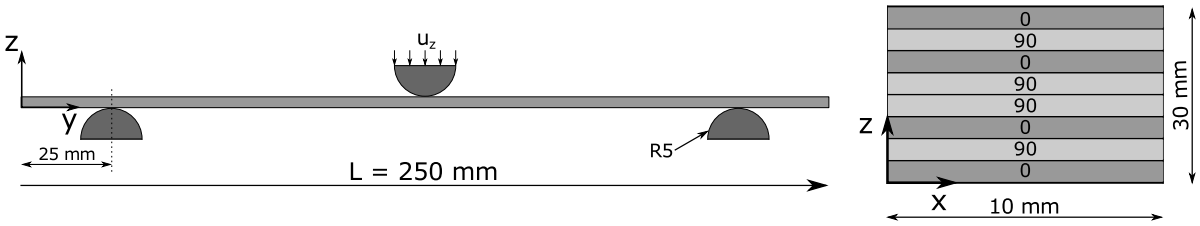

Fig. 4.9 Geometry and boundary conditions for the 3-point bending analysis of a composite laminated beam.

4.3.2 3-point bending of composite laminated beam

The current example considers the 3-point bending analysis of a composite laminated beam. The beam is supported by two rollers, and the load is applied via a central roller placed on top of the beam, at its midspan, as shown in Fig. 4.9. Contact between the components is taken into account using a combination of node-to-node discretisation and the penalty approach to contact enforcement. The laminate stacking sequence is $[0/90]_{2s}$ and the total thickness is 30 mm, while the span of the beam is 250 mm. The radius of each roller is 5 mm, and the support rollers are placed 25 mm from each end of the beam. The composite beam is constructed of IM7/8552 CFRP, whose elastic properties are given in Table 4.3. The structure is modelled using layer-wise beam theories based on CUF (CUF-LW) as well as 3D-FEA (ABQ-3D). Model information such as the discretisation, DOF used and analysis time for the two models are listed in Table 4.4. The vertical deflection u_z and axial stress σ_{yy} of the beam along its axis has been plotted in Fig. 4.10, while the axial strain ε_{yy} and stress σ_{yy} components, at the beam midspan (y = 125 mm) and through its thickness, have been plotted in Fig. 4.11. The distribution of the transverse strain ε_{zz} across the beam cross-section at the point y = 150 mm has been shown in Fig. 4.12, while that of the transverse shear stress σ_{yz} has been given in Fig. 4.13. Based on the obtained results, the following comments are made:

1. The example demonstrates the capability of the framework in modelling an arbitrary number of bodies simultaneously in contact.

2. The assessment confirms the capabilities of CUF-LW approaches in the accurate evaluation of stress and strain fields along the laminate thickness.

3. The layer-wise modelling approach results in an accurate evaluation of strain and stress fields, comparable in quality to 3D-FEA, and can account for deformations through the thickness of the laminate.

4. The CUF analysis requires about 11x fewer DOF and is about 4x times faster compared to 3D-FEA.

Table 4.3 Material properties of the IM7/8552 laminated composite material.

Material	E_1 [GPa]	E_2 [GPa]	E_3 [GPa]	G_{12} [GPa]	G_{13} [GPa]	G_{23} [GPa]	ν_{12}	ν_{13}	ν_{23}
IM7/8552	165.00	9.00	9.00	5.60	5.60	2.80	0.34	0.34	0.50

Table 4.4 Model details for the 3-point bending analysis of the composite beam.

Model	Discretisation of laminated beam	DOF	CPU Time (s)
ABQ - 3D	27,200 C3D8R, 3 elements per ply	399,366	1313
CUF - LW	20 B4 - 32 L9, 1 element per ply	34,236	326

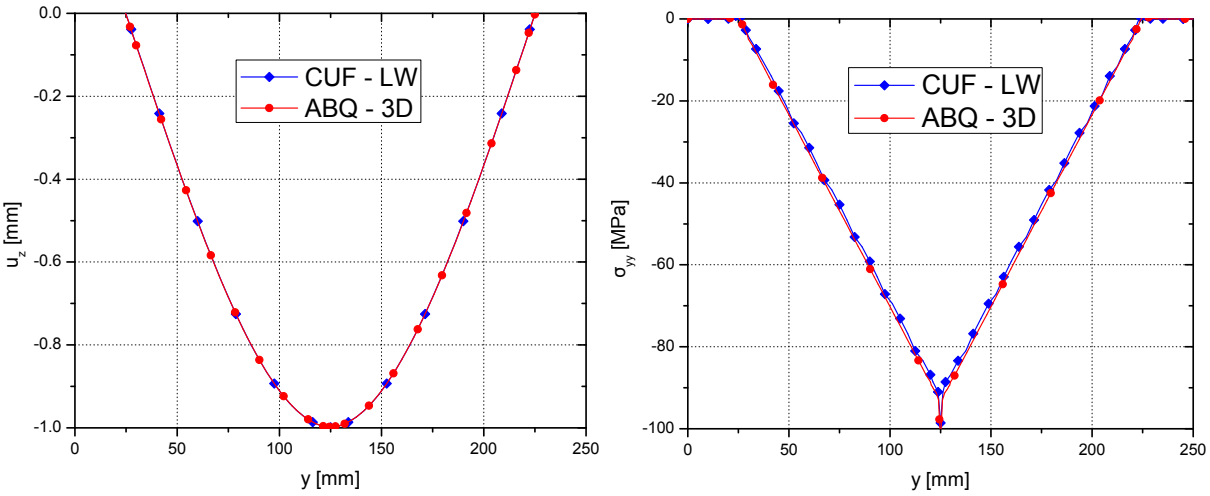

(a) Axial displacement u_z (b) Axial stress σ_{yy}

Fig. 4.10 Displacement and stress profile along the axis of the composite beam under 3-point bending.

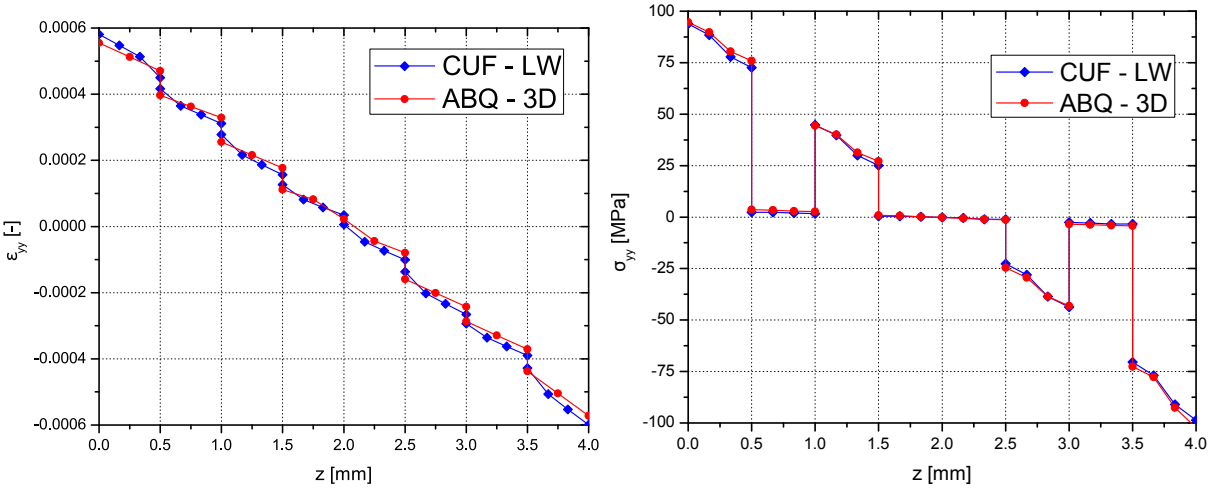

(a) Strain component ε_{yy} (b) Stress component σ_{yy}

Fig. 4.11 Axial strain and stress components at the midspan and through the thickness of the composite beam under 3-point bending.

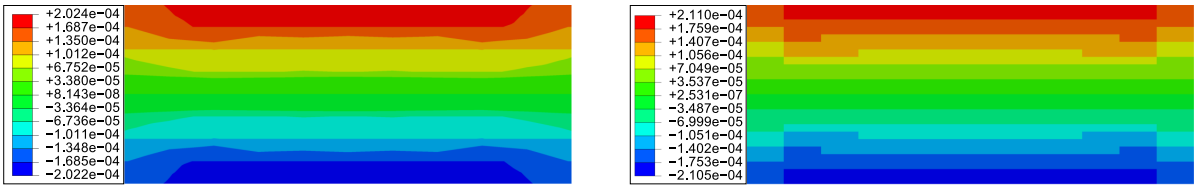

(a) ABAQUS-3D (b) CUF-LW

Fig. 4.12 Distribution of transverse normal strain ε_{33} at the beam cross-section (y = 150 mm).

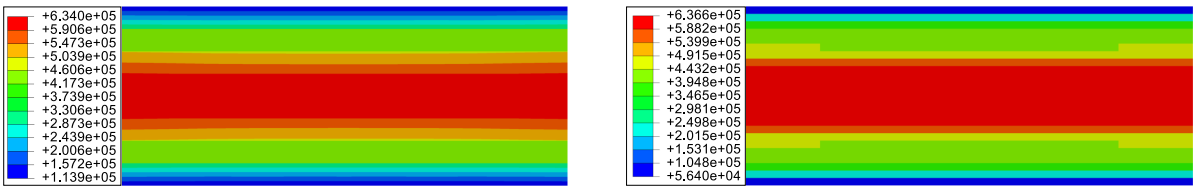

(a) ABAQUS-3D (b) CUF-LW

Fig. 4.13 Distribution of transverse shear stress σ_{23} at the beam cross-section (y = 150 mm).

4.3.3 Elastoplastic analysis of thin-walled beam under bending

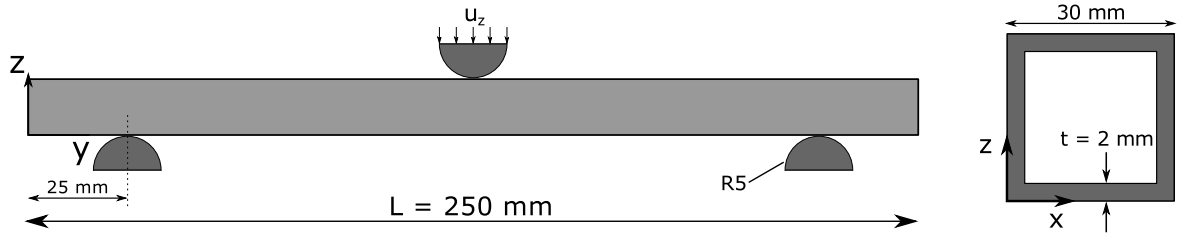

Fig. 4.14 3-point bending analysis of the thin-walled square-section tube.

The current example is a case of elastoplastic contact, where a square-section metal tube is subjected to the 3-point bending test. A schematic view of the setup is shown in Fig. 4.14. The beam spans 250 mm and has a square-section of edge length 30 mm with a thickness of 2 mm. It is supported by two rollers placed 25 mm from each end, while a third roller placed at the midspan applies the bending load on the top surface of the beam. Each roller has a radius of 5 mm, and is considered to be rigid. The beam is composed of an elastoplastic material with Young's modulus E = 68 GPa, Poisson's ratio $\nu = 0.33$ and initial yield stress $\sigma_{y0} = 29$ MPa. The elastoplastic behaviour of the material is described by the curve in Fig. 4.15, and is modelled using the von Mises plasticity theory with a piece-wise linear isotropic hardening law.

A series of numerical models were developed using 1D-CUF and ABAQUS-3D. The CUF

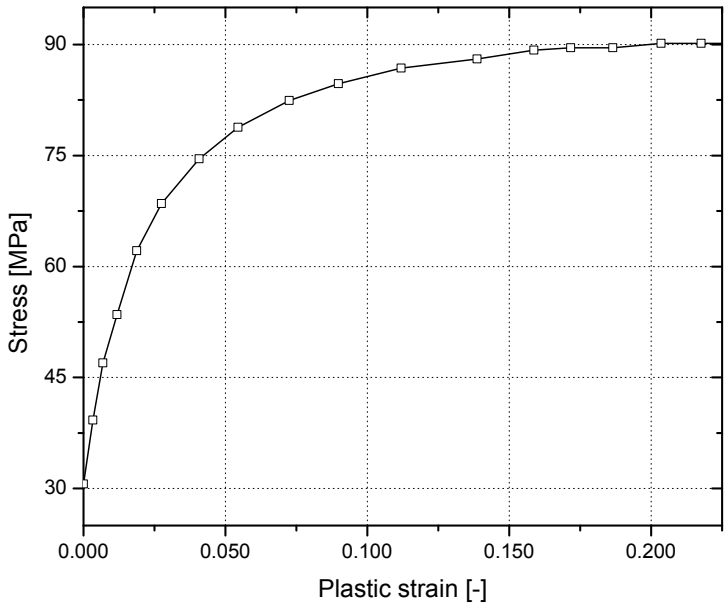

Fig. 4.15 Elastoplastic behaviour of the material used in the square-section tube.

models use 22 B4 elements to mesh the beam axis, while the cross-section is discretised with

20 L9 and 28 L9 expansions, respectively, which results in two models of varying levels of refinement. A mesh convergence study is performed in ABAQUS, resulting in three models of increasing refinement using 8-node linear hexahedral elements (C3D8R), as well as a fourth model discretised using 20-node quadratic hexahedral elements (C3D20R). The motivation behind the use of the quadratic-meshed model is to compare the use of high-order elements in standard FE modelling with those available in CUF. Table 4.5 summarises the discretisation and associated computational overheads of each numerical model. The vertical deflections u_z and axial stress σ_{yy} of the beam, at its top surface, have been plotted in Fig. 4.16 and Fig. 4.17, respectively. The equivalent plastic strain at the same domain has been plotted in Fig. 4.18, while a 3D distribution of the same at the contact region has been shown in Fig. 4.19. The following comments can be made:

1. The current assessment demonstrates the capability of the framework in handling cases of elastoplastic contact, with the quality of results comparable with 3D-FE solutions.

2. The importance of a sufficiently refined discretisation of the contact surface is seen in Fig. 4.16, in which the coarse 3D-FE analysis predicts a completely inaccurate deformation profile of the tube. The coarsely meshed contact surfaces leads to errors in the contact force computation, resulting in inaccurate deformation profiles.

3. The stress fields evaluated by the various 3D-FE models converge towards that predicted by CUF, as seen in Fig. 4.17, with the quadratic FE model being closest to the CUF values. A similar trend is observed in the predicted equivalent plastic strains, seen in Fig. 4.18.

4. The 1D-CUF model is approximately $13x$ smaller in computational size, and is about $4x$ faster than the refined 3D-FE model, for equivalent accuracy of the obtained solutions.

4.3.4 Global-local analysis of an elastoplastic beam under 3-point bending

The current numerical example demonstrates the use of the global-local technique, previously described in Chapter 3, as applied to the case of elastoplastic contact. Such a problem consists of multiple types of nonlinearities stemming from material behaviour and contact mechanics, which necessitates a high degree of structural discretisation, leading to computationally expensive models with long run-times. The ability to decouple the global structure and the local region of interest, with a fine discretisation applied only to the latter, can enable significant savings in computational effort and analysis times. The numerical assessment considers a

Table 4.5 Model details for the elastoplastic contact analysis of the square-section tube under 3-point bending.

Model	Discretisation of the square tube	Total DOF	Time (hh:mm:ss)
ABQ - Coarse	3,344 C3D8R	20,328	00:08:43
ABQ - Medium	76,464 C3D8R	307,152	00:57:00
ABQ - Refined	129,600 C3D8R	456,120	01:44:35
ABQ - Quadratic	19,008 C3D20R	315,360	00:50:45
CUF - 1D (20L9)	22 B4 - 20 L9	24,120	00:17:52
CUF - 1D (28L9)	22 B4 - 28 L9	33,768	00:26:04

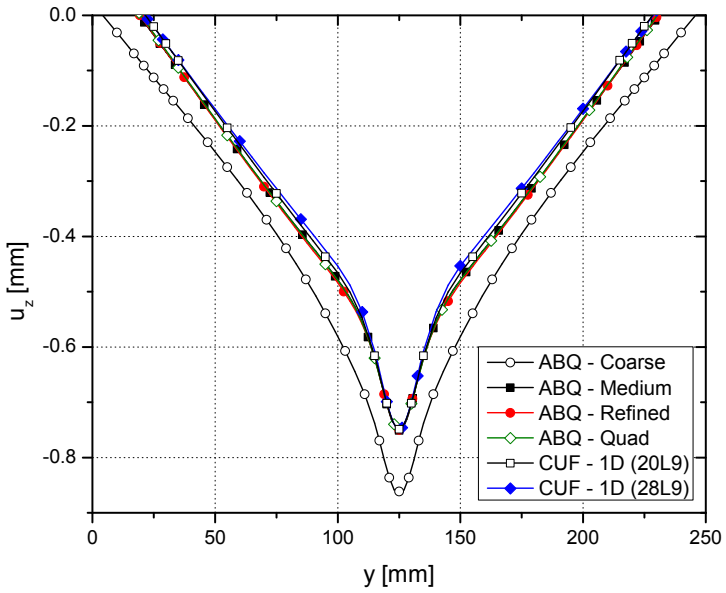

Fig. 4.16 Vertical deflection u_z at the top surface of the square-section tube under 3-point bending.

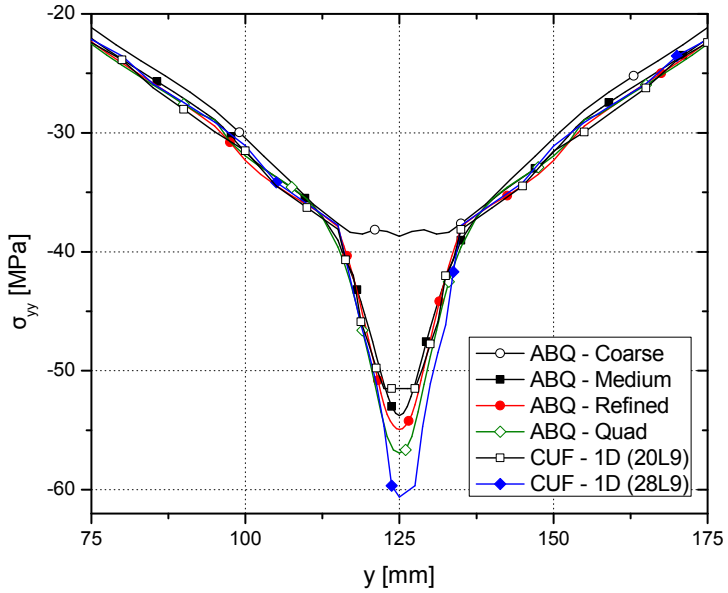

Fig. 4.17 Axial stress σ_{yy} at the top surface of the square-section tube under 3-point bending.

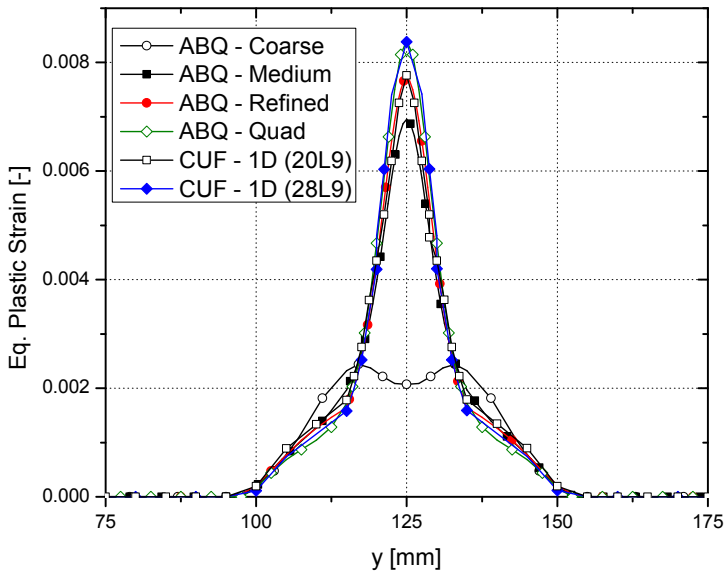

Fig. 4.18 Equivalent plastic strain at the top surface of the square-section tube under 3-point bending.

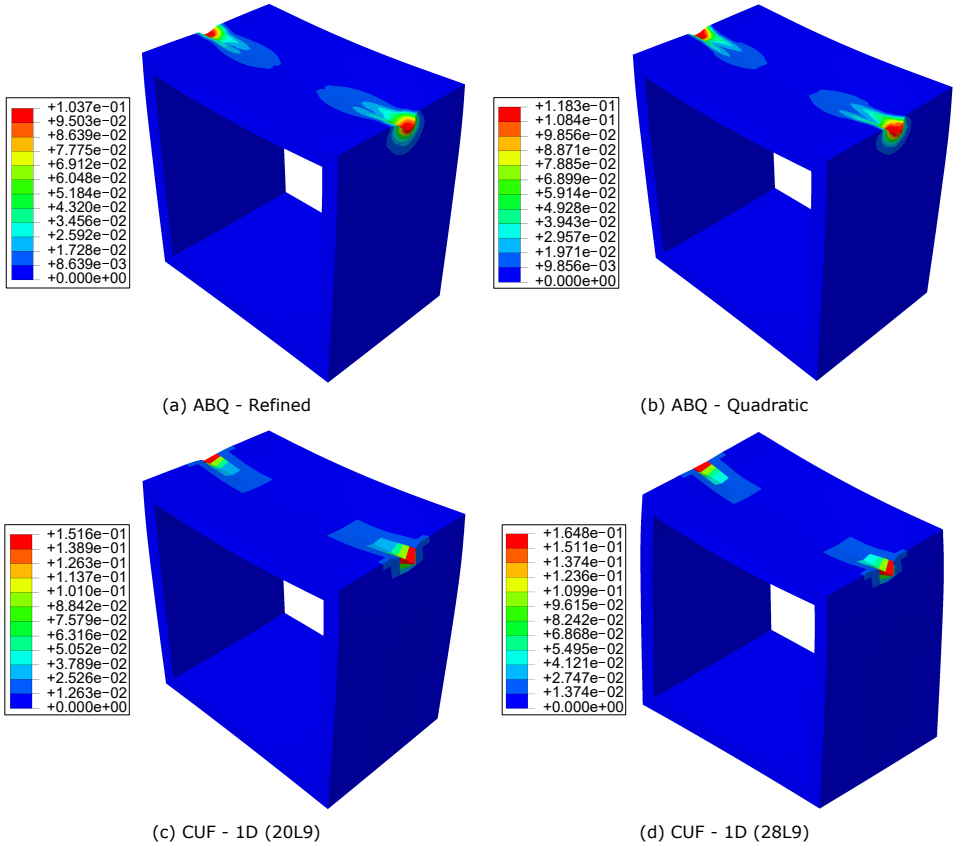

Fig. 4.19 Plastic strains developed at the indented region of the thin-walled tube.

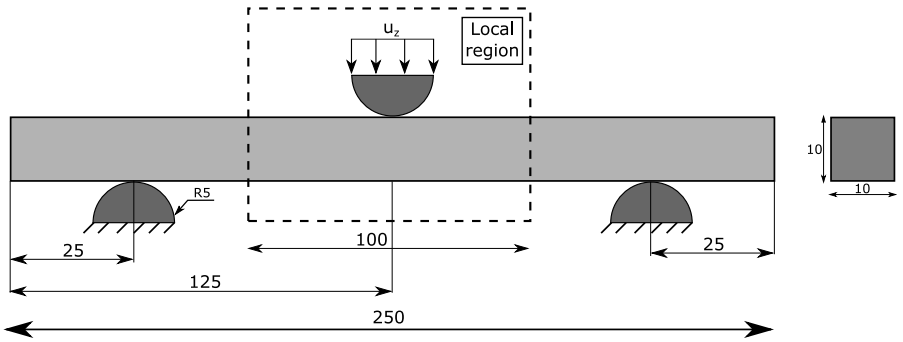

Fig. 4.20 Compact square-section elastoplastic beam subjected to 3-point bending. The local domain for global-local analysis has been highlighted.

metallic beam with a solid square cross-section subjected to the 3-point bending test, as shown in Fig. 4.20. The material properties described in Section 4.3.3 are retained and the rollers are modelled as rigid entities. The bending load is applied via a prescribed displacement u_z = -1.0 mm on the top roller. The setup described above is first analysed with CUF and ABAQUS using standard single-step approaches, where the global structure is modelled with a high level of discretisation. This provides a set of reference numerical solutions for comparison. The setup is then analysed using the global-local approach, where the global structure is first analysed in ABAQUS using a low-fidelity model, and the local region is subsequently modelled in CUF with prescribed displacements stemming from the global results. The domain of the local region to be analysed in CUF is highlighted in Fig. 4.20. Model details including the discretisation, DOF and analysis time are listed in Table 4.6. The axial deflection u_z and stress σ_{yy} of the beam, at its midspan, are shown in Fig. 4.21a and Fig. 4.21b, respectively. The plastic strains though the thickness of the beam, at its midspan, is plotted in Fig. 4.22. A 3D distribution of the plastic strains at the midspan of the beam, where permanent deformations occur due to contact, is shown in Fig. 4.23. The obtained results lead to the following comments:

1. The global-local technique is successfully applied to the elastoplastic contact problem, and the obtained results are in good agreements with reference high-fidelity global analyses in CUF and ABAQUS.

2. The coarsely meshed global 3D-FE model is able to evaluate the displacements correctly (Fig. 4.21a), but performs poorly in stress evaluation (Fig. 4.21b). However, when combined with high-fidelity CUF models, the results show a significant improvement.

3. The local CUF analysis requires about 31x fewer DOF and 5x less analysis time when comapred with refined global 3D-FEA, and has approximately half the computational cost of the refined global CUF model. Such improvements in the computational efficiency can be significant in the design process where the structure is subjected to various load cases, necessitating multiple runs of the analysis.

The global-local technique is thus demonstrated to be suitable for the computationally-efficient high-fidelity analysis of structures with complex nonlinear behaviour and loading conditions.

Table 4.6 Model details for the global-local analysis of the 3-point bending test of the square-section elastoplastic beam.

Model	Beam Discretisation	Total DOF	Time (s)
Reference global models			
ABQ - Refined	24,192 C3D8R	207,507	531
CUF - 1D	10 B4 - 16 L9	13,770	205
Global-Local analysis			
ABQ - Coarse (global)	3,024 C3D8R	30,453	43
CUF - 1D (local)	6 B4 - 16 L9	6,696	109

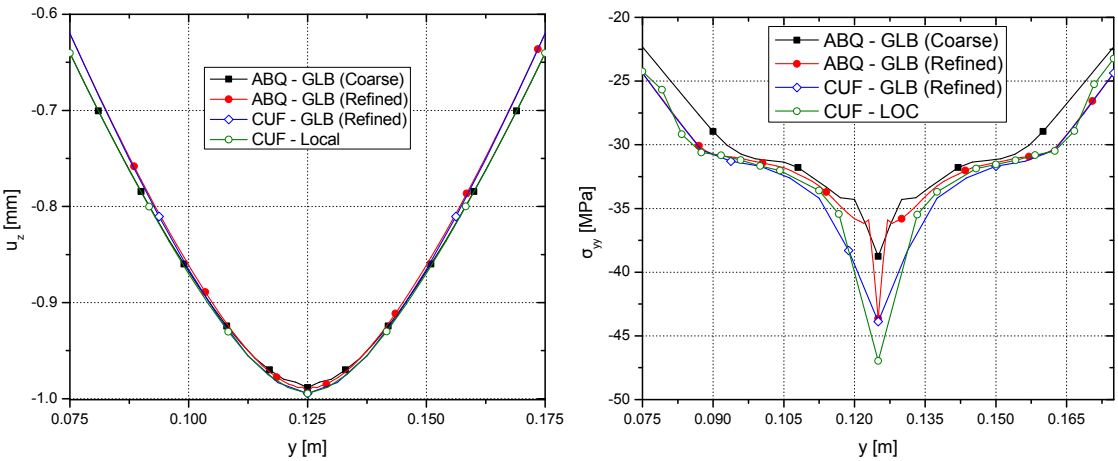

(a) Vertical displacement u_z (b) Axial stress σ_{yy}

Fig. 4.21 Vertical displacement u_z and axial stress σ_{yy} along the axis at the midspan of the compact-section beam under 3-point bending.

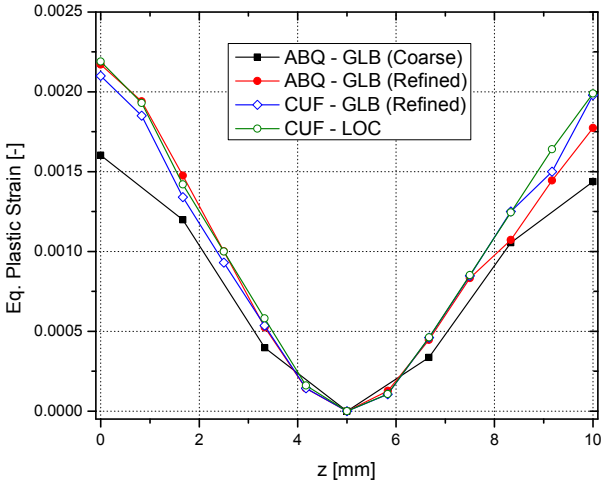

Fig. 4.22 Equivalent plastic strains through the thickness at the midspan of the compact-section beam under 3-point bending.

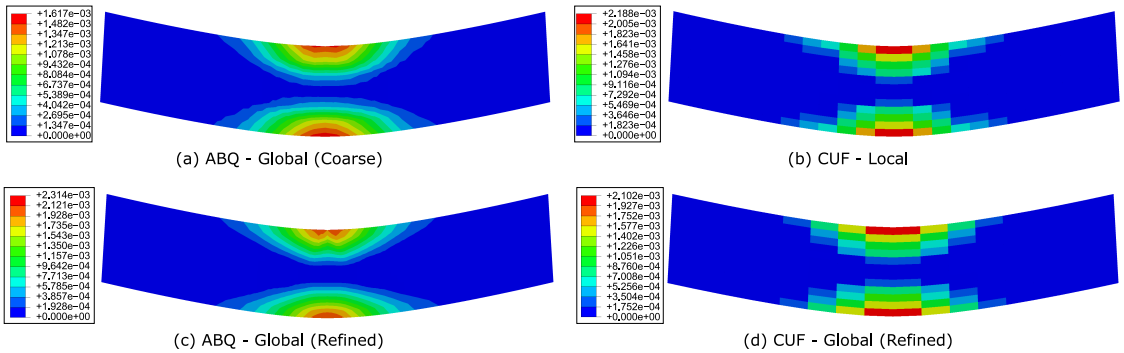

Fig. 4.23 Distribution of the equivalent plastic strains at the midspan of the compact-section beam under 3-point bending.

4.4 Numerical assessments of dynamic contact/impact problems

4.4.1 Impact between two rods

The present numerical assessment is a case of 1D-impact between two elastic rods, as shown in Fig. 4.24, and is based on the works of Carpenter et al. [18]. The objective of the current assessment is to provide basic verification of the dynamic contact/impact capabilities of the implemented framework within the context of explicit analysis. The setup consists of two identical rods, each prescribed with an initial velocity $v_0 = 5.136$ m/s, impacting each other. The rods are modelled as elastic, with Young's modulus E = 206.84 GPa and density $\rho = 7844\ kg/m^3$. The problem is analysed in CUF-Explicit using beam theories, where contact is modelled using node-to-node discretisation in combination with Lagrange multiplier enforcement. Analytical solutions and reference numerical results to the 1D impact problem are available in [18]. The displacement at the centre of the impact zone, as a function of time, is plotted in Fig. 4.25. The following comments are made:

1. The CUF predictions are in good agreement with reference analytical and numerical solutions, as seen in Fig. 4.25.

2. The obtained results provide verification for the correct implementation of the forward increment Lagrange multiplier algorithm for contact enforcement, and also demonstrates the capability of the CUF-Explicit framework in solving problems involving dynamic contact/impact.

The current numerical assessment is intended to provide a basic demonstration of dynamic contact/impact capabilities within the CUF framework, and its verification using analytical and numerical data available in the literature. Further numerical assessments which provide a comprehensive verification and validation of the impact capabilities of CUF models, especially concerning node-surface approaches, are presented in Chapter 6.

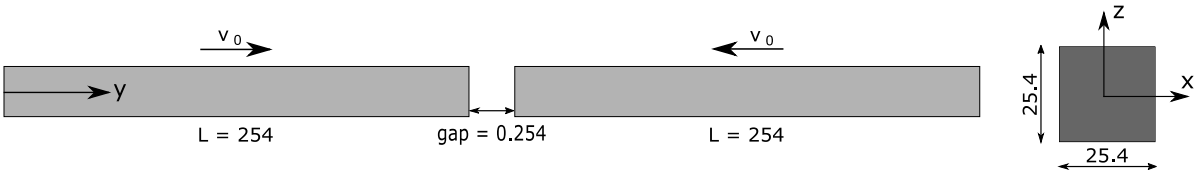

Fig. 4.24 A schematic representation of two elastic rods under impact.

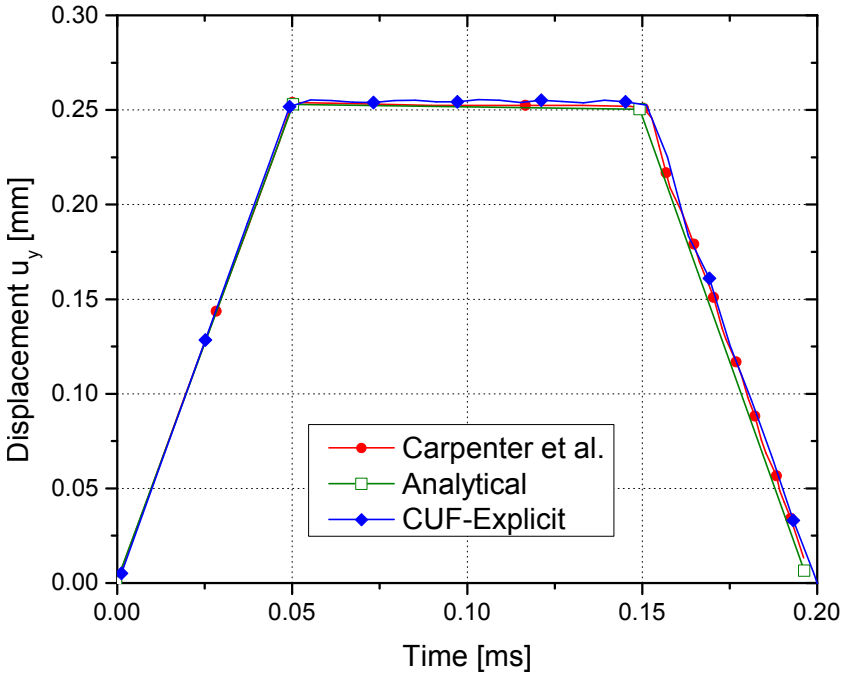

Fig. 4.25 Displacement at the centre of the impact zone of the the two rods as a function of time, as predicted by CUF-Explicit. Analytical and numerical solutions from Carpenter et al. [18] are overlaid for comparison.

4.5 Discussion

The present chapter provides a detailed description of the development and implementation of contact modelling techniques in the CUF framework. In particular, the node-to-node and node-to-surface contact discretisation approaches are presented, in combination with the penalty and Lagrange multiplier methods, respectively, for the enforcement of contact constraints. A series of numerical assessments are presented as verification cases, to demonstrate contact modelling capability in CUF. The first set of assessments consider static contact problems, and are solved implicitly using the Newton-Raphson solver described in Section 2.4.1. The first numerical example is the indentation of a doubly-clamped sandwich beam. Numerical models are developed using layer-wise 1D-CUF and 3D-FE. The CUF-LW and 3D-FE solutions are in perfect agreement with each other, while classical beam theories lead to significant errors in the deformation response. This is attributed to the fact that sandwich structures composed of foam cores and composite face-sheets have very high through-thickness gradients in material stiffness, leading to high gradients in the interlaminar strains, and requires refined kinematics for an accurate evaluation of the 3D strain fields. CUF-LW models based on Lagrange expansion functions are capable of resolving such complex strain fields, and can accurately account for through-thickness deformation of the sandwich beam. In contrast, 3D-FE models require a high

level of through-thickness discretisation with multiple elements used to model the thickness of each ply, in order to accurately compute the interlaminar fields. This leads to greatly increased computational costs which can be avoided by the use of refined 1D-CUF theories. The second assessment considers the 3-point bending analysis of a composite laminate, and demonstrates the capability of the CUF framework in modelling an arbitrary number of bodies and defining multiple contact pairs. The ability of CUF-LW models in accurately capturing through-thickness deformations and transverse stretching of the beam section is once again demonstrated. The CUF solutions are in very good agreement with reference 3D-FE models, and achieve an improvement of about $4x$ in terms of analysis time, and require approximately $11x$ fewer degrees of freedom.

The next set of assessments evaluate the capability of the framework in handling multiple types of nonlinearities, specifically contact problems involving physical nonlinearity. The analysed problem is the 3-point bending test of a thin-walled square-section tube composed of an elastoplastic material. Both CUF-LW and 3D-FE models are developed and the predicted responses of both approaches are compared. The CUF models provide an accurate prediction of the global deformation as well as localised plastic effects, whereas the 3D-FE models require a highly refined discretisation to achieve a solution of comparable quality. Similar to previous assessments, the refined 3D-FE model requires about $13x$ more degrees of freedom and $4x$ higher analysis time, compared to the most refined CUF model. The global-local technique is then applied to the case of elastoplastic contact, considering the 3-point bending test of a compact square-section elastoplastic beam. The global-local analysis results are in line with the global refined CUF and 3D-FE solutions, in terms of structural deformation as well as extent of plastic zone formation. The global-local approach provides a significant boost to computational efficiency, requiring about $31x$ fewer degrees of freedom and $5x$ less analysis time, compared to equivalent 3D-FE models.

The final numerical assessment is the initial verification of dynamic contact/impact modelling capabilities in CUF. This type of problem is analysed using the CUF-Explicit framework, a nonlinear explicit dynamics solver previously described in Section 2.4.2. The problem involves the low-velocity impact of two identical rods, modelled using CUF-LW theories, and the Forward Increment Lagrange Multiplier technique is used to enforce contact. The CUF predictions are in excellent correlation with analytical and numerical results available in the literature, and hence verifies CUF-Explicit for the analysis of problems involving dynamic contact/impact. The establishment of a robust numerical framework to handle this class of problems lead to the capability to investigate more complex numerical assessments, such as impact analysis of composite structures. This class of investigation is described in detail in Chapter 6 of the present thesis.

Chapter 5

Progressive damage analysis of fibre-reinforced composite laminates

This chapter introduces the CODAM2 composite material model and provides an overview of its formulation. The implementation of the damage model in the CUF-Explicit framework is described in detail, along with the use of linear-brittle softening curves to model the phenomenological effects of fibre compression. A selection of numerical assessments is presented, for composite structures in tension as well as in compression, as validation studies for a higher-order numerical platform for the mesoscopic progressive damage analysis of composite structures.[1]

5.1 The CODAM2 intralaminar damage model

The present work involves the implementation of the CODAM2 material model, where damage initiation and progression is evaluated within individual plies. The onset of damage is governed by failure criteria based on maximum stress values. The initiation criteria for damage in the fibre direction is given by

$$F_1 = \frac{\sigma_{11}}{X_T} \tag{5.1}$$

where X_T is the fibre tensile strength. σ_{11} is the stress along the fibre direction, and numerical subscripts indicate that the stress and strain fields have been rotated to the material

[1] Parts of this chapter have been published in the following:

1. Nagaraj, M. H., Reiner, J., Vaziri, R., Carrera, E., & Petrolo, M. (2020). Progressive damage analysis of composite structures using higher-order layer-wise elements. Composites Part B: Engineering, 190, 107921.

coordinate system. Damage initiation transverse to the fibre is given by the Hashin quadratic failure theory [64] as

$$F_2 = \left(\frac{\sigma_{22}}{Y_T}\right)^2 + \left(\frac{\tau_{12}}{S_L}\right)^2 \tag{5.2}$$

where Y_T is the transverse tensile strength and S_L is the in-plane shear strength. The equivalent strain measures ε_1^{eq} and ε_2^{eq}, parallel and transverse to the fibre respectively, are given by

$$\varepsilon_1^{eq} = |\varepsilon_{11}| \tag{5.3}$$

$$\varepsilon_2^{eq} = \sqrt{(\gamma_{12}^e)^2 + (\varepsilon_{22})^2} \tag{5.4}$$

where γ_{12}^e is the elastic component of the in-plane shear strain. The corresponding equivalent stress measures are defined as

$$\sigma_1^{eq} = \sigma_{11} \tag{5.5}$$

$$\sigma_2^{eq} = \frac{\tau_{12}\gamma_{12}^e + \sigma_{22}\varepsilon_{22}}{\sqrt{(\gamma_{12}^e)^2 + (\varepsilon_{22})^2}} \tag{5.6}$$

The damage initiation strains, i.e. the strain values at the point of failure initiation (F_1, F_2 = 1), are calculated as

$$\varepsilon_\alpha^i = \varepsilon_\alpha^{eq}|_{F_\alpha=1}, \quad \alpha = 1,2 \tag{5.7}$$

The corresponding strain values when the material is completely degraded, i.e. fully damaged, is then computed by

$$\varepsilon_1^s = \frac{2g_1^f}{X_T} \quad and \quad \varepsilon_2^s = \frac{2g_2^f}{T} \tag{5.8}$$

where the fracture energy density is denoted by g_α^f, and $T = \sigma_2^{eq}|_{F_2=1}$ is the maximum value of the equivalent transverse stress σ_2^{eq}. Mesh dependency is addressed by the rational scaling of the fracture energy G_α^f, following the crack-band approach [6]

$$g_\alpha^f = \frac{G_\alpha^f}{l^*}, \quad \alpha = 1,2 \tag{5.9}$$

This approach requires the definition of a characteristic length parameter of the element, denoted by l^* in Eq. 5.9. The current work considers $l^* = (V_{GP})^{\frac{1}{3}}$, where V_{GP} is the volume associated with a Gauss point within the element domain. The local form of the CODAM2 model is used in the present work, which means that the longitudinal as well as transverse fracture energy can be scaled. The magnitude of damage is quantified using the damage parameters ω_1 (longitudinal direction) and ω_2 (transverse direction), which are computed as

$$\omega_\alpha = \left(\frac{< \varepsilon_\alpha^{eq} - \varepsilon_\alpha^i >}{\varepsilon_\alpha^s - \varepsilon_\alpha^i} \right) \left(\frac{\varepsilon_\alpha^s}{\varepsilon_\alpha^{eq}} \right), \quad \alpha = 1,2 \tag{5.10}$$

where $< \cdot >$ is the Macaulay bracket. The damage parameters ω_α is used to compute the 3D secant material matrix, in the degraded state, as follows [125]

$$\mathbf{C}^{dam} = \frac{1}{\Delta} \begin{bmatrix} (1-R_2\nu_{23}\nu_{32})R_1E_1 & (\nu_{21}+\nu_{23}\nu_{31})R_1R_2E_1 & (\nu_{31}+R_2\nu_{21}\nu_{32})R_1E_1 & 0 & 0 & 0 \\ & (1-R_1\nu_{31}\nu_{13})R_2E_2 & (\nu_{32}+R_1\nu_{31}\nu_{12})R_2E_2 & 0 & 0 & 0 \\ & & (1-R_1R_2\nu_{21}\nu_{12})E_3 & 0 & 0 & 0 \\ & & & \Delta R_1R_2G_{12} & 0 & 0 \\ & sym. & & & \Delta G_{23} & 0 \\ & & & & & \Delta G_{13} \end{bmatrix} \tag{5.11}$$

where

$$\Delta = 1 - R_2\nu_{23}\nu_{32} - R_1R_2\nu_{12}\nu_{21} - 2R_1R_2\nu_{31}\nu_{12}\nu_{23} - R_1\nu_{31}\nu_{13} \tag{5.12}$$

and the stiffness reduction factor R_α is

$$R_\alpha = (1-\omega_\alpha), \quad \alpha = 1,2 \tag{5.13}$$

Finally, the stress state is computed as

$$\boldsymbol{\sigma} = \mathbf{C}^{dam}\boldsymbol{\varepsilon} \tag{5.14}$$

5.1.1 In-plane shear nonlinearity

It has been experimentally observed that unidirectional composite laminates exhibit significant nonlinear in-plane shear behaviour [80]. Such effects should therefore be accounted for within material models to retain accuracy of the resulting analysis. The current section describes the modelling of in-plane shear nonlinearity in the CODAM2 material model [125].

Prior to matrix damage initiation, the shear stress-strain relation is given by

$$\tau_{12} = \begin{cases} \frac{|\gamma_{12}|}{\gamma_{12}}\tau(|\gamma_{12}|), & \text{for } |\gamma_{12}| = \gamma_{12}^{*} \\ \frac{|\gamma_{12}|}{\gamma_{12}}G_{12}^{0}\langle|\gamma_{12}| - \gamma_{12}^{p}\rangle, & \text{for } |\gamma_{12}| < \gamma_{12}^{*} \end{cases} \tag{5.15}$$

where $\tau(|\gamma_{12}|)$ is the experimentally obtained nonlinear shear behaviour, and initial shear modulus is denoted by G_{12}^{0}. $\langle\cdot\rangle$ represents the Macaulay operator, and γ_{12}^{*} is the maximum value of computed shear strain in time. The inelastic shear strain γ_{12}^{p} is evaluated as

$$\gamma_{12}^{p} = \gamma_{12}^{*} - \tau_{12}^{*}/G_{12}^{0} \tag{5.16}$$

where τ_{12}^{*} is the corresponding shear stress associated with γ_{12}^{*}. Matrix damage initiation occurs when Eq. 5.2 reaches unity, i.e. $F_2 = 1.0$. The equivalent strain in the transverse direction (see Eq. 5.4), which is the matrix damage driver, considers only the elastic component of the shear strain, since only the elastic internal energy contributes to fracture. This requires the elastic shear strain, which is evaluated as

$$\gamma_{12}^{e} = \gamma_{12} - \gamma_{12}^{p}|_{F_2=1} \tag{5.17}$$

where $\gamma_{12}^{p}|_{F_2=1}$ is the inelastic shear strain at the initiation of matrix damage. After the onset of matrix damage, the shear stress is computed as

$$\tau_{12} = R_{12}G_{12}^{0}(\gamma_{12} - \gamma_{12}^{p}|_{F_2=1}) \tag{5.18}$$

5.1.2 Post-peak fibre softening under compression

The formulation presented in Section 5.1 constitutes the basic material model with a bilinear formulation, where the post-peak softening is modelled as a straight line. This is sufficient for unidirectional composites under tension, but leads to significant limitations when the composite is subjected to axial compressive loads. This is due to the micro-buckling of fibres under compression, leading to the eventual formation of kink-bands. This process is usually defined by a sudden load drop due to fibre buckling immediately after the peak load, and is followed by a plateauing of the residual stress, indicating a stable configuration of the buckled fibres. Such complex phenomena cannot be described by simple bilinear damage models, leading to severe shortcomings in the accurate predictive capabilities of numerical tools using such material models. One approach to take into account the effect of such phenomena is via the use of different classes of softening curves to describe the post-damage response of the fibre, when the structure is loaded in compression. Popular techniques include the use of bilinear or

trilinear post-peak fibre softening curves [118, 155]. Following this approach, the current work considers a bilinear post-peak softening model for the fibre under compression, specifically the 'linear-brittle' curve which is characterised by a sudden stress drop following the peak, followed by a steady residual stress until final failure. The magnitude of the residual stress is computed as a percentage of the peak stress, and varying this parameter leads to a family of curves, which is then calibrated for the specific composite material system under consideration. A series of linear-brittle fibre softening curves, along the the basic linear curve, is plotted in Fig. 5.1. It is noted that in each case, the area under the curve, which represents the fibre fracture energy, remains constant.

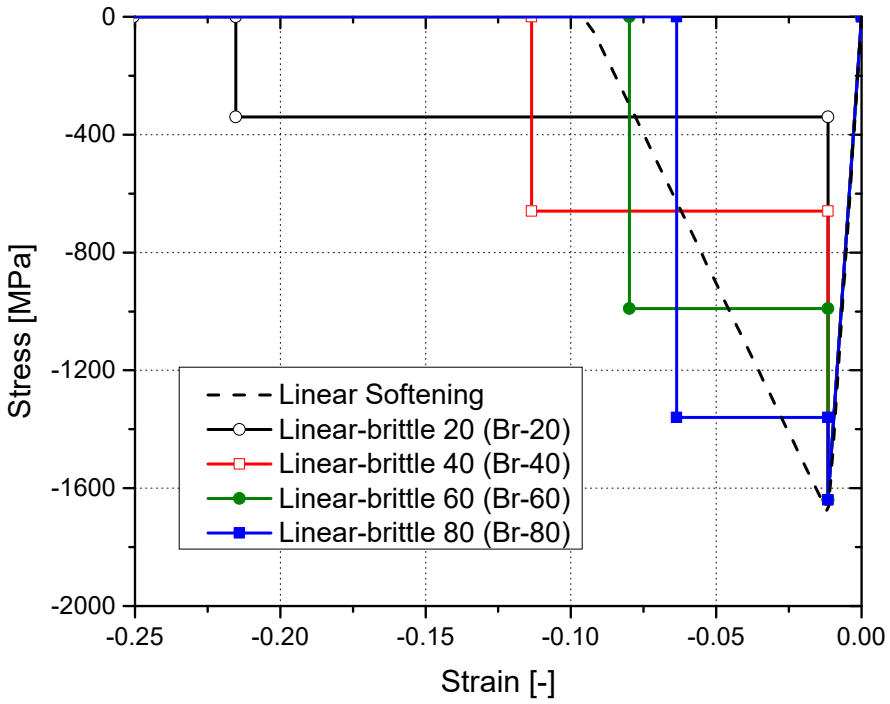

Fig. 5.1 Linear and linear-brittle post-peak softening curves to model compressive fibre damage. The number indicates the percentage of the peak strength which remains as a residual stress plateau.

5.2 Numerical assessments of progressive tensile damage

This section presents a set of numerical examples as validation cases, to ensure the correct implementation of the CODAM2 model for progressive damage analysis under tensile loads. The material system considered for all cases is IM7/8552 carbon-fibre reinforced plastic (CFRP),

with a nominal ply thickness of 0.125 mm, and its elastic and strength properties are listed in Table 5.1.

Table 5.1 Elastic and strength properties of IM7/8552 CFRP [68].

E_1 [GPa]	E_2 [GPa]	E_3 [GPa]	G_{12} [GPa]	G_{13} [GPa]	G_{23} [GPa]	ν_{12}	ν_{13}	ν_{23}
165.0	9.0	9.0	5.6	5.6	2.8	0.34	0.34	0.5

X_T [MPa]	Y_T [MPa]	S_L [MPa]	G_1^f $[kJ/m^2]$ [119]	G_2^f $[kJ/m^2]$ [125]
2560.0	73.0	90.0	120.0	2.6

5.2.1 Verification: Single-element analysis

Single-element tests are widely used during the development of material models since they are a suitable method to verify the correctness of the implementation. In the case of damage modelling of composites, they enable the independent evaluation of each failure mode. The current set of assessments consider a 1 mm $\times$ 1 mm domain modelled using a single L4 element within the plane, and a linear expansion (LE1) to model the ply thickness, which is 0.125 mm. Such a domain is subjected to uni-axial strain, and the resulting stress is evaluated. Such a discretisation is used to ensure kinematic compatibility with the 8-node linear hexahedral element of classical 3D-FEA. The first case considers loading in the fibre direction, which results in purely fibre damage. This is then followed by loading in a direction transverse to the fibre, resulting in matrix-dominated damage. The stress-strain curves for these loading cases is shown in Fig. 5.2. Next, a single-element laminate is considered, with a stacking sequence of $[90/45/0/-45]_{2s}$, under the same loading condition. In this case, reference numerical results from LS-Dyna are available for comparison [115]. The stress-strain curve for the single-element laminate is plotted in Fig. 5.3.

The following observations are made:

1. The bilinear stress-strain curve predicted by the single-element analysis, shown in Fig. 5.2 is consistent with the CODAM2 formulation.

2. The peak stress values observed in the single-element test, under longitudinal and transverse loading, is in agreement with the fibre and matrix strengths which are provided as material inputs.

3. The stress-strain response of the single-element laminate is in good general agreement with reference LS-Dyna results as shown in Fig. 5.3.

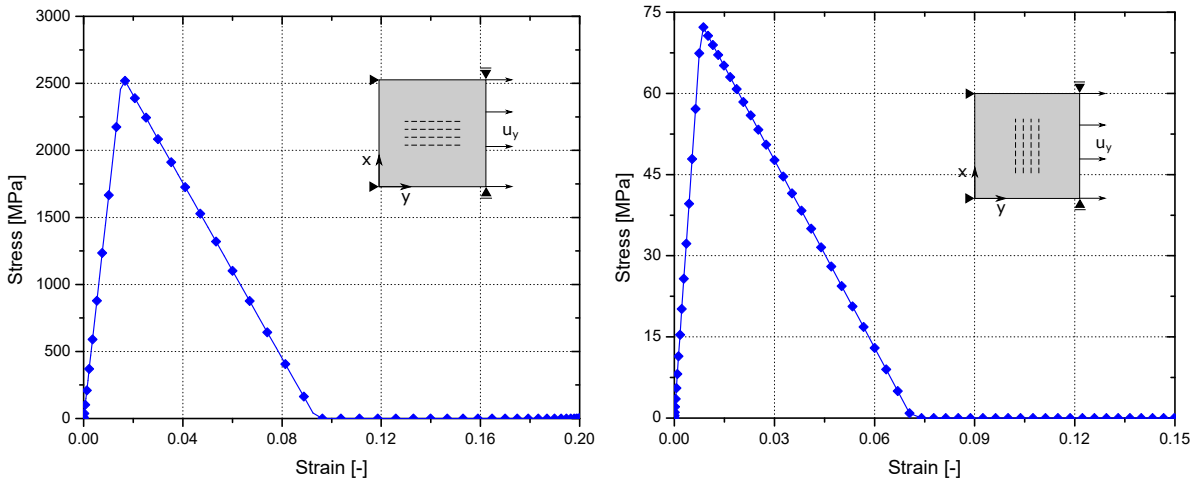

(a) Longitudinal loading (fibre) (b) Transverse loading (matrix)

Fig. 5.2 Predicted response of the single-element under uni-axial tensile strain.

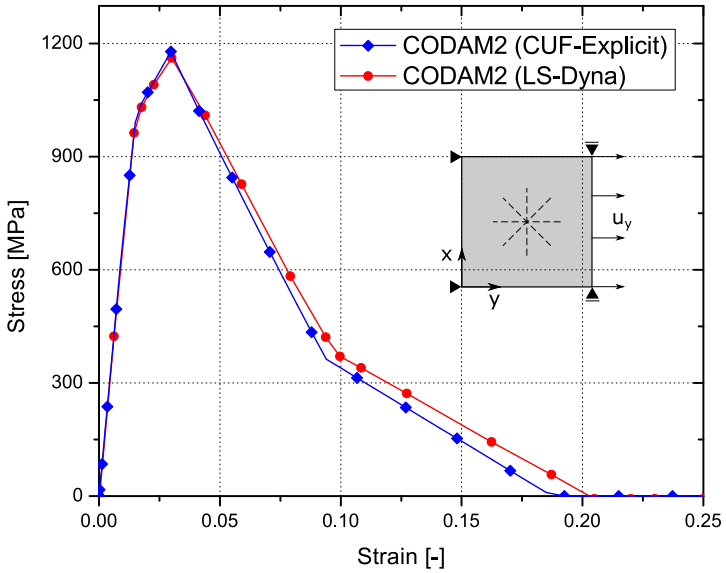

Fig. 5.3 Predicted response of the single-element $[90/45/0/-45]_{2s}$ laminate under uni-axial tensile strain, with reference LS-Dyna results [115].

5.2.2 Tension test of notched laminates

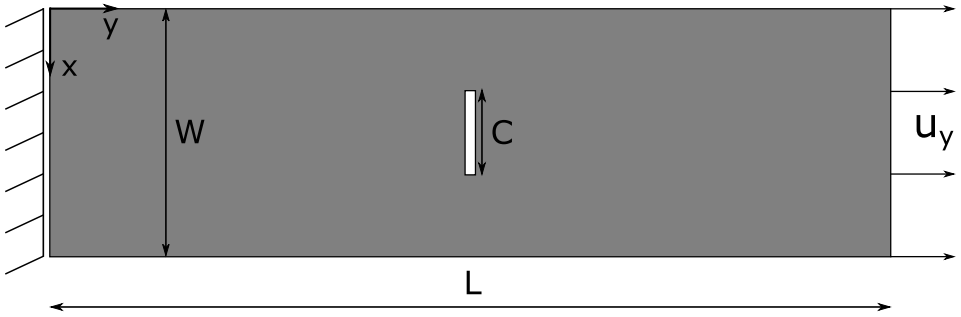

Fig. 5.4 A schematic representation of the $[45/90/-45/0]_{4s}$ centre-notched tension specimen with the applied boundary conditions.

The current set of numerical assessments evaluates the capabilities of high-order structural models towards the progressive damage analysis of coupon-level composites. The centre-notched tensile specimen, shown in Fig. 5.4, is considered at various length scales listed in Table 5.2. The laminate has a stacking sequence of $[90/45/0/-45]_{4s}$, with a total thickness of 4 mm. The structure is fixed at one end, and the tensile load is applied in the form of prescribed displacements at the opposite end.

Table 5.2 Analysed scales of the centre-notched laminate in tension.

Scale	Notch Length C [mm]	Specimen Width [mm]	Specimen Length [mm]
1	3.2	15.9	63.5
2	6.4	31.8	127.0
4	12.7	63.5	254.0
8	25.4	127.0	508.0
16	50.8	254.0	508.0
24*	76.2	381.0	1016.0

* Virtual test sample

The first study considers the scale-8 specimen, and a mesh convergence study is undertaken using successively refined 2D-CUF models, in terms of both in-plane and through-thickness discretisation. The resulting stress-strain curves have been plotted in Fig. 5.5. The 132 Q9 mesh is deemed sufficient based on the convergence study, and is used for subsequent analyses. Next, the peak strengths of the various specimen scales are predicted, as shown graphically in Fig. 5.6. In both studies, experimental data from [154] and numerical results from [115]

have been included for comparison. The final study investigates the computational overheads associated with the various numerical approaches across the specimen scales, in terms of DOF and analysis time, and are shown in Fig. 5.7, for the case of CUF and LS-Dyna models. Based on the obtained results, the following observations are made:

1. The proposed approach based on 2D-CUF models is capable of accurately predicting the tensile failure strength of coupon-level composite structures, as seen in 5.5, when compared to available experimental data.

2. The current approach is also capable of predicting size-effects in scaled composite coupons, where the tensile strength is inversely proportional to the specimen size, and is consistent with experimental observations as seen in Fig. 5.6.

3. The relaxed aspect-ratio constraints of CUF models, owing to the use of higher-order structural theories, enables the use of the same finite element mesh for successively scaled composite specimens. This leads to significant savings in computational size, see Fig. 5.7a, and analysis time, see Fig. 5.7b, compared to standard FE approaches.

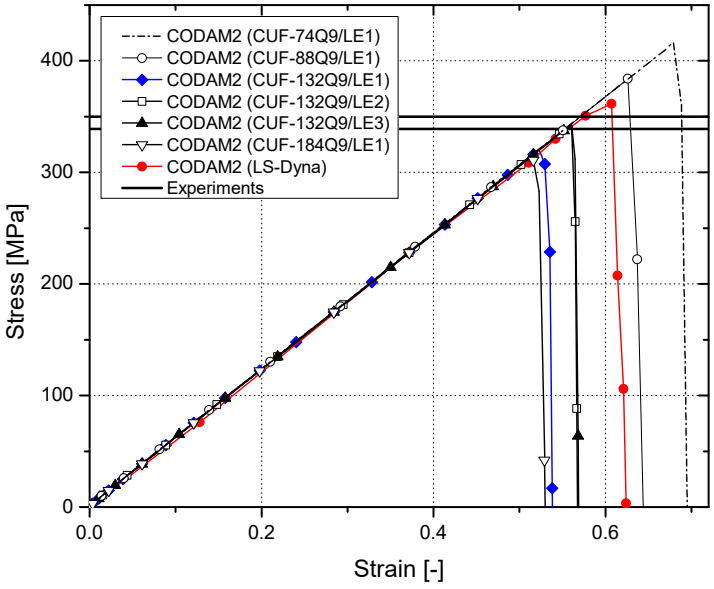

Fig. 5.5 Stress-strain curves obtained as a result of the mesh convergence study of the scale-8 CNT specimen. Maximum and minimum values of the experimentally obtained peak strengths (horizontal black lines) [154] and reference numerical curves [115] are also reported.

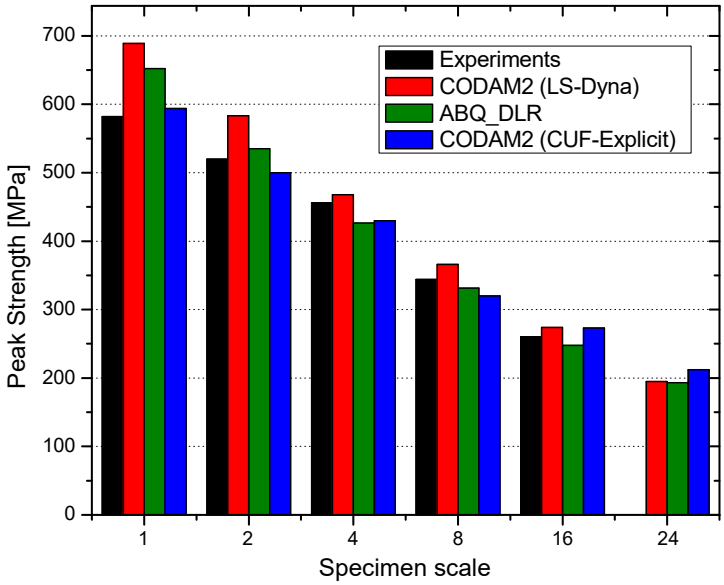

Fig. 5.6 Predicted peak strengths across the CNT specimen scales according to CUF, experimental data [154] and reference numerical simulations [115].

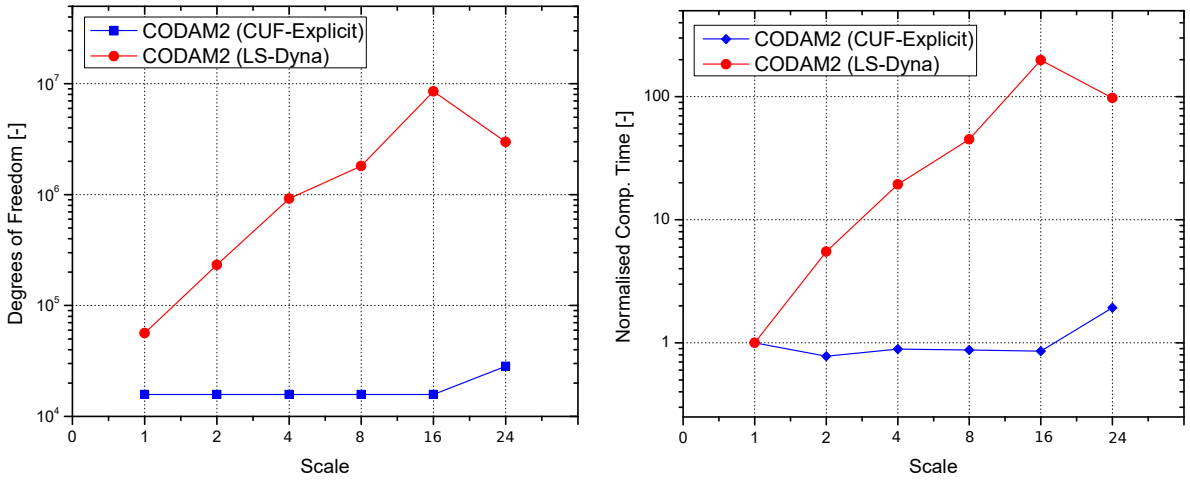

(a) DOF (b) Normalised analysis time

Fig. 5.7 Computational costs associated with the numerical analysis of centre-notched tensile specimens across the scales.

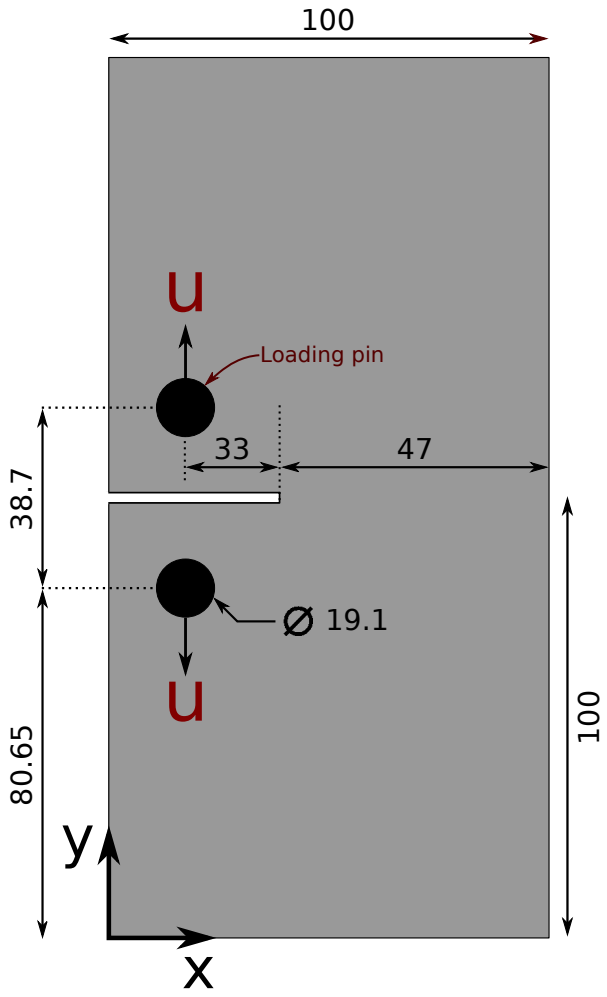

Fig. 5.8 Geometry and loading conditions of the over-height compact tension specimen (dimensions in mm).

5.2.3 Analysis of over-height compact specimen in tension

The current example consists of the analysis of an over-height compact tension (OCT) specimen, considering a dispersed-ply laminate with a $[90/45/0/-45]_{4s}$ stacking sequence. The specified geometry and layup leads to stable crack growth with minimum delamination, and hence is selected for the present assessment, where the focus is on intralaminar damage initiation and progression. The structure of the OCT specimen, with applied loading conditions, is presented in Fig. 5.8. Rigid loading pins are built into the laminate structural model, and the load is applied via prescribed displacements u = 1.0 mm on each pin. The 2D-CUF model consists of 392 Q9 elements modelling the in-plane structural geometry, and three thickness expansions of increasing polynomial refinement, i.e. LE1, LE2 and LE3, are considered. The current analysis is based on the numerical assessments of Reiner et al. [115]. Experimental data is available from [162].

The analysis results are presented in the form of force-displacement plots, shown in Fig. 5.9, along with the reference numerical and experimental curves. The predicted crack growth is plotted in Fig. 5.10, which is measured by the amount of saturated fibre damage present in the 0° ply of the laminate. Contour plots of saturated longitudinal (fibre) damage in the 0° ply and transverse (matrix) damage in the 0° ply of the composite laminate are provided in Fig. 5.11. The following comments are made:

1. The predicted force-displacement response of the CUF models are in reasonably good agreement with experimental data, see Fig. 5.9, thus validating the CUF framework for progressive damage analysis.

2. The over-prediction of the peak loads by the CUF models is attributed to the absence of delamination. This is consistent with reference LS-Dyna simulations, in which delamination was not considered.

3. Numerical oscillations are present in the obtained solutions and is a consequence of higher-order (Q9) elements as well as explicit solution schemes. The use of numerical damping techniques such as the Bulk Viscosity Method (BVM) may be beneficial in obtaining smooth results.

4. The fibre and matrix damage morphology predicted by the CUF models, shown in Fig. 5.11, is consistent with the predictions of reference LS-Dyna simulations, and provides further verification for the progressive damage capabilities of the current approach.

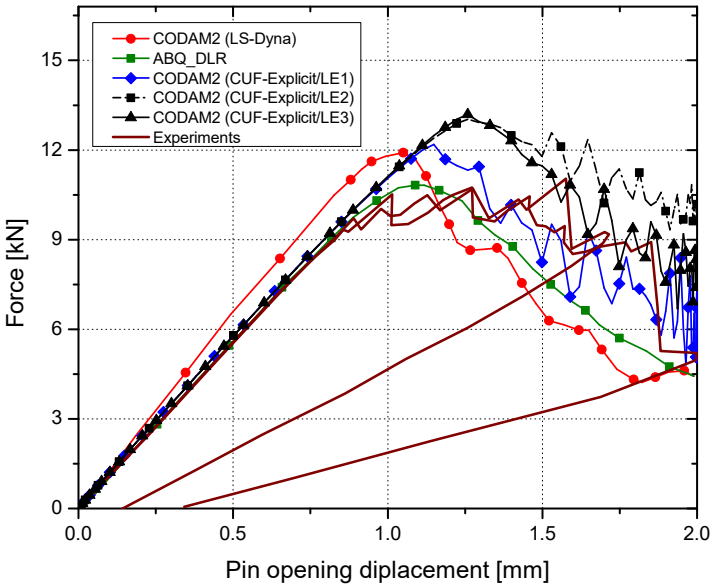

Fig. 5.9 Force-displacement plot of the OCT specimen as predicted by the CUF models. Reference numerical results from [115] and experimental data from [162] are also overlaid.

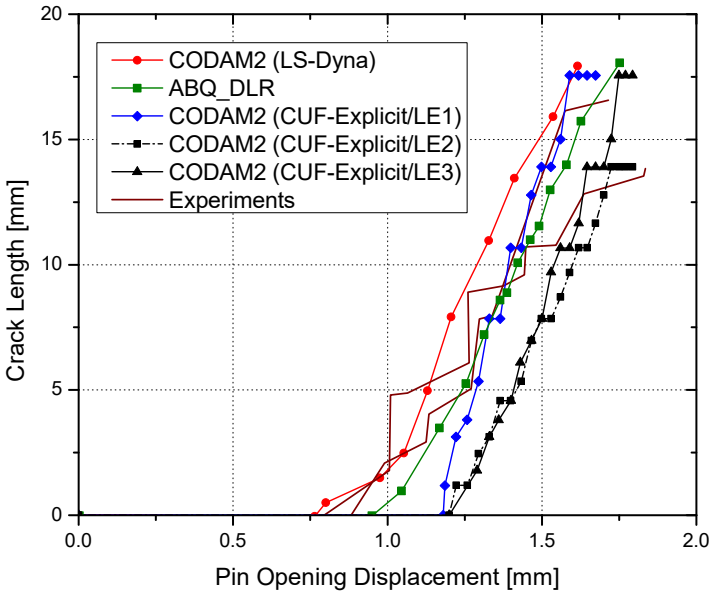

Fig. 5.10 Crack growth in the 0° ply of the OCT specimen as predicted by the CUF models. Reference numerical results from [115] and experimental data from [162] are also overlaid.

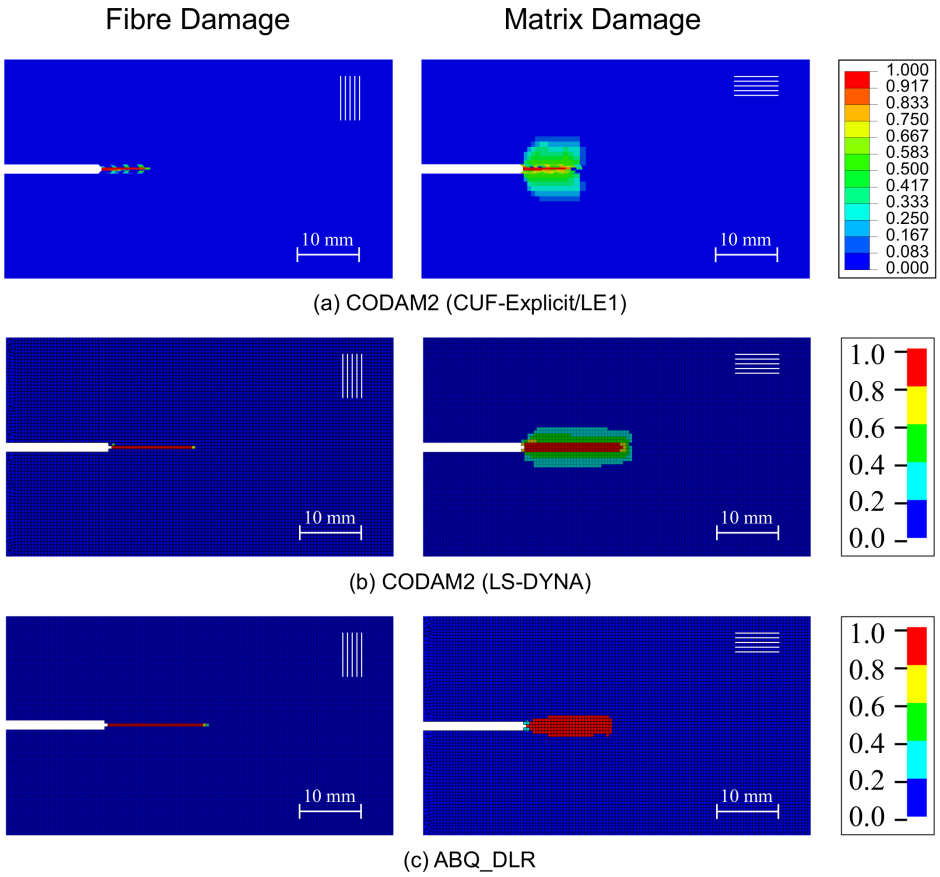

Fig. 5.11 Saturated fibre (0° ply) and matrix (90° ply) damage in the OCT specimen at a POD of 1.5 mm, as predicted by (a) CUF-2D, (b) LS-DYNA, and (c) ABQ-DLR models.

5.3 Numerical assessments of progressive damage in compression

This section presents a set of numerical examples as validation cases, to ensure the correct implementation of the CODAM2 model for progressive damage analysis under compressive loads. The material system considered for all cases is IM7/8552 carbon-fibre reinforced plastic (CFRP), with a nominal ply thickness of 0.125 mm, and its elastic and strength properties are provided in Table 5.3.

Table 5.3 Elastic and strength properties of IM7/8552 CFRP.

E_1 [GPa]	E_2 [GPa]	E_3 [GPa]	G_{12} [GPa]	G_{13} [GPa]	G_{23} [GPa]	ν_{12}	ν_{13}	ν_{23}
150.0	11.0	11.0	5.8	5.8	2.9	0.34	0.34	0.48
X_T [MPa]	X_C [MPa]	Y_T [MPa]	Y_C [MPa]	S_{12} [MPa]	G_1^T $[kJ/m^2]$	G_2^T $[kJ/m^2]$	G_1^C $[kJ/m^2]$	G_2^C $[kJ/m^2]$
2560.0	1690.0	73.0	250.0	90.0	120.0	2.6	80.0	4.2

5.3.1 Verification: Single-element analysis

The basic verification of the CODAM2 implementation in CUF-Explicit is performed via a series of single-element analyses, since they are a convenient way of investigating each failure mode in an independent manner. The single-element consists of a 1 mm $\times$ 1 mm unidirectional lamina, which is subjected to uni-axial compression. The lamina is modelled using a single linear Q4 element within the plane, and a single linear (LE1) expansion models the ply thickness. The model is first loaded in the fibre (0°) direction, leading to fibre-dominated damage. The resulting stress-strain response is plotted in Fig. 5.12a. Next, the same lamina is loaded in compression transverse to the fibre (90°), resulting in matrix-dominated damage, and the stress-strain response is shown in Fig. 5.12b. Finally, a single-element quasi-isotropic laminate is considered, whose stacking sequence is given by $[90/45/0/-45]_{2s}$. The predicted response for this assessment is presented in Fig. 5.13, with reference LS-DYNA simulation results overlaid for comparison. The following comments are made

1. The predicted results are in agreement with the bilinear formulation of the basic CODAM2 material model, as seen in Fig. 5.12a and Fig. 5.12b. Furthermore, the peak stress obtained in both cases is equal to the material strength values provided as an input.

2. The stress-strain curve predicted by the CUF approach correlates well with the LS-DYNA results, for the case of the quasi-isotropic $[90/45/0/-45]_{2s}$ single-element laminate.

The differences in the two curves is attributed to the structural models used in the two numerical approaches.

The single-element tests thus demonstrate the basic verification of the implementation of the CODAM2 model for compressive damage analysis, within the CUF-Explicit framework.

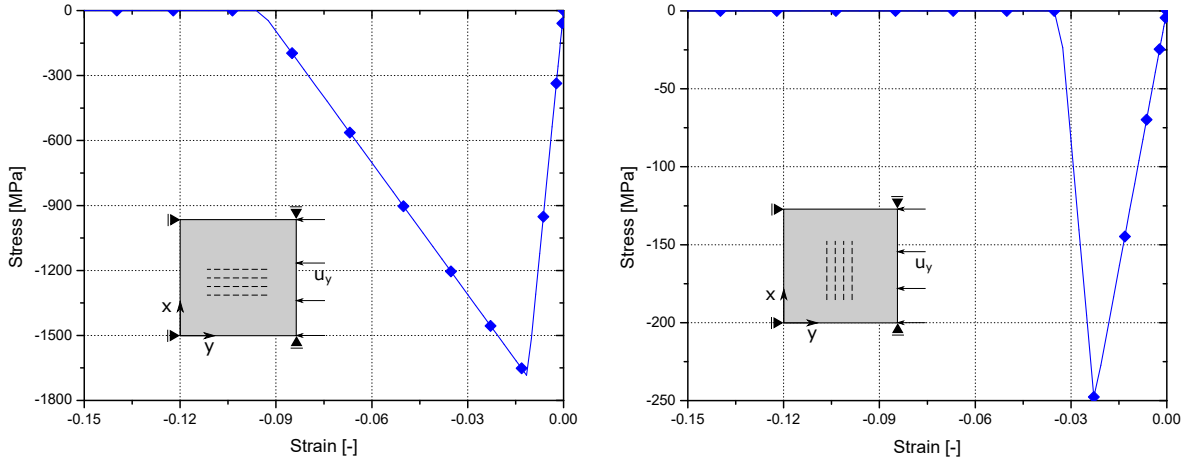

(a) Longitudinal loading (fibre) (b) Transverse loading (matrix)

Fig. 5.12 Predicted response of the single-element lamina under uni-axial compressive strain. (a) 0° orientation, and (b) 90° orientation.

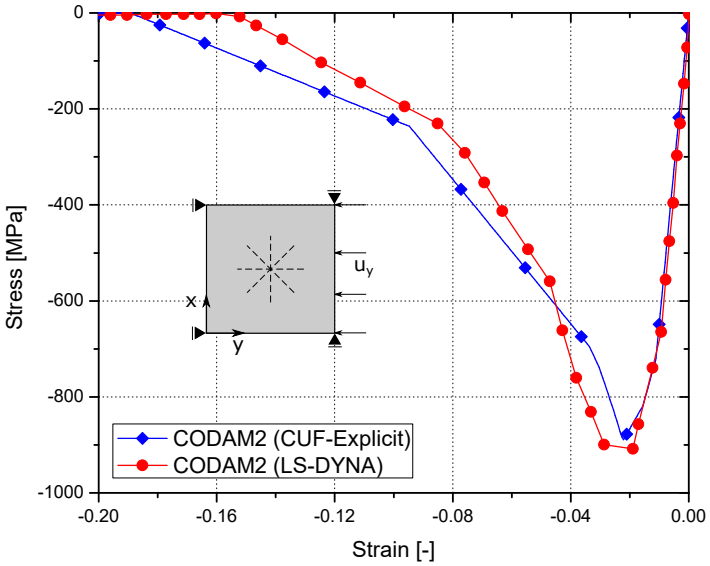

Fig. 5.13 Predicted response of the single-element $[90/45/0/-45]_{2s}$ quasi-isotropic laminate under uni-axial compressive strain.

5.3.2 Analysis of compact compression specimen

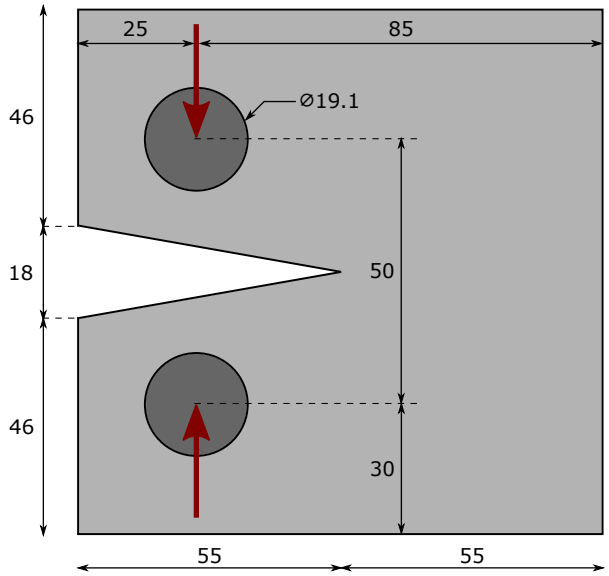

Fig. 5.14 Geometry and load conditions of the IM7/8552 CFRP $[90/45/0/-45]_{4s}$ quasi-isotropic compact compression test specimen.

The present numerical analysis is the compact compression (CC) test of a quasi-isotropic $[90/45/0/-45]_{4s}$ laminate, shown schematically in Fig. 5.14. This validation case is based on the works of Zobeiry et al. [162], which reports experimental data and reference numerical predictions. The CUF model is meshed with 191 quadratic (Q9) elements within the plane, and is obtained via a mesh convergence study. For compressive damage analysis, the post-peak fibre response is modelled using both linear and linear-brittle curves, to study their influence on progressive damage and failure. The first study considers a linear (LE1) thickness expansion for each ply, in combination with both linear and linear-brittle softening curves. The results of the analyses is presented in Fig. 5.16, in the form of force-displacement plots. Next, the influence of the polynomial order of the ply thickness functions is investigated. This study compares linear softening curves with the linear-brittle Br-30 option, the latter being selected based on the results of the first study. The force-displacement response for this case is presented in Fig. 5.17. In both studies, reference experimental data and numerical solutions obtained from LS-DYNA, are also plotted for comparison. The most significant observations are listed below:

1. The response predicted by the CUF models has a positive correlation with experimental data, as seen in Fig. 5.16 and Fig. 5.17.

2. Linear softening curves do not account for fibre micro-buckling and kinking, and thus over-predict the peak global loads, as seen in Fig. 5.16. Linear-brittle curves take such

phenomena into account, resulting in more accurate predictions of the peak load and post-peak softening, specifically for the case of the Br-30 model.

3. A difference in the slope is observed between the experimental and numerical approaches, in the linear part of the force-displacement curve. This likely stems from issues in perfectly replicating the experimental boundary conditions.

4. A considerable amount of noise is observed in the force-displacement response, and is likely due to the inherent issues related to compressive damage modelling. The use of linear-brittle softening models, which include a sudden loss of stiffness immediately after the peak stress level, may also contribute to a noisy response.

5. Since the current structure is loaded in compression within the plane, linear (LE1) ply thickness expansions are sufficient to obtain results of a required accuracy. This is not the case, however, when out-of-plane effects are prominent. For instance, impact loads lead to significant delamination and laminate bending, and necessitate higher-order expansions, based on the findings reported in [93].

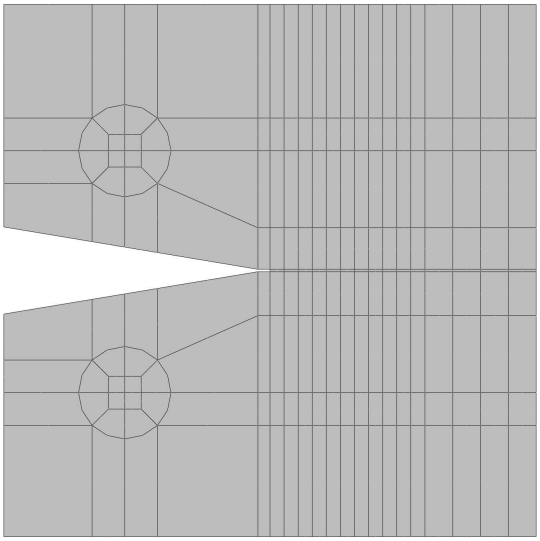

Fig. 5.15 In-plane discretisation of the compact compression specimen using 191 Q9 elements.

5.3.3 Failure strength of notched laminates in compression

The last validation case concerns the prediction of compressive strength in notched laminates. Two types of notches - open-hole and central sharp notch - are considered in the present work. The first study is the analysis of open-hole compression specimens of various scales, and is

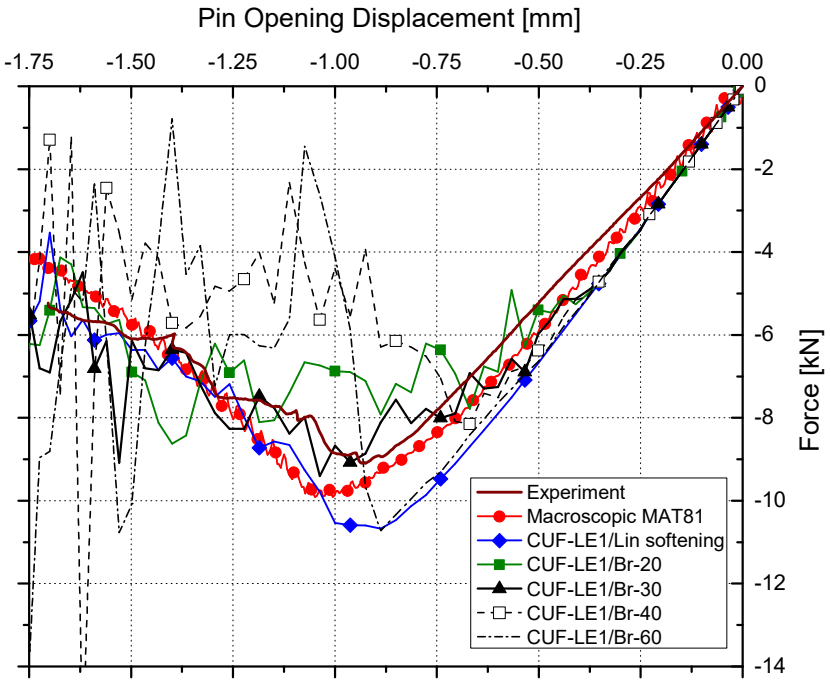

Fig. 5.16 Force-displacement response of the IM7/8552 CFRP dispersed-ply $[90/45/0/-45]_{4s}$ quasi-isotropic compact compression test specimen analysed using various fibre softening options (LE1 used in each case).

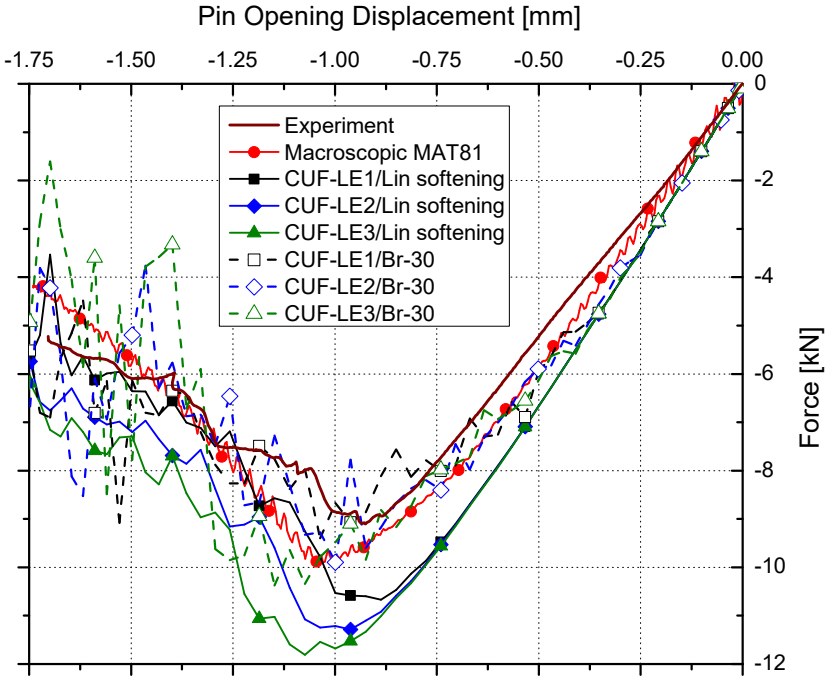

Fig. 5.17 Force-displacement response of the IM7/8552 CFRP dispersed-ply $[90/45/0/-45]_{4s}$ quasi-isotropic compact compression test specimen with increasing order of the ply thickness expansion function.

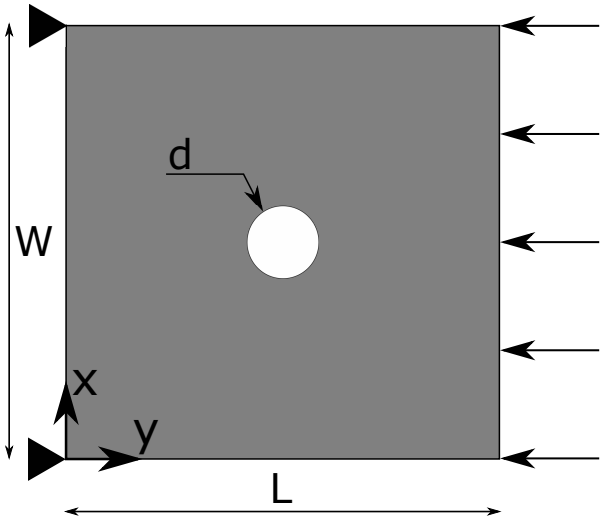

Fig. 5.18 Open-hole compression test of $[45/90/-45/0]_{4s}$ IM7/8552 CFRP laminate.

based on the experimental works of Lee and Soutis [82]. A schematic representation of the open-hole laminate is shown in Fig. 5.18, and Table 5.4 lists the various laminate scales considered in the current study. The composite laminate is quasi-isotropic in nature, with a $[45/90/-45/0]_{4s}$ stacking sequence, and has a total laminate thickness of 4 mm. A series of CUF models are developed, with progressive refinement of the in-plane and through-thickness mesh, and both linear and linear-brittle fibre softening curves are used. The first investigation considers the Scale-1 specimen, and the influence of the softening model on the peak compressive strength is studied. The Scale-1 laminate is modelled using 48 quadratic (Q9) elements, as shown in Fig. 5.21. The strength predictions reported by CUF models with a linear fibre softening curve are shown in Fig. 5.19. Similarly, the predicted strengths for the case of linear-brittle models are presented in Fig. 5.20. Next, the Scale-2 and Scale-3 laminates are analysed using a combination of the Br-30 linear-brittle model and linear (LE1) ply thickness expansions. The Scale-2 and Scale-3 models are meshed within the plane with 128 and 256 Q9 elements, respectively. Details of the numerical models, including discretisation and computational time, are provided in Table 5.5.

The second study is the compressive strength prediction of centre-notched laminates, following the works of Xu et al. [153]. The laminate characteristics of the open-hole case is retained, leading to a $[45/90/-45/0]_{4s}$ quasi-isotropic laminate with a 4 mm thickness. The Scale-8 (see Ref. [153] is analysed in the current study, and the CUF models consider the gauge section of the compression specimen, as seen in Fig. 5.23. The CUF models use the Br-30 softening curve, and each ply is modelled with a single linear (LE1) expansion, through its thickness. A mesh convergence study is performed to determine the in-plane mesh, and the results are presented in the form of force-displacement plots in Fig. 5.24, along with the

experimental curve for comparison. The saturated longitudinal (fibre) damage in the 0° ply and the transverse (matrix) damage in the 90° ply is shown in the form of contour plots in Fig. 5.25, as predicted by the CUF 108 Q9 model. The following points are noted:

1. Linear post-peak fibre softening models over-predict the compressive strength of open-hole laminates by about 60%, as seen in Fig. 5.19, and the error remains constant with further refinement of the structural mesh, i.e. the error remains even for a converged solution.

2. CUF models using the Br-30 linear-brittle curve predict compressive strengths which are in excellent agreement with experimental observations, as seen in Fig. 5.20.

3. The numerical analysis of the three scales of the open-hole laminate results in compressive strength predictions that correlate very well with experimental data, as seen in Fig. 5.22. Additionally, the CUF models are able to capture the experimentally observed size-effect, wherein the laminate strength is reduced as the scale is increased.

4. The Br-30 softening curve remains suitable for the numerical analysis of the centre-notched compression specimen, see Fig. 5.24, where the force-displacement curve of the 108 Q9 model is in good agreement with experimental data. The fracture morphology predicted by the CUF model, shown in Fig. 5.25, is also well represented compared to experiments, see Fig. 3b of Ref. [153].

Table 5.4 Dimensions of the three scales considered for the open-hole compression tests.

Scale	Gauge length L [mm]	Gauge width W [mm]	Diameter d [mm]
Scale - 1	32	32	6.35
Scale - 2	64	64	12.70
Scale - 3	128	128	25.40

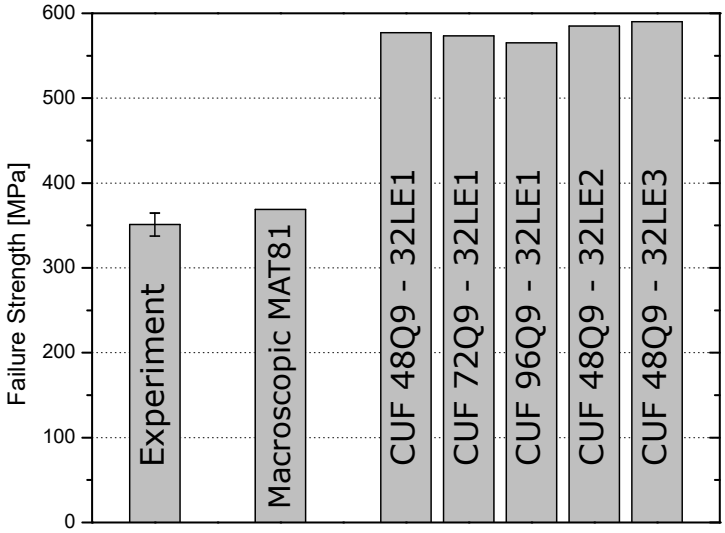

Fig. 5.19 Predicted failure strength of the $[45/90/-45/0]_{4s}$ quasi-isotropic open-hole compression specimen based on various CUF models with linear post-peak softening (scale-1 test). Experimental results are from [82].

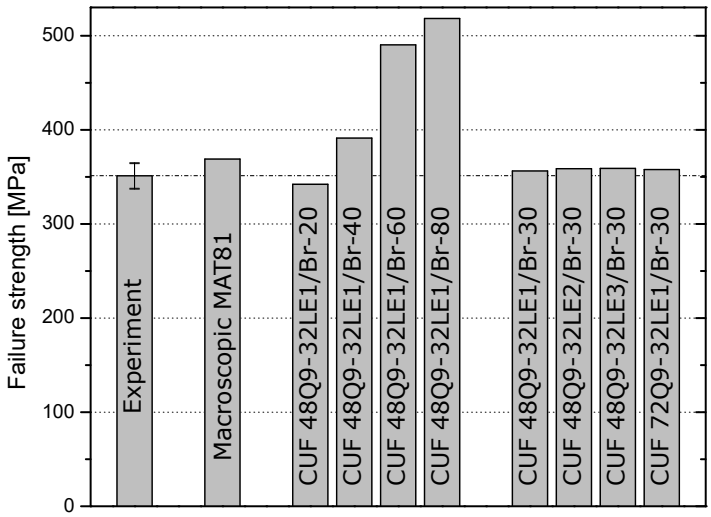

Fig. 5.20 Predicted failure strength of the $[45/90/-45/0]_{4s}$ quasi-isotropic open-hole compression specimen based on various CUF models with linear-brittle post-peak softening (scale-1 test). Experimental results are from [82].

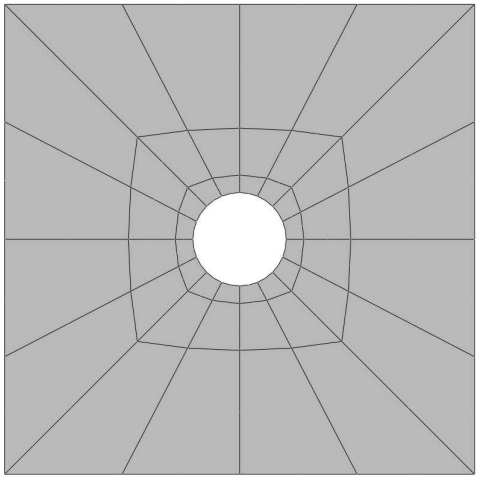

Fig. 5.21 In-plane discretization of the scale-1 open-hole compression specimen using 48 Q9 elements.

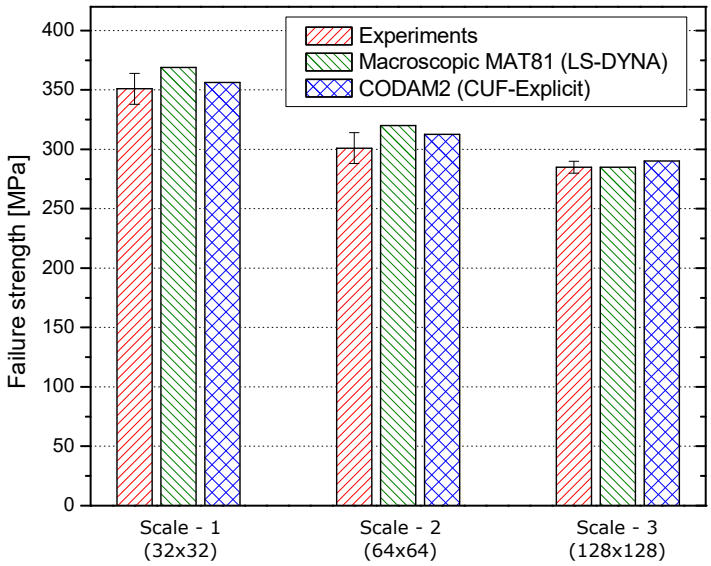

Fig. 5.22 Predicted failure strengths of the the $[45/90/-45/0]_{4s}$ quasi-isotropic open-hole compression specimen for all the scales by CUF models with linear brittle (Br-30) post-peak softening. Experimental results from [82].

Table 5.5 Model details for the compressive damage analysis of quasi-isotropic open-hole laminates.

Model	Discretisation of the open-hole specimen	DOF	Analysis Time* [hh:mm:ss]
	Scale-1 test (32 mm x 32 mm)		
CUF 48Q9 - 32LE1	48 Q9 elements (1 LE1 per layer)	22,176	00:29:34
CUF 48Q9 - 32LE2	48 Q9 elements (1 LE2 per layer)	43,680	01:20:23
CUF 48Q9 - 32LE3	48 Q9 elements (1 LE3 per layer)	65,184	02:51:20
CUF 72Q9 - 32LE1	72 Q9 elements (1 LE1 per layer)	33,264	00:46:51
	Scale-2 test (64 mm x 64 mm)		
CUF 128Q9 - 32LE1	128 Q9 elements (1 LE1 per layer)	57,024	01:49:03
	Scale-3 test (128 mm x 128 mm)		
CUF 256Q9 - 32LE1	256 Q9 elements (1 LE1 per layer)	114,048	03:09:29

* Computational times based on analyses performed on desktop PC using 6 cores.

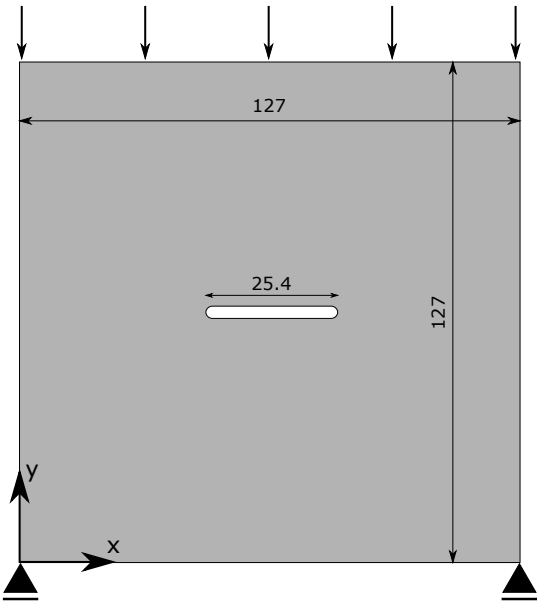

Fig. 5.23 Schematic representation of the $[45/90/-45/0]_{4s}$ quasi-isotropic centre-notched compression specimen.

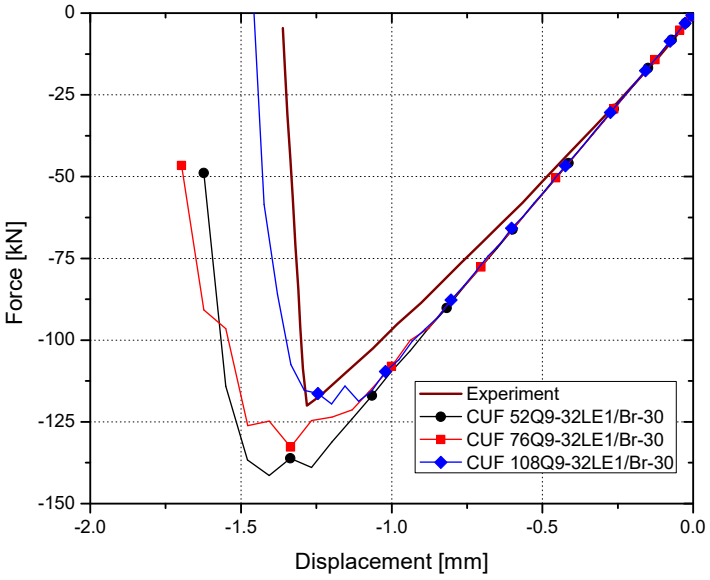

Fig. 5.24 Force-displacement response of the $[45/90/-45/0]_{4s}$ quasi-isotropic centre-notched compression specimen. Experimental results from [153].

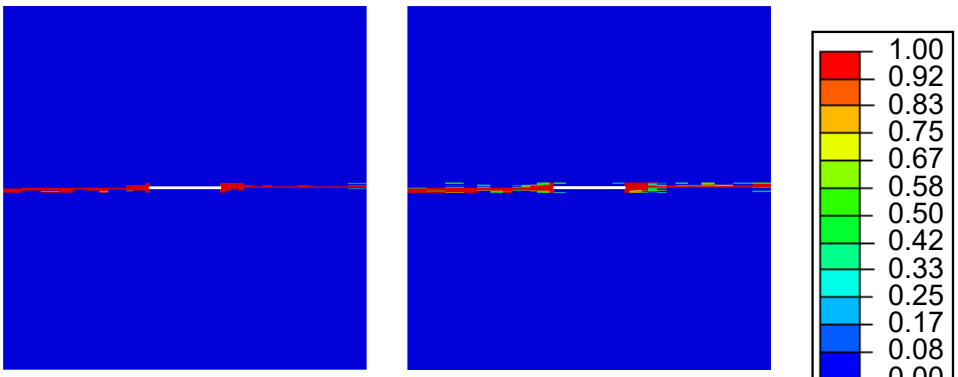

(a) Fibre damage in 0° ply (b) Matrix damage in 90° ply

Fig. 5.25 Saturated damage state in the $[45/90/-45/0]_{4s}$ quasi-isotropic centre-notched compression specimen predicted by the 108 Q9 - 32 LE1 CUF model. (a) Longitudinal damage in the 0° ply, and (b) transverse damage in the 90° ply.

5.4 Discussion

This chapter presents an overview of progressive damage analysis in CUF using the continuum damage mechanics-based CODAM2 material model. A detailed description of the formulation is provided, and a series of numerical assessments are carried out for the evaluation of progressive damage of IM7/8552 composite laminates subjected to tension and compression. Initial verification assessments for each load type consist of single-element studies, where a unidirectional lamina is loaded along, and perpendicular to, the fibre direction, leading to fibre-dominated and matrix-dominated damage modes, respectively. It is shown that the resulting stress-strain curves follow the bilinear path in accordance with the CODAM2 formulation, with the peak stress values corresponding to the input material strength values. In addition, the area under the stress-strain curve matches the material fracture energy, provided as an input to the analysis. Finally, a single-element laminate is considered, with a quasi-isotropic layup, and the CUF predictions are compared with reference numerical simulations obtained from LS-DYNA. A good correlation is observed in the predicted stress-strain response of the two numerical approaches. The obtained results provide initial verification of the model implementation in the CUF-Explicit framework.

The first laminate-level assessments for tensile progressive damage analysis consists of a series of centre-notched specimens of varying dimensions. The CUF models are able to predict the tensile failure strength of the centre-notched coupons with good general accuracy, and in addition, predict the experimentally observed size-effect where tensile strength is inversely proportional to laminate size. It is shown that the relaxed aspect-ratio constraints of the CUF approach allows for the same discretisation to be scaled up along with the geometry, leading to a constant computational overhead for the analysis of centre-notched specimens of varying dimensions, which is not possible with classical FE-based approaches. The final assessment of tensile progressive damage is the simulation of the over-height compact tension test. A series of CUF models are developed with various through-thickness refinements. It is shown that the predicted force-displacement response has a good correlation with LS-DYNA predictions as well as experimental results. The numerical models, in general, over-predict the peak force when compared to experiments, and is attributed to the fact that they do not model delamination. The analysis of the over-height tension specimen results in considerable noise in the force-displacement response during the post-peak softening regime. This likely stems from the use of higher-order elements, and the use of numerical damping approaches such as the Bulk Viscosity Method (BVM) could be helpful in obtaining a smoother response.

For the case of compressive damage modelling, the limitations of bilinear damage models with linear fibre softening laws is emphasised. Phenomena such as fibre micro-buckling and the formation of kink-bands, under compressive loading of the laminate, have significant conse-

quences on global laminate behaviour, and simple damage models with linear fibre softening are not capable of accounting for such effects.The present work uses linear-brittle fibre softening curves, where a sudden drop in stress occurs once the peak strength is attained, followed by a stable stress plateau until final failure, as a reasonable approximation of experimentally observed behaviour of quasi-isotropic laminates. The first assessment of compressive damage is the compact compression test. The assessment studies the use of linear and linear-brittle softening options, and their effect on global laminate response. The basic damage model with a linear fibre softening law leads to significant errors in the peak force predictions. A series of linear-brittle curves are then used, with varying levels of residual stress, to calibrate the optimum curve for the current class of problems. The results indicate that the Br-30 model, i.e. the linear-brittle curve with a residual stress whose magnitude is 30% of the peak stress, leads to the most accurate response with under 10% error in peak force prediction compared to experiments, as well as a reasonably good evaluation of the post-peak softening behaviour. The use of linear-brittle models with higher values of residual stress leads to highly oscillatory response, and likely stems from the sudden loss of a large magnitude of material stiffness at the evaluated gauss point, giving rise to noise in the system.

The second set of assessments consider the open-hole compression test, and a series of such tests are performed for specimens of varying dimensions. As in the previous case, the use of linear softening models leads to significant errors in the predicted compressive failure strength. On the other hand, using linear-brittle damage evolution laws, specifically the Br-30 model, results in very accurate predictions which are in line with experiments. The final assessment is the compressive strength prediction of centre-notched compression specimens, and the Br-30 model provides excellent predictions which are in perfect agreement with experimental observations, in terms of laminate peak strength as well as damage morphology.

The presented validation cases therefore demonstrate the capabilities of the CUF-Explicit framework as a computationally efficient platform for the accurate progressive damage analysis of composite laminates loaded in tension and in compression. The outcomes of this chapter, in combination with CUF contact modelling capabilities highlighted in Chapter 4, allow for the modelling of progressive damage in fibre-reinforced composite laminates subjected to impact loads, and is presented in Chapter 6 of the present thesis.

Chapter 6

Low-velocity impact analysis

This chapter presents a series of numerical assessments as validation cases to demonstrate the capability of the CUF-Explicit framework for the impact analysis of composite laminates. The first assessment is the elastic impact analysis of a fibre-reinforced laminated plate. An elastoplastic multilayered metallic plate is then considered, and demonstrates the accuracy and computational efficiency of the proposed layer-wise CUF models, compared to 3D-FE approaches, for the analysis of nonlinear impact problems. The final assessment is the progressive damage analysis of a circular laminated composite plate subjected to impact loads, and the numerical example confirms the capability of the CUF virtual testing platform in handling problems of this class.[1]

6.1 Numerical assessments of low-velocity impact

6.1.1 Linear-elastic stress analysis of composite laminate

The primary objective of the present numerical assessment is to compare the proposed modelling approach using layer-wise structural models based on higher-order CUF theories, with standard techniques commonly found in the literature, i.e. 3D-FEA. The comparison involves determining the quality of the discretisation, and subsequently the analysis time, required by the two modelling strategies for solutions of comparable quality. For this purpose, a simple square composite plate of side length 100 mm has been considered, and is subjected to impact

[1] Parts of this chapter have been published in the following:

1. MH Nagaraj, M Petrolo, & E Carrera (2020). Progressive damage analysis of composite laminates subjected to low-velocity impact using 2D layer-wise structural models. International Journal of Non-Linear Mechanics, 127, 103591.

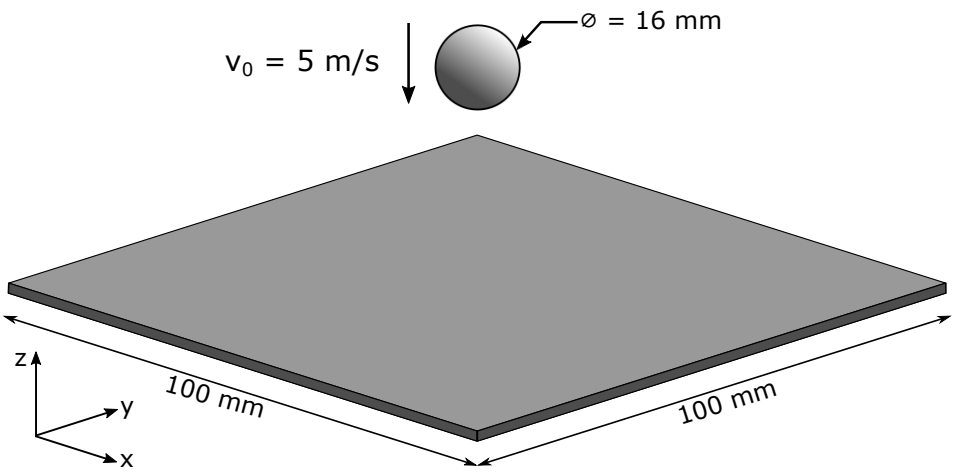

Fig. 6.1 Geometry of the square composite laminate under low-velocity impact.

at its centre via a 16 mm diameter spherical impactor with a prescribed velocity v_0 = 5 m/s, as shown in Fig. 6.1. The composite laminate is quasi-isotropic with a ply stacking sequence of $[90/45/0/-45]_{2s}$, and is clamped at all edges. The thickness of each ply is 0.125 mm, and the laminate thickness is 2 mm. The IM7/8552 CFRP composite system is considered, and its elastic properties are provided in Table 6.1. The current assessment only considers a linear-elastic stress analysis of the composite laminate subjected to impact, since the objective is to evaluate the performance of the two numerical modelling approaches.

The analysis is performed using a series of layer-wise 2D-CUF models and 3D-FE models developed in ABAQUS/Explicit. The 3D-FE models consider progressive mesh refinement in the thickness direction of each ply. Similarly, three CUF models are developed by increasing the polynomial order of the expansion function used to model the thickness of individual plies. The models are labelled as CUF-LEn, where n denotes the order of the Lagrange ply thickness expansion function. A fourth CUF model is also developed which uses 3 linear expansion functions (LE1) per ply of the laminate. This model is kinematically equivalent to the 3D-FE model (3 C3D8R/ply), in the thickness direction. Details of each model, including the discretisation and analysis time, have been listed in Table 6.2. The in-plane stress components σ_{xx} and σ_{xy}, at [x=48, y=48] and through the thickness, are plotted in Fig. 6.2. The interlaminar shear stress component σ_{yz}, at [x=40, y=40] and through the thickness, is shown in Fig. 6.3. The following observations are made

1. As expected, the in-plane stress fields predicted by all the numerical models perfectly match each other, as seen in Fig. 6.2. This is due to the low (in-plane) kinematic requirement of the structural models for the evaluation of in-plane fields.

2. The interlaminar stress fields, however, have a higher requirement for (through-thickness) kinematic refinement. This can be observed in Fig. 6.3 where a single brick element in the case of 3D-FE models, and a single linear expansion (LE1) for CUF models, leads to inaccurate results for the interlaminar shear stress σ_{yz}.

3. CUF models with higher-order thickness functions result in a converged solution of σ_{yz}. Similarly, the use of multiple solid elements though the thickness of each ply in 3D-FE models leads to interlaminar stresses which approach that predicted by the CUF models. Such a trend is consistent with the observations in [35].

4. The CUF-LE2 model is the coarsest mesh which leads to a converged value of σ_{yz}, while the ABQ-Refined model (5 elements/ply) predicts an interlaminar stress field of comparable quality. The CUF-LE2 model requires approximately 76x fewer degrees of freedom and 5x less analysis time compared to the refined 3D-FE model, demonstrating the computational efficiency of the proposed layer-wise modelling approach for impact analysis.

Table 6.1 Elastic properties of IM7/8552 CFRP.

E_1 [GPa]	E_2 [GPa]	E_3 [GPa]	G_{12} [GPa]	G_{13} [GPa]	G_{23} [GPa]	ν_{12}	ν_{13}	ν_{23}	ρ [kg/m^3]
165.00	9.00	9.00	5.60	5.60	2.80	0.34	0.34	0.50	1700.00

Table 6.2 Model details for the elastic impact analysis of the quasi-isotropic composite laminate.

Model	Laminate Discretisation	DOF	Analysis Time* [hh:mm:ss]
ABQ - Coarse	102,400 C3D8R elements (1 elem/layer)	334,611	0:09:04
ABQ - Medium	307,200 C3D8R elements (3 elem/layer)	964,467	1:15:06
ABQ - Refined	512,000 C3D8R elements (5 elem/layer)	1,594,323	3:16:33
CUF - LE1	48 Q9 elements (1 LE1/layer)	10,659	0:10:29
CUF - LE2	48 Q9 elements (1 LE2/layer)	20,691	0:37:55
CUF - LE3	48 Q9 elements (1 LE3/layer)	30,723	1:30:46
CUF - 3LE1	48 Q9 elements (3 LE1/layer)	30,723	1:38:53

* Reported computational times based on analyses performed on desktop PC using 1 core.

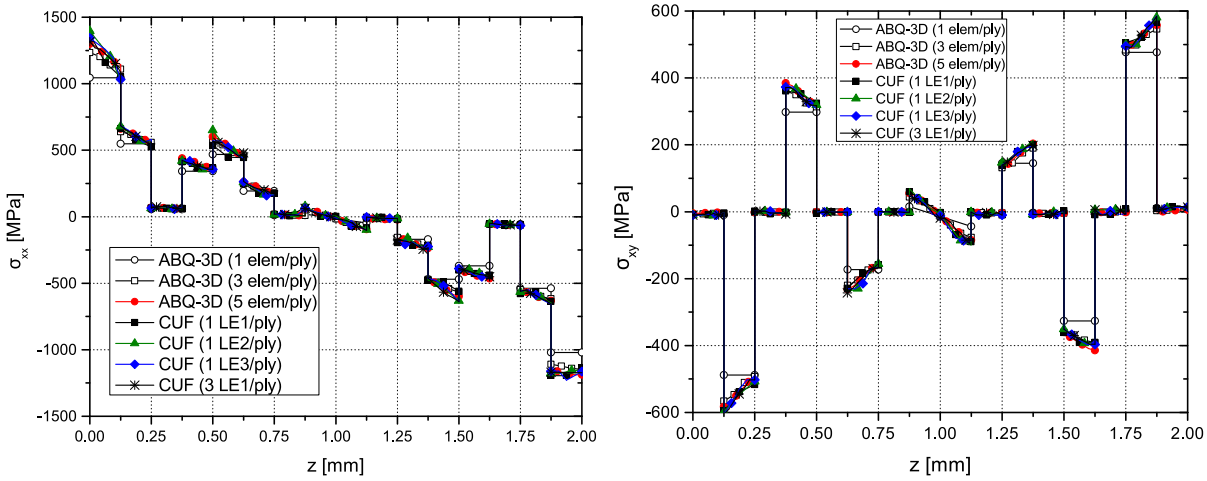

(a) σ_{xx} (b) σ_{xy}

Fig. 6.2 In-plane stress fields along the z-axis of the composite plate.

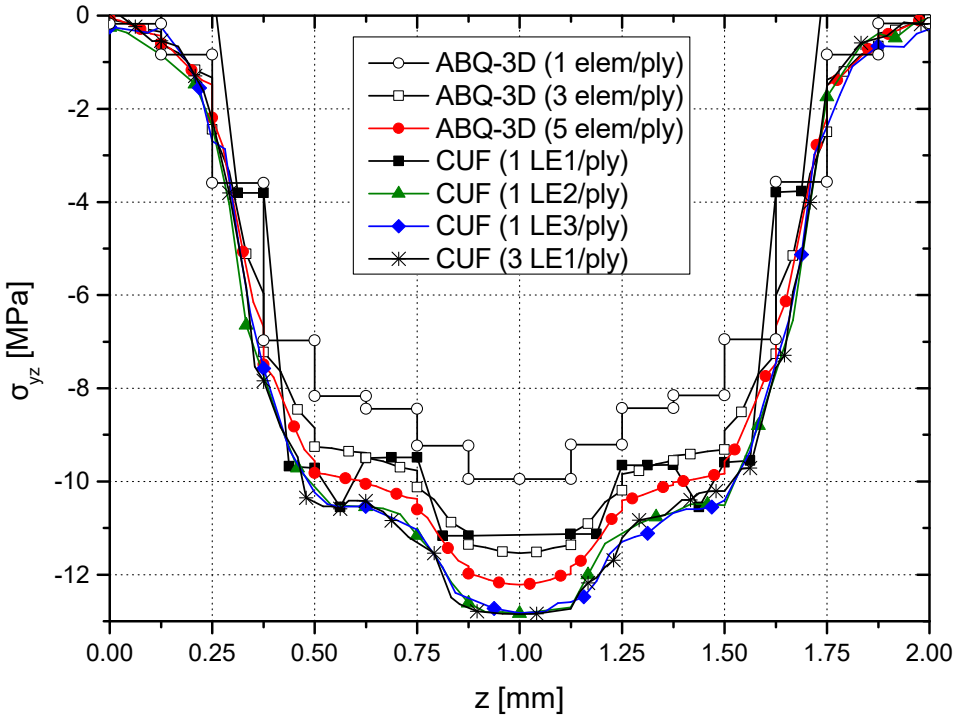

Fig. 6.3 Interlaminar shear stress component σ_{yz} along the z-axis of the square composite plate.

6.1.2 Nonlinear analysis of multilayered metallic plate

The current numerical example compares the relative performance of layer-wise 2D-CUF and 3D-FE models, when material nonlinearity is present in the impact analysis. The same laminated plate as in the previous numerical assessment, see Fig. 6.1, is analysed in the present case, but is now modelled as a 16-layer bimetallic laminated plate. The two metallic constituents M1 and M2 are assumed to be elastoplastic, and their material properties are given in Table 6.3. Both materials are modelled as elastic - perfectly plastic. The bimetallic laminate has a $[M1/M2]_s$ layup, and is 2 mm thick. Physical nonlinearity within the system stems from the elastoplastic behaviour of the metallic constituents, and has been considered in the present analysis since it is available in both CUF and 3D-FE numerical platforms, thereby ensuring consistency of the type and complexity of the nonlinear material behaviour, while comparing the two modelling approaches.

The bimetallic plate under impact is analysed using 2D-CUF theories, while reference numerical results are obtained from 3D-FE models developed using ABAQUS/Explicit. Details of the model discretisation and total analysis time is listed in Table 6.4. The deformation of the impacted surface of the bimetallic plate along the y-axis, in the form of the vertical deflection u_z and equivalent plastic strains, is presented in Fig. 6.4. The morphology of the plastic deformation at the impact zone, in the form of 3D plastic strain contours, is given in Fig. 6.5. The following comments are made

1. The deformation of the bimetallic plate under impact predicted by the CUF-LW model matches that of the refined 3D-FE analysis, as seen in Fig. 6.4. This verifies the CUF framework for impact cases with nonlinear material behaviour.

2. Insufficient mesh refinement in 3D-FE models leads to significant errors in the prediction of the extent and morphology of the plastic zone, as seen in Fig .6.4b and Fig. 6.5.

3. The refined 3D-FE model is about 80x larger in terms of computational size and requires approximately 3.6x more time to solve, compared to the layer-wise 2D-CUF approach, for similar quality of solutions. This demonstrates that the computational efficiency observed in the previous elastic impact case carries over also for nonlinear impact analysis.

Table 6.3 Elastoplastic constituent properties of the multilayered metallic plate.

Constituent	Young's Modulus E [GPa]	Poisson's ratio ν [-]	Yield stress σ_y [MPa]
Material-1 (M1)	210	0.30	210
Material-2 (M2)	70	0.30	110

Table 6.4 Model details for the impact analysis of the $[M1/M2]_{4s}$ elastoplastic multilayered plate.

Model	Plate Discretisation	DOF	Analysis Time* [hh:mm:ss]
ABQ - Coarse	102,400 C3D8R elements (1 elem/layer)	334,611	00:24:18
ABQ - Refined	270,848 C3D8R elements (2 elem/layer)	856,251	01:55:12
CUF-LW	48 Q9 elements (1 LE1/layer)	10,659	0:31:29

* Reported computational times based on analyses performed on desktop PC using 1 core.

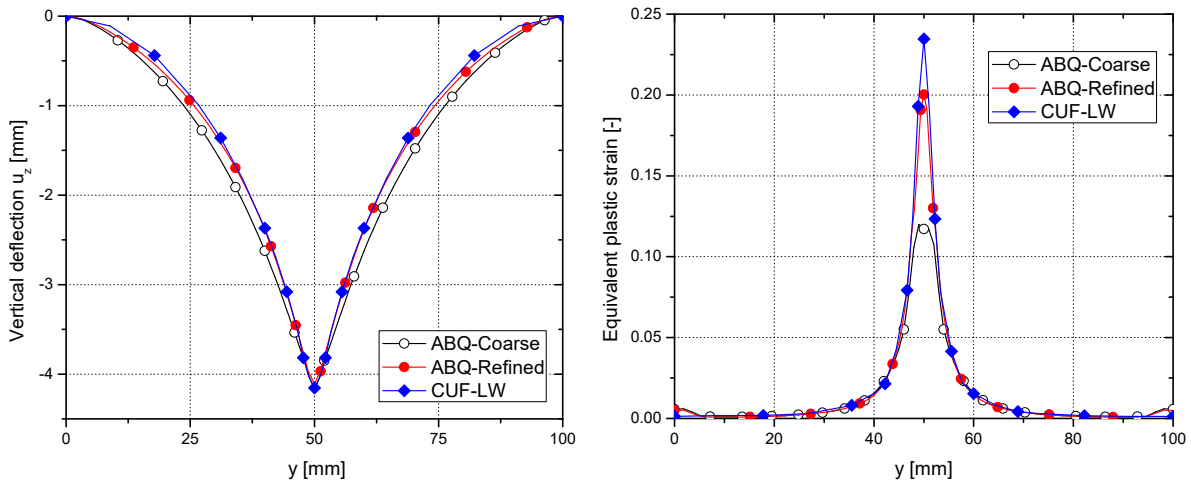

(a) u_z (b) Equivalent plastic strains

Fig. 6.4 Vertical deflection u_z and plastic strain of the elastoplastic plate along the y-axis.

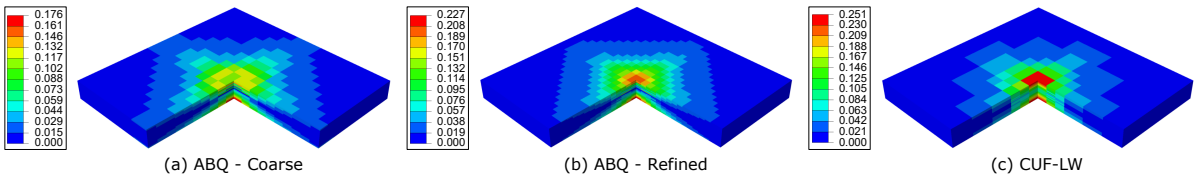

Fig. 6.5 Contour plot of the plastic strain field in the impact region of the elastoplastic plate.

6.1.3 Progressive damage analysis of a circular composite plate

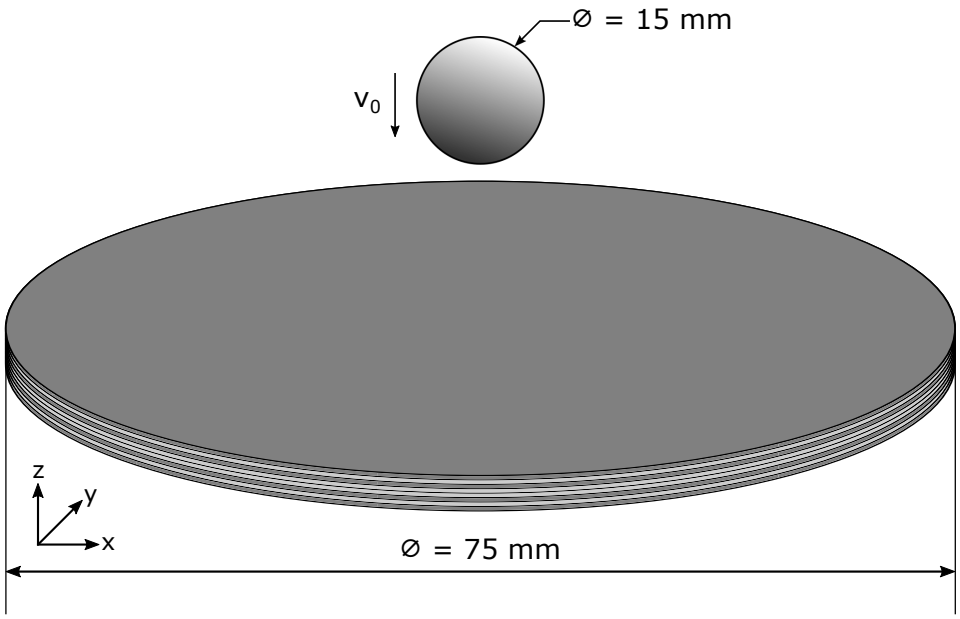

Fig. 6.6 Geometry of the circular CFRP composite laminate under low-velocity impact.

This numerical example deals with the progressive damage analysis of a composite laminated plate subjected to low-velocity impact. The composite laminate is a 75 mm diameter disk, fully clamped at its edges, and impacted at its centre by a 15 mm diameter spherical impactor with a prescribed velocity of 3.83 m/s and a kinetic energy of 7.35 J, as shown in Fig. 6.6. The current assessment is derived from the works of Shi et al. [127]. The composite laminate is constructed from HTS40/9772 CFRP, whose elastic and strength properties are listed in Table 6.5. The composite laminate has a $[0/90]_{2s}$ layup, with 0.25 mm thick plies, leading to a 2 mm laminate.

The problem is analysed by developing a series of layer-wise CUF models by successively refining the in-plane discretisation, as well as the polynomial order of the Lagrange expansion function defined over the ply thickness. Delamination is taken into account by the insertion of a cohesive layer between successive plies, where the cohesive elements are based on the mixed-mode cohesive constitutive model developed by Camanho et al. [14]. A detailed overview of cohesive modelling in CUF is provided in [69]. The material parameters of the cohesive layer, obtained from [127], are given in Table 6.6. The first assessment is based on the progressive refinement of the in-plane discretisation, to study its influence on th quality of the solution. In this case, each ply is modelled using a quadratic (LE2) thickness function. The impact force-time plots obtained from this assessment are presented in Fig. 6.7. The 192 Q9 in-plane mesh, see Fig. 6.8, is selected for further studies based on the obtained mesh convergence

analysis results. The second set of assessments investigates the effect of the thickness function polynomial order on the quality of the numerical results. In this case, the in-plane mesh is held constant at 192 Q9, and a series of models are developed with increasingly refined ply thickness expansion functions (LE1, LE2 and LE3). The predicted force-time curves obtained in this study are reported in Fig. 6.9. In both cases, reference numerical and experimental curves, obtained from [127], have been overlaid for comparison. The damaged state in the impact zone, predicted by the CUF 192 Q9 - LE3 model, is shown in Fig. 6.10 in the form of 3D distributions of the damage variables, while the extent of delamination is shown in Fig. 6.11. The following observations are made

1. The use of linear expansion functions (LE1), leads to severe oscillations, as seen in Fig. 6.9. Higher-order expansion functions lead to stable and smooth impact force-time curve which correlate well with the reference experimental and numerical curves, thus validating layer-wise CUF models for the progressive damage analysis of fibre-reinforced composites under impact loads.

2. The differences between the CUF models and experiments, in the post-impact unloading regime of the impact force time histories, stems from the fact that energy dissipation mechanisms such as contact friction and permanent indentation of the laminate have not been considered in the present analysis. However, a good general agreement of the global response is demonstrated between the experimental data and the solutions reported by the CUF models, as well as the accurate prediction of the peak load.

3. The layer-wise modelling technique adopted by the proposed approach leads to the evaluation of the damage state within each ply, as well as delamination growth between consecutive plies. As seen from Fig. 6.10, matrix damage is the dominant failure mechanism.

Table 6.5 Elastic and strength properties of HTS40/9772 CFRP [127].

E_1 [GPa]	E_2 [GPa]	E_3 [GPa]	G_{12} [GPa]	G_{13} [GPa]	G_{23} [GPa]	ν_{12}	ν_{13}	ν_{23}	Density $[kg/m^3]$
153.0	10.3	10.3	6.0	6.0	3.7	0.3	0.3	0.4	1600.0
X_T [MPa]	X_C [MPa]	Y_T [MPa]	Y_C [MPa]	S_{12} [MPa]	S_{23} [MPa]	G_1^T $[kJ/m^2]$	G_2^T $[kJ/m^2]$	G_1^C $[kJ/m^2]$	G_2^C $[kJ/m^2]$
2537.0	1580.0	82.0	236.0	90.0	40.0	91.6	0.22	79.9	1.1

Table 6.6 Interface properties [127].

Parameter	Mode I	Mode II	Mode III
Elastic modulus [GPa/mm]	1373.3	493.3	493.3
Interlaminar strength [MPa]	62.3	92.3	92.3
Interlaminar fracture toughness $[kJ/m^2]$	0.28	0.79	0.79

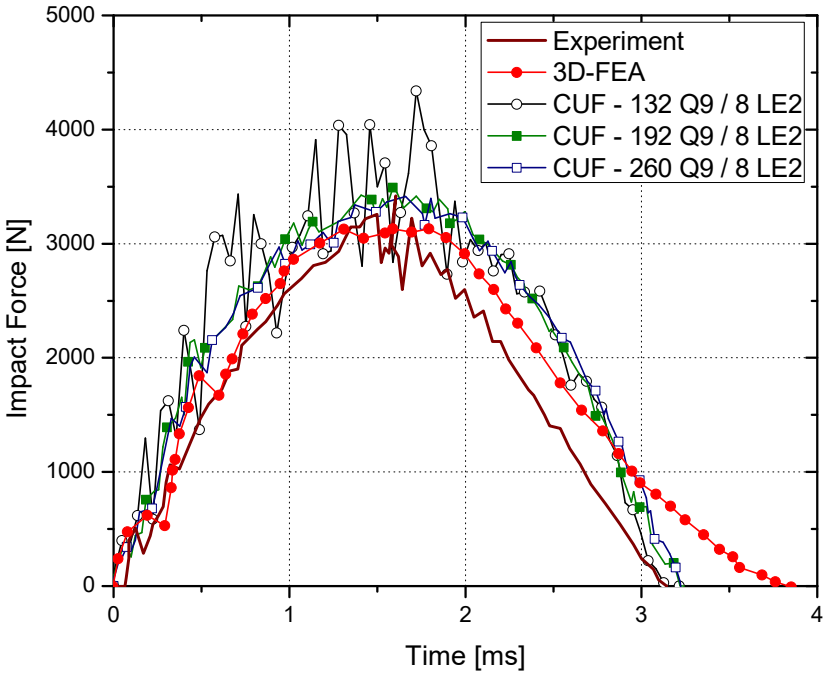

Fig. 6.7 Impact force-time response based on the in-plane discretisation convergence analysis of the $[0/90]_{2s}$ composite laminate. Experimental data and numerical predictions obtained from [127].

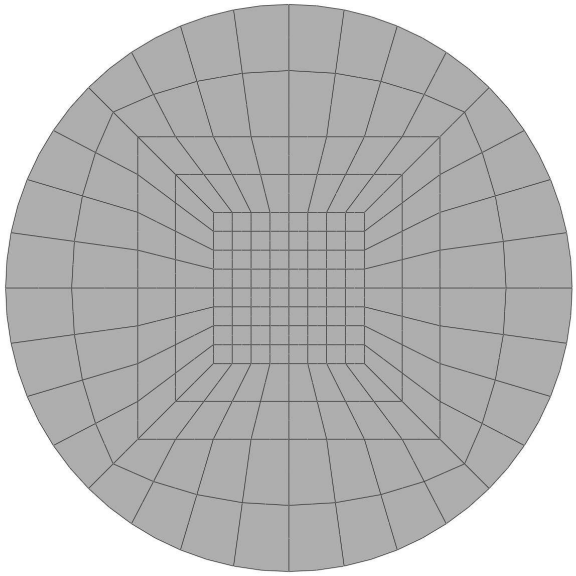

Fig. 6.8 The 192 Q9 mesh used for the in-plane discretisation of the circular composite laminate.

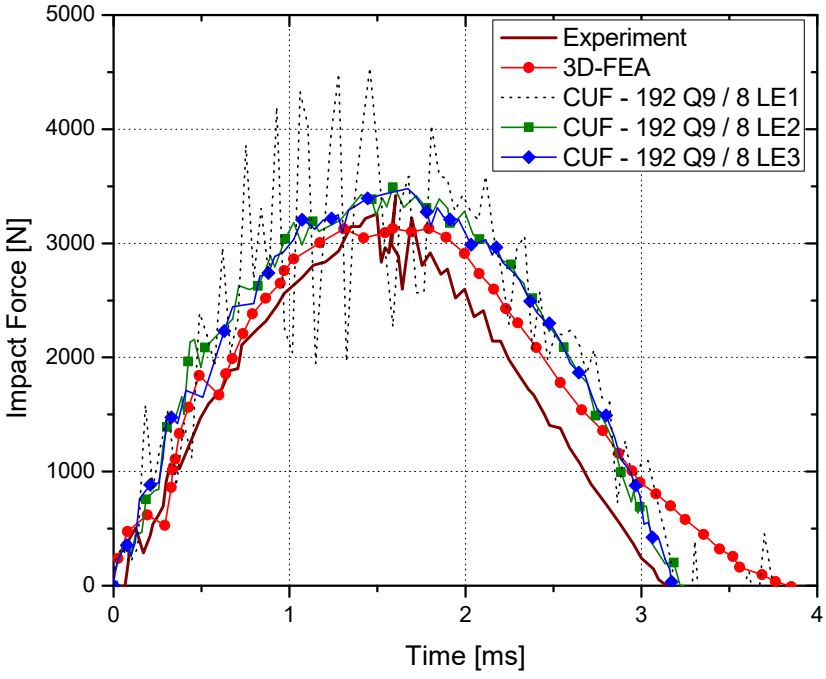

Fig. 6.9 Impact force-time response obtained from the thickness expansion function convergence study of the $[0/90]_{2s}$ composite laminate. Reference experimental and numerical results obtained from [127].

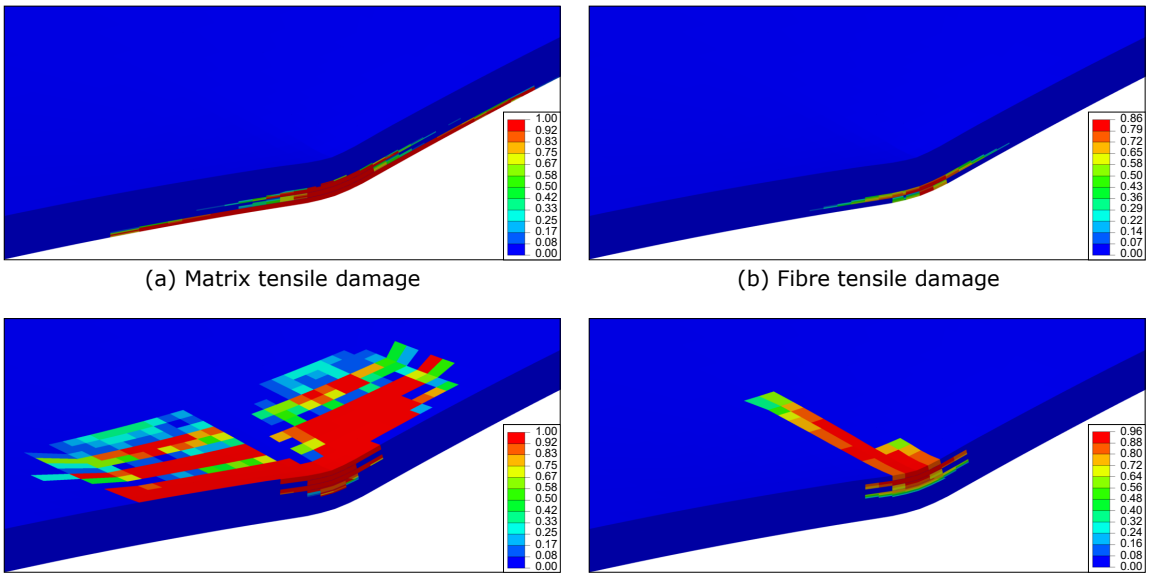

(a) Matrix tensile damage

(b) Fibre tensile damage

(c) Matrix compressive damage

(d) Fibre compressive damage

Fig. 6.10 Damaged state predicted by the CUF 192 Q9 - LE3 model at the impact site of the composite laminate.

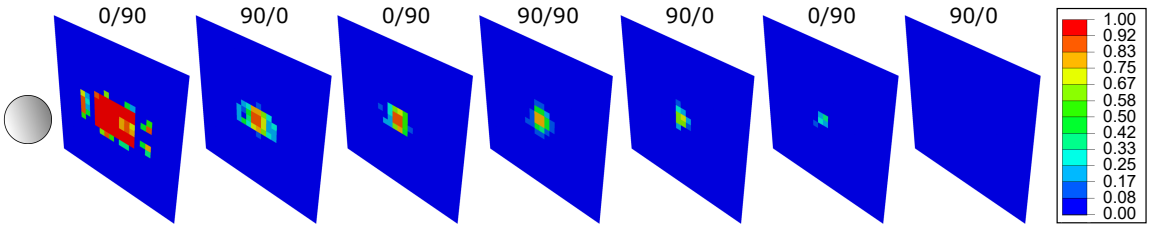

Fig. 6.11 Predicted delamination at the impact site of the circular composite laminate (CUF 192 Q9 - LE3 model).

6.2 Discussion

This chapter presents a series of numerical assessments involving low-velocity impact of multilayered laminated plates to demonstrate the capabilities of layer-wise 2D-CUF models, and their advantages over standard 3D-FE approaches.

The first assessment considers the linear-elastic stress analysis of a quasi-isotropic IM7/8552 composite laminate clamped at its edges and impacted at its centre by a spherical impactor. The motivation of this assessment is to compare 2D-CUF and 3D-FE models in the evaluation of the 3D stress field, with a focus on interlaminar terms, since they constitute an important input to composite damage models. An inaccurate evaluation of the stress and strain tensors, even within the elastic regime, leads to errors during the damage initiation phase and could result in significant inaccuracies during damage progression and eventual failure. A mesh convergence analysis is performed for both approaches, considering a refinement of the laminate thickness. In the 3D-FE models, each ply is modelled with an increasing number of solid hexahedral elements, while in the case of 2D-CUF models, thickness expansion functions of increasing polynomial order are used to model individual plies. As expected, all the numerical models predict the same intralaminar stress fields, irrespective of the level of through-thickness refinement. However, a significant difference is observed when interlaminar stress fields are considered. For the case of 2D-CUF, all the models, except the one with linear (LE1) ply thickness expansion, converge to the same value of interlaminar shear stress through the thickness of the laminate. On the other hand, as the through-thickness discretisation is refined for 3D-FE models, the predicted interlaminar shear stress approaches that of the converged CUF results. The most refined 3D-FE model, with 5 solid elements per ply of the laminate, predicts stress values which are in close agreement with the CUF predictions. The high through-thickness discretisation requirements of the 3D-FE models leads to escalating computational costs of the analysis, with the coarsest converged CUF model (considering LE2 expansions) requiring approximately $76x$ fewer degrees of freedom and about $5x$ less analysis time, compared to the refined 3D-FE model. This assessment demonstrates the accuracy and computational efficiency of the proposed layer-wise CUF approach.

The second numerical assessment considers a bimetallic multilayered laminate subjected to low-velocity impact at its centre. The laminated plate is composed of two elastoplastic materials, and the aim of this assessment is to evaluate the computational performance of the layer-wise CUF approach, compared to standard 3D-FE, for impact problems involving material nonlinearity. Two 3D-FE models are developed, with 1 and 2 solid hexahedral elements used to model the thickness of each layer, respectively. The 2D-CUF model considers one LE1 thickness expansion to model an individual layer. It is seen that the results obtained by the CUF analysis are in excellent correlation with refined 3D-FE results, in terms of global laminate

deformation as well as evaluation of localised plastic regions. The refined 3D-FE model is about $80x$ larger in computational size, and requires approximately $3.6x$ more time to obtain solutions of comparable accuracy, indicating that the computational efficiency of layer-wise CUF models for impact problems, observed in the previous linear-elastic stress analysis, is maintained even in the presence of physical nonlinearities.

The final numerical assessment is the progressive damage analysis of a CFRP composite laminated plate under low-velocity impact loads. A circular laminate is clamped at its edges and a spherical impactor with an initial prescribed velocity impacts the laminate at its centre. A series of CUF models is developed, with increasing refinement of both the in-plane geometry as well as the laminate thickness. The first study evaluates the effect of the in-plane mesh on the accuracy of the solution, keeping the thickness function constant (LE2), and the in-plane discretisation is decided on the basis of this convergence analysis. Next, the influence of the polynomial order of the ply thickness expansion function is studied. It is observed that linear (LE1) expansions lead to oscillatory results, while higher-order functions lead to a stable and accurate response. This trend is attributed to the fact that interlaminar stress fields are important drivers of material nonlinearity in the current example, specifically in the evaluation of delamination initiation and propagation. The layer-wise CUF models, with at minimum a quadratic (LE2) expansion function to model individual plies, predict impact force-time responses that correlate well with experimental results as well as numerical simulations. The predicted peak force is in line with experimental observations, however, a slight deviation is observed in the post-impact unloading phase of the analysis. This likely stems from the fact that the developed 2D-CUF models do not account for friction or plastic deformation of the laminate, which leads to the formation of a permanent indentation. Such phenomena are energy dissipation mechanisms which account for the difference between the predicted and experimental unloading curves. In addition, the damage morphology predicted by the CUF models is in good general agreement with experiments, in terms of the extent of delamination and intralaminar damage. The simulations indicate that progressive damage is matrix-dominated, in both tension and compression, with a small amount of saturated fibre damage.

The results presented in the current chapter demonstrate the capability of layer-wise CUF models in analysing impact problems in an accurate and computationally efficient manner, compared to standard 3D-FE approaches. Furthermore the capabilities of the CUF-Explicit platform in the progressive damage modelling and analysis of fibre-reinforced laminated composites subjected to low-velocity impact loads is also demonstrated.

Chapter 7

Conclusions and Perspectives

Summary and conclusions of the current work

The primary aim of the present thesis was the development of a computationally efficient numerical platform, using higher-order structural theories derived from the Carrera Unified Formulation, for the progressive damage analysis of fibre-reinforced composite laminates subjected to low-velocity impact loads. 1D- and 2D-CUF theories have been demonstrated to provide accurate 3D descriptions of the stress and strain fields, leading to solutions comparable to 3D-FEA in accuracy, without the corresponding computational overheads. The focus of the present work is to evaluate the capabilities and performance of CUF models when applied to impact problems, and consequently to demonstrate their computational efficiency for the analysis of this class of nonlinear structural problems.

Chapter 2 introduced the concept of the Carrera Unified Formulation, and provided a detailed description of the formulation and finite element implementation of refined 1D models based on higher-order structural theories generated using CUF. The concept of the fundamental nucleus was discussed, and its role in the development of higher-order theories in a generalised manner was highlighted. A brief overview of the Taylor and Lagrange expansion classes was provided. A numerical example was presented to motivate the advantages of using higher-order numerical models for the high-fidelity analysis of multi-layered structures such as fibre-reinforced laminated composites. It was shown that the use of 1D-CUF models enabled over a ten-fold reduction in computational size and time of the problem, compared to standard 3D-FE approaches. Such savings motivate the development of CUF models to more complex nonlinear analysis, such as progressive damage and low-velocity impact analysis. The last part of the chapter provided an overview of the techniques employed in the current work for the solution to nonlinear problems. The formulation and implementation of the Newton-Raphson scheme was described in detail, and was employed for the implicit analysis of a variety of

nonlinear problems, such as material plasticity and quasi-static contact. A numerical platform using a combination of higher-order CUF theories and an explicit time integration scheme – CUF-Explicit – was also described in detail, and was used for progressive damage analysis and dynamic contact/impact problems, and finally low-velocity impact analysis of composite structures.

Chapter 3 described a two-step sequential global-local technique, whereby the academic MUL^2 code was interfaced with the commercial FE solver ABAQUS. The process involved an initial low-fidelity analysis in ABAQUS of the global structure, followed by a high-fidelity local CUF analysis of the critical regions of interest. The global displacements were then prescribed on the boundary of the local domain to drive the high-fidelity analysis. A series of numerical assessments were presented to demonstrate the capabilities of the proposed global-local approach. In particular, it was shown that the application of such an approach to the stress analysis of composite structures leads to significant savings in computational effort, on the order of one magnitude, compared to single-step CUF models of comparable accuracy. The technique was also demonstrated to be effective for the case of physically nonlinear analysis. The promising results indicate the suitability of the 2-step global-local approach towards the efficient high-fidelity nonlinear analysis of complex composite structures.

Chapter 4 introduced the topic of computational contact modelling, and described in detail its implementation in the CUF framework. In particular, node-to-node and node-surface contact discretisation schemes were discussed, in combination with the penalty and Lagrange multiplier approaches to contact constraint enforcement. A series of numerical cases were presented for the case of static contact, which were solved implicitly using the Newton-Raphson method. The presented numerical examples demonstrated the capabilities of the framework in handling multiple contact pairs with an arbitrary number of bodies as well as the presence of multiple sources of nonlinearities, namely elastoplasticity. The global-local technique was further applied to an assessment involving elastoplastic contact, and a improvement in computational efficiency was demonstrated compared to 3D-FE approaches. On average, 1D-CUF models required approximately two orders of magnitude fewer degrees of freedom and one order of magnitude less analysis time, when compared to 3D-FE approaches. In the final part of the chapter, an assessment involving dynamic contact/impact of two identical elastic bars was presented, which was solved explicitly using the CUF-Explicit solver. The presented numerical assessment constituted an initial verification of the CUF framework in handling such a class of problems.

Chapter 5 focused on the development of progressive damage modelling capabilities within the CUF-Explicit framework. In particular, a detailed overview of the CODAM2 material model was provided, based on continuum damage mechanics, for the progressive damage analysis of

unidirectional carbon-fibre reinforced composites loaded in tension and in compression. The CODAM2 model was implemented in the CUF-Explicit numerical framework in combination with higher-order layer-wise 2D structural models, and a series of numerical assessments was performed for the verification and validation of the numerical framework. The proposed framework was capable of predicting progressive damage and post-peak softening in compact tension and compression specimens, and the results were in good agreement with experimental data. A series of notched specimens were also tested in tension and compression, and the predicted laminate failure strength was in excellent agreement with experiments. The CUF models were also able to predict size-effects in line with experimental observations. The relaxed aspect-ratio constraints of CUF structural theories enabled the scaling of the discretisation along with the specimen geometry, leading to constant computational costs for increasing laminate size, in the case of notched specimens under tension. For the case of compressive damage modelling, linear-brittle fibre post-peak softening models were used to account for the effects of fibre micro-buckling and kinking. It was observed that the linear-brittle model with 30% residual stress values with respect to the peak stress, i.e. the Br-30 softening law, was the optimised value for the IM7/8552 material system, and numerical simulations based on this value resulted in predictions which were in closest agreement to experiments.
Chapter 6 presented a series of verification and validation cases to demonstrate the capability of the CUF-Explicit framework in accurately solving problems related to low-velocity impact of multilayered structures. 2D layer-wise models based on higher-order CUF theories were used in the analysis, where each ply was individually modelled using thickness functions based on Lagrange polynomials. The first numerical case was the linear impact analysis of a composite laminated plate, and the 3D stress fields obtained by the CUF models were compared to reference 3D-FE solutions. It was shown that the use of the proposed approach leads to a multi-fold reduction in the analysis time, and a two order-of-magnitude reduction in the computational size of the problem, when compared to 3D-FEA. The elastoplastic analysis of a bimetallic plate was then carried out, and the computational efficiency of layer-wise CUF models was demonstrated for impact assessments involving physical nonlinearities. Finally, the progressive damage analysis of a composite laminate was performed, and the results were validated with available experimental and numerical data from the literature. The CUF virtual testing platform was thus shown to be capable of handling problems involving low-velocity impact in a computationally efficient manner.
The major conclusions drawn from the results of progressive damage and impact analysis of laminated structures using layer-wise 2D-CUF models are enumerated as follows:

1. 2D-CUF models perform very well in predicting progressive damage and failure in composite laminates, and the framework is validated using experimental results.

2. The proposed CUF platform for impact analysis is demonstrated to accurately predict the response of multilayered laminates under impact loads, and is verified using 3D-FE simulation, for elastic impact as well as problems involving physical nonlinearities.

3. 2D-CUF models demonstrate good predictive accuracy in the global progressive damage response of composites subjected to low-velocity impact, and are also capable of correctly evaluating localised intra- and interlaminar damage in the impact region, whose morphology is consistent with experimental observations.

4. A relaxation of aspect-ratio constraints enables the use of large-sized elements to discretise the in-plane structural geometry, compared to 3D solid finite elements, resulting in a significant improvement of the computational efficiency.

5. The capability of 2D-CUF models in accurately evaluating 3D strain and stress fields is fundamental in obtaining accurate numerical results which correlate well with experimental data.

6. The layer-wise approach allows for the use of different polynomial orders to model the thickness of composite laminates, allowing for the freedom of choosing the appropriate thickness function for a specific problem. In particular, higher-order thickness functions are important for the accurate evaluation of interlaminar stress fields in composites subjected to bending under the influence of impact loads, whereas linear thickness functions are sufficient for the progressive damage analysis of in-plane loaded composites.

Scope for future investigations

The present work developed a numerical framework which combines various capabilities such as continuum intralaminar damage models, interface elements based on cohesive formulations, and contact discretisation and enforcement techniques - within the context of explicit time integration schemes - towards the low-velocity impact analysis of composite laminates. The numerical platform can be used, and extended, to explore a variety of research avenues. Some topics which could be considered for future investigations are listed as follows:

1. Extending low-velocity impact analysis to compression after impact (CAI) of composite laminates.

2. Development of multiscale techniques for the high-fidelity impact analysis of fibre-reinforced composites.

3. Development of adaptive methodologies for the insertion of cohesive elements in localised regions to reduce computational costs of the overall analysis.

4. Applying the global-local framework to the progressive damage analysis of composites, and developing a two-way coupling approach to account for local stiffness degradation.

References

[1] Abir, M., Tay, T., Ridha, M., and Lee, H. (2017). Modelling damage growth in composites subjected to impact and compression after impact. *Composite Structures*, 168:13–25.

[2] Akterskaia, M., Jansen, E., Hallett, S., Weaver, P., and Rolfes, R. (2019). Progressive failure analysis using global-local coupling including intralaminar failure and debonding. *AIAA Journal*, pages 3078–3089.

[3] Anderson, T. and Madenci, E. (2000). Experimental investigation of low-velocity impact characteristics of sandwich composites. *Composite structures*, 50(3):239–247.

[4] Barenblatt, G. I. (1962). The mathematical theory of equilibrium cracks in brittle fracture. *Advances in applied mechanics*, 7(1):55–129.

[5] Bathe, K.-J. (2006). *Finite element procedures*. Klaus-Jurgen Bathe.

[6] Bažant, Z. P. and Oh, B. H. (1983). Crack band theory for fracture of concrete. *Matériaux et construction*, 16(3):155–177.

[7] Belgacem, F., Hild, P., and Laborde, P. (1997). Approximation of the unilateral contact problem by the mortar finite element method. *Comptes Rendus de l'Academie des Sciences Series I Mathematics*, 324(1):123–127.

[8] Benson, D. and Hallquist, J. (1990). A single surface contact algorithm for the post-buckling analysis of shell structures. *Computer Methods in Applied Mechanics and Engineering*, 78(2):141–163.

[9] Bharati, R. B., Filippi, M., Mahato, P. K., and Carrera, E. (2020). Flutter analysis of laminated composite structures using carrera unified formulation. *Composite Structures*, 253:112759.

[10] Bisagni, C., Vescovini, R., and Dávila, C. G. (2011). Single-stringer compression specimen for the assessment of damage tolerance of postbuckled structures. *Journal of Aircraft*, 48(2):495–502.

[11] Bouvet, C., Castanié, B., Bizeul, M., and Barrau, J. (2009). Low velocity impact modelling in laminate composite panels with discrete interface elements. *International Journal of Solids and Structures*, 46(14-15):2809–2821.

[12] Bouvet, C., Rivallant, S., and Barrau, J. (2012). Low velocity impact modeling in composite laminates capturing permanent indentation. *Composites Science and Technology*, 72(16):1977–1988.

[13] Brewer, J. C. and Lagace, P. A. (1988). Quadratic stress criterion for initiation of delamination. *Journal of composite materials*, 22(12):1141–1155.

[14] Camanho, P. P., Davila, C. G., and De Moura, M. (2003). Numerical simulation of mixed-mode progressive delamination in composite materials. *Journal of composite materials*, 37(16):1415–1438.

[15] Camanho, P. P., Maimí, P., and Dávila, C. G. (2007). Prediction of size effects in notched laminates using continuum damage mechanics. *Composites science and technology*, 67(13):2715–2727.

[16] Cantwell, W. and Morton, J. (1989). Comparison of the low and high velocity impact response of CFRP. *Composites*, 20(6):545–551.

[17] Caputo, F., De Luca, A., Lamanna, G., Lopresto, V., and Riccio, A. (2015). Numerical investigation of onset and evolution of LVI damages in carbon–epoxy plates. *Composites Part B: Engineering*, 68:385–391.

[18] Carpenter, N., Taylor, R., and Katona, M. (1991). Lagrange constraints for transient finite element surface contact. *International journal for numerical methods in engineering*, 32(1):103–128.

[19] Carrera, E. (1995). A class of two dimensional theories for multilayered plates analysis, atti accademia delle scienze di torino. *Mem Sci Fis*, 19:49–87.

[20] Carrera, E. (2003). Theories and finite elements for multilayered plates and shells: a unified compact formulation with numerical assessment and benchmarking. *Archives of Computational Methods in Engineering*, 10(3):215–296.

[21] Carrera, E., Cinefra, M., Petrolo, M., and Zappino, E. (2014). *Finite element analysis of structures through unified formulation*. John Wiley & Sons.

[22] Carrera, E., Filippi, M., and Zappino, E. (2013). Laminated beam analysis by polynomial, trigonometric, exponential and zig-zag theories. *European Journal of Mechanics-A/Solids*, 41:58–69.

[23] Carrera, E. and Giunta, G. (2010). Refined beam theories based on a unified formulation. *International Journal of Applied Mechanics*, 2(01):117–143.

[24] Carrera, E., Giunta, G., Nali, P., and Petrolo, M. (2010). Refined beam elements with arbitrary cross-section geometries. *Computers & structures*, 88(5-6):283–293.

[25] Carrera, E., Guarnera, D., and Pagani, A. (2018). Static and free-vibration analyses of dental prosthesis and atherosclerotic human artery by refined finite element models. *Biomechanics and modeling in mechanobiology*, 17(2):301–317.

[26] Carrera, E., Kaleel, I., and Petrolo, M. (2019). Elastoplastic analysis of compact and thin-walled structures using classical and refined beam finite element models. *Mechanics of advanced materials and structures*, 26(3):274–286.

[27] Carrera, E. and Nali, P. (2010). Multilayered plate elements for the analysis of multifield problems. *Finite Elements in Analysis and Design*, 46(9):732–742.

[28] Carrera, E. and Petrolo, M. (2012). Refined beam elements with only displacement variables and plate/shell capabilities. *Meccanica*, 47(3):537–556.

[29] Cesnik, C. E. and Hodges, D. H. (1997). Vabs: a new concept for composite rotor blade cross-sectional modeling. *Journal of the American helicopter society*, 42(1):27–38.

[30] Chen, B. Y., Pinho, S. T., de Carvalho, N. V., Baiz, P. M., and Tay, T. E. (2014). A floating node method for the modelling of discontinuities in composites. *Engineering Fracture Mechanics*, 127:104–134.

[31] Choi, H., Downs, R., and Chang, F. (1991). A new approach toward understanding damage mechanisms and mechanics of laminated composites due to low-velocity impact: Part I—experiments. *Journal of Composite Materials*, 25(8):992–1011.

[32] Cinefra, M., Petrolo, M., Li, G., and Carrera, E. (2017). Variable kinematic shell elements for composite laminates accounting for hygrothermal effects. *Journal of Thermal Stresses*, 40(12):1523–1544.

[33] Council, N. R. et al. (2008). *Integrated computational materials engineering: a transformational discipline for improved competitiveness and national security*. National Academies Press.

[34] de Borst, R., Crisfield, M. A., Remmers, J. J. C., and Verhoosel, C. V. (2012). *Nonlinear finite element analysis of solids and structures*. John Wiley & Sons.

[35] de Miguel, A., Kaleel, I., Nagaraj, M., Pagani, A., Petrolo, M., and Carrera, E. (2018). Accurate evaluation of failure indices of composite layered structures via various fe models. *Composites Science and Technology*, 167:174–189.

[36] De Moura, M. and Gonçalves, J. (2004). Modelling the interaction between matrix cracking and delamination in carbon–epoxy laminates under low velocity impact. *Composites Science and Technology*, 64(7-8):1021–1027.

[37] Demirbas, M. D., Caliskan, U., Xu, X., and Filippi, M. (2020). Evaluation of the bending response of compact and thin-walled fg beams with cuf. *Mechanics of Advanced Materials and Structures*, pages 1–10.

[38] D'Mello, R. J., Waas, A. M., Maiaru, M., and Koon, R. (2020). Integrated computational modeling for efficient material and process design for composite aerospace structures. In *AIAA Scitech 2020 Forum*, page 0655.

[39] Duarte, C. A. and Kim, D.-J. (2008). Analysis and applications of a generalized finite element method with global–local enrichment functions. *Computer Methods in Applied Mechanics and Engineering*, 197(6):487–504.

[40] Dugdale, D. S. (1960). Yielding of steel sheets containing slits. *Journal of the Mechanics and Physics of Solids*, 8(2):100–104.

[41] Euler, L. (1744). *Methodus inveniendi lineas curvas maximi minimive proprietate gaudentes*. apud Marcum-Michaelem Bousquet.

[42] Feng, D. and Aymerich, F. (2014). Finite element modelling of damage induced by low-velocity impact on composite laminates. *Composite Structures*, 108:161–171.

[43] Filippi, M. and Carrera, E. (2016a). Aerodynamic and mechanical hierarchical aeroelastic analysis of composite wings. *Mechanics of Advanced Materials and Structures*, 23(9):997–1004.

[44] Filippi, M. and Carrera, E. (2016b). Capabilities of 1d cuf-based models to analyse metallic/composite rotors. *Advances in aircraft and spacecraft science*, 3(1):001.

[45] Filippi, M. and Carrera, E. (2017). Dynamic analyses of axisymmetric rotors through three-dimensional approaches and high-fidelity beam theories. *Journal of Vibration and Acoustics*, 139(6).

[46] Filippi, M., Carrera, E., and Zenkour, A. (2015). Static analyses of fgm beams by various theories and finite elements. *Composites Part B: Engineering*, 72:1–9.

[47] Fischer, K. and Wriggers, P. (2005). Frictionless 2d contact formulations for finite deformations based on the mortar method. *Computational Mechanics*, 36(3):226–244.

[48] Flightpath, A. (2011). 2050-europe's vision for aviation. *Advisory Council for Aeronautics Research in Europe*.

[49] Forghani, A., Poursartip, A., and Vaziri, R. (2019). An orthotropic non-local approach to modeling intra-laminar damage progression in laminated composites. *International Journal of Solids and Structures*, 180:160–175.

[50] Forghani, A., Zobeiry, N., Poursartip, A., and Vaziri, R. (2013). A structural modelling framework for prediction of damage development and failure of composite laminates. *Journal of Composite Materials*, 47(20-21):2553–2573.

[51] Francavilla, A. and Zienkiewicz, O. (1975). A note on numerical computation of elastic contact problems. *International Journal for Numerical Methods in Engineering*, 9(4):913–924.

[52] Friedlingstein, P., Jones, M., O'sullivan, M., Andrew, R., Hauck, J., Peters, G., Peters, W., Pongratz, J., Sitch, S., Le Quéré, C., et al. (2019). Global carbon budget 2019. *Earth System Science Data*, 11(4):1783–1838.

[53] Frizzell, R., McCarthy, C., and McCarthy, M. (2011). Simulating damage and delamination in fibre metal laminate joints using a three-dimensional damage model with cohesive elements and damage regularisation. *Composites Science and Technology*, 71(9):1225–1235.

[54] Gendre, L., Allix, O., Gosselet, P., and Comte, F. (2009). Non-intrusive and exact global/local techniques for structural problems with local plasticity. *Computational Mechanics*, 44(2):233–245.

[55] Glaessgen, E. and Stargel, D. (2012). The digital twin paradigm for future nasa and us air force vehicles. In *53rd AIAA/ASME/ASCE/AHS/ASC structures, structural dynamics and materials conference 20th AIAA/ASME/AHS adaptive structures conference 14th AIAA*, page 1818.

[56] Gonçalves, R. and Camotim, D. (2011). Generalised beam theory-based finite elements for elastoplastic thin-walled metal members. *Thin-Walled Structures*, 49(10):1237–1245.

[57] Gonçalves, R. and Camotim, D. (2012). Geometrically non-linear generalised beam theory for elastoplastic thin-walled metal members. *Thin-walled structures*, 51:121–129.

[58] González, E., Maimí, P., Camanho, P., Turon, A., and Mayugo, J. (2012). Simulation of drop-weight impact and compression after impact tests on composite laminates. *Composite Structures*, 94(11):3364–3378.

[59] Graver, B., Zhang, K., and Rutherford, D. (2019). Co2 emissions from commercial aviation, 2018. *The International Council of Clean Transportation*.

[60] Gruttmann, F. and Wagner, W. (2001). Shear correction factors in timoshenko's beam theory for arbitrary shaped cross-sections. *Computational mechanics*, 27(3):199–207.

[61] Hallett, S. R., Jiang, W., Khan, B., and Wisnom, M. R. (2008). Modelling the interaction between matrix cracks and delamination damage in scaled quasi-isotropic specimens. *Composites Science and Technology*, 68(1):80–89.

[62] Hallquist, J., Goudreau, G., and Benson, D. (1985). Sliding interfaces with contact-impact in large-scale lagrangian computations. *Computer methods in applied mechanics and engineering*, 51(1-3):107–137.

[63] Harris, C. E. (2001). *An assessment of the state-of-the-art in the design and manufacturing of large composite structures for aerospace vehicles*. National Aeronautics and Space Administration, Langley Research Center.

[64] Hashin, Z. (1980). Failure criteria for unidirectional fiber composites. *Journal of applied mechanics*, 47(2):329–334.

[65] Iarve, E. V., Hoos, K. H., Nikishkov, Y., and Makeev, A. (2018). Discrete damage modeling of static bearing failure in laminated composites. *Composites Part A: Applied Science and Manufacturing*, 108:30–40.

[66] International Civil Aviation Organization (ICAO) (2018). The world of air transport in 2018.

[67] Jin, S., Sohn, D., and Im, S. (2016). Node-to-node scheme for three-dimensional contact mechanics using polyhedral type variable-node elements. *Computer Methods in Applied Mechanics and Engineering*, 304:217–242.

[68] Kaddour, A. S., Hinton, M. J., Smith, P. A., and Li, S. (2013). Mechanical properties and details of composite laminates for the test cases used in the third world-wide failure exercise. *Journal of Composite Materials*, 47(20-21):2427–2442.

[69] Kaleel, I., Carrera, E., and Petrolo, M. (2020). Progressive delamination of laminated composites via 1d models. *Composite Structures*, 235:111799.

[70] Kaleel, I., Petrolo, M., Carrera, E., and Waas, A. (2019a). Computationally efficient concurrent multiscale framework for the linear analysis of composite structures. *AIAA Journal*, 57(9):4019–4028.

[71] Kaleel, I., Petrolo, M., Carrera, E., and Waas, A. (2019b). Computationally efficient concurrent multiscale framework for the nonlinear analysis of composite structures. *AIAA Journal*, 57(9):4029–4041.

[72] Kaleel, I., Petrolo, M., Waas, A., and Carrera, E. (2017). Computationally efficient, high-fidelity micromechanics framework using refined 1d models. *Composite Structures*, 181:358–367.

[73] Kaleel, I., Petrolo, M., Waas, A., and Carrera, E. (2018). Micromechanical progressive failure analysis of fiber-reinforced composite using refined beam models. *Journal of Applied Mechanics*, 85(2).

[74] Kim, D.-J., Duarte, C. A., and Proença, S. P. (2012). A generalized finite element method with global-local enrichment functions for confined plasticity problems. *Computational Mechanics*, 50(5):563–578.

[75] Kim, J., Lim, J., Lee, J., and Im, S. (2008). A new computational approach to contact mechanics using variable-node finite elements. *International journal for numerical methods in engineering*, 73(13):1966–1988.

[76] Kirchhoff, G. (1850). *Über das Gleichgewicht und die Bewegung einer elastischen Scheibe*.

[77] Krueger, R. and Minguet, P. J. (2007). Analysis of composite skin–stiffener debond specimens using a shell/3d modeling technique. *Composite Structures*, 81(1):41–59.

[78] Krueger, R. and O'Brien, T. K. (2001). A shell/3d modeling technique for the analysis of delaminated composite laminates. *Composites Part A: applied science and manufacturing*, 32(1):25–44.

[79] Ladeveze, P. and LeDantec, E. (1992). Damage modelling of the elementary ply for laminated composites. *Composites science and technology*, 43(3):257–267.

[80] Lafarie-Frenot, M. and Touchard, F. (1994). Comparative in-plane shear behaviour of long-carbon-fibre composites with thermoset or thermoplastic matrix. *Composites science and technology*, 52(3):417–425.

[81] Lammerant, L. and Verpoest, I. (1996). Modelling of the interaction between matrix cracks and delaminations during impact of composite plates. *Composites Science and Technology*, 56(10):1171–1178.

[82] Lee, J. and Soutis, C. (2008). Measuring the notched compressive strength of composite laminates: Specimen size effects. *Composites Science and Technology*, 68(12):2359–2366.

[83] Li, G., Carrera, E., Cinefra, M., Zappino, E., and Jansen, E. (2019). Variable kinematic shell formulations accounting for multi-field effects for the analysis of multi-layered structures. In *Advances in Predictive Models and Methodologies for Numerically Efficient Linear and Nonlinear Analysis of Composites*, pages 13–27. Springer.

[84] Li, G., Cinefra, M., and Carrera, E. (2020). Coupled thermo-mechanical finite element models with node-dependent kinematics for multi-layered shell structures. *International Journal of Mechanical Sciences*, 171:105379.

[85] Litewka, P. and Wriggers, P. (2002). Contact between 3d beams with rectangular cross-sections. *International Journal for Numerical Methods in Engineering*, 53(9):2019–2041.

[86] Lopes, C., Seresta, O., Coquet, Y., Gürdal, Z., Camanho, P., and Thuis, B. (2009). Low-velocity impact damage on dispersed stacking sequence laminates. Part i: experiments. *Composites Science and Technology*, 69(7-8):926–936.

[87] Mao, K. and Sun, C. (1991). A refined global-local finite element analysis method. *International journal for numerical methods in engineering*, 32(1):29–43.

[88] Matzenmiller, A., Lubliner, J., and Taylor, R. L. (1995). A constitutive model for anisotropic damage in fiber-composites. *Mechanics of materials*, 20(2):125–152.

[89] McCarthy, R., Haines, G., and Newley, R. (1994). Polymer composite applications to aerospace equipment. *Composites Manufacturing*, 5(2):83–93.

[90] McDevitt, T. and Laursen, T. (2000). A mortar-finite element formulation for frictional contact problems. *International Journal for Numerical Methods in Engineering*, 48(10):1525–1547.

[91] McGregor, C., Zobeiry, N., Vaziri, R., Poursartip, A., and Xiao, X. (2017). Calibration and validation of a continuum damage mechanics model in aid of axial crush simulation of braided composite tubes. *Composites Part A: Applied Science and Manufacturing*, 95:208–219.

[92] Mindlin, R. (1951). Influence of rotatory inertia and shear on flexural motions of isotropic, elastic plates. *J. appl. Mech.*, 18:31–38.

[93] Nagaraj, M., Carrera, E., and Petrolo, M. (2020). Progressive damage analysis of composite laminates subjected to low-velocity impact using 2d layer-wise structural models. *International Journal of Non-Linear Mechanics*, page 103591.

[94] Neto, A., Pimenta, P., and Wriggers, P. (2016). A master-surface to master-surface formulation for beam to beam contact. part i: frictionless interaction. *Computer Methods in Applied Mechanics and Engineering*, 303:400–429.

[95] Noor, A. K. (1986). Global-local methodologies and their application to nonlinear analysis. *Finite Elements in Analysis and Design*, 2(4):333–346.

[96] Nour-Omid, B. and Wriggers, P. (1987). A note on the optimum choice for penalty parameters. *Communications in Applied Numerical Methods*, 3(6):581–585.

[97] Orifici, A. C., Herszberg, I., and Thomson, R. S. (2008). Review of methodologies for composite material modelling incorporating failure. *Composite structures*, 86(1-3):194–210.

[98] Ostergaard, M. G., Ibbotson, A. R., Le Roux, O., and Prior, A. M. (2011). Virtual testing of aircraft structures. *CEAS Aeronautical Journal*, 1(1-4):83.

[99] Pagani, A. and Carrera, E. (2017). Large-deflection and post-buckling analyses of laminated composite beams by carrera unified formulation. *Composite Structures*, 170:40–52.

[100] Pagani, A. and Carrera, E. (2018). Unified formulation of geometrically nonlinear refined beam theories. *Mechanics of Advanced Materials and Structures*, 25(1):15–31.

[101] Palazotto, A. N. (1992). *Nonlinear analysis of shell structures*. Aiaa.

[102] Papadopoulos, P. and Taylor, R. (1992). A mixed formulation for the finite element solution of contact problems. *Computer Methods in Applied Mechanics and Engineering*, 94(3):373–389.

[103] Petrolo, M., Kaleel, I., De Pietro, G., and Carrera, E. (2018a). Wave propagation in compact, thin-walled, layered, and heterogeneous structures using variable kinematics finite elements. *International Journal for Computational Methods in Engineering Science and Mechanics*, 19(3):207–220.

[104] Petrolo, M., Nagaraj, M., Kaleel, I., and Carrera, E. (2018b). A global-local approach for the elastoplastic analysis of compact and thin-walled structures via refined models. *Computers & Structures*, 206:54–65.

[105] Pietropaoli, E. and Riccio, A. (2011). A global/local finite element approach for predicting interlaminar and intralaminar damage evolution in composite stiffened panels under compressive load. *Applied Composite Materials*, 18(2):113–125.

[106] Puso, M. and Laursen, T. (2004). A mortar segment-to-segment contact method for large deformation solid mechanics. *Computer methods in applied mechanics and engineering*, 193(6-8):601–629.

[107] Quéré, C., Andrew, R., Friedlingstein, P., Sitch, S., Hauck, J., Pongratz, J., Pickers, P., Ivar Korsbakken, J., Peters, G., Canadell, J., et al. (2018). Global carbon budget 2018. *Earth System Science Data*, 10(4):2141–2194.

[108] Reddy, J. (1984). A simple higher-order theory for laminated composite plates.

[109] Reddy, J. (1987). A generalization of two-dimensional theories of laminated composite plates. *Communications in applied numerical methods*, 3(3):173–180.

[110] Reddy, J. (2003). *Mechanics of laminated composite plates and shells: theory and analysis*. CRC press.

[111] Reddy, J. and Liu, C. (1985). A higher-order shear deformation theory of laminated elastic shells. *International journal of engineering science*, 23(3):319–330.

[112] Reddy, Y. and Reddy, J. (1993). Three-dimensional finite element progressive failure analysis of composite laminates under axial extension. *Journal of Composites, Technology and Research*, 15(2):73–87.

[113] Reifsnider, K. and Majumdar, P. (2013). Multiphysics stimulated simulation digital twin methods for fleet management. In *54th AIAA/ASME/ASCE/AHS/ASC Structures, Structural Dynamics, and Materials Conference*, page 1578.

[114] Reiner, J. (2016). *A computational investigation of failure modes in hybrid titanium composite laminates*. PhD thesis, The University of Queensland.

[115] Reiner, J., Feser, T., Schueler, D., Waimer, M., and Vaziri, R. (2019). Comparison of two progressive damage models for studying the notched behavior of composite laminates under tension. *Composite Structures*, 207:385–396.

[116] Reiner, J. and Vaziri, R. (2018). Structural analysis of composites with finite element codes: An overview of commonly used computational methods. In Beaumont, P. and Zweben, C., editors, *Comprehensive Composite Materials II*, volume 8, pages 61–84. Oxford: Academic Press.

[117] Reiner, J., Veidt, M., Dargusch, M., and Gross, L. (2017a). A progressive analysis of matrix cracking-induced delamination in composite laminates using an advanced phantom node method. *Journal of Composite Materials*, 51(20):2933–2947.

[118] Reiner, J., Zobeiry, N., and Vaziri, R. (2020). A stacked sublaminate-based damage-plasticity model for simulating progressive damage in composite laminates under impact loading. *Thin-Walled Structures*, 156:107009.

[119] Reiner, J., Zobeiry, N., Vaziri, R., Feser, T., Waimer, M., Schueler, D., and Toso-Pentecôte, N. (2017b). Prediction of damage progression in notched tensile specimens: comparison between two intralaminar damage models. In *VI ECCOMAS Thematic Conference on the Mechanical Response of Composites*. Eindhoven, Netherlands.

[120] Reissner, E. (1945). The effect of transverse shear deformation on the bending of elastic plates. *J. appl. Mech.*, pages A69–A77.

[121] Riccio, A., De Luca, A., Di Felice, G., and Caputo, F. (2014). Modelling the simulation of impact induced damage onset and evolution in composites. *Composites Part B: Engineering*, 66:340–347.

[122] Riccio, A., Sellitto, A., Saputo, S., Russo, A., Zarrelli, M., and Lopresto, V. (2017). Modelling the damage evolution in notched omega stiffened composite panels under compression. *Composites Part B: Engineering*, 126:60–71.

[123] Rivallant, S., Bouvet, C., and Hongkarnjanakul, N. (2013). Failure analysis of cfrp laminates subjected to compression after impact: Fe simulation using discrete interface elements. *Composites Part A: Applied Science and Manufacturing*, 55:83–93.

[124] Rouchon, J. (1990). Certification of large airplane composite structures. In *ICAS Congress Proceedings*, volume 2, pages 1439–1447.

[125] Shahbazi, M. (2017). *An efficient virtual testing framework to simulate the progression of damage in notched composite laminates*. PhD thesis, University of British Columbia.

[126] Shi, Y., Pinna, C., and Soutis, C. (2014). Modelling impact damage in composite laminates: a simulation of intra-and inter-laminar cracking. *Composite Structures*, 114:10–19.

[127] Shi, Y., Swait, T., and Soutis, C. (2012). Modelling damage evolution in composite laminates subjected to low velocity impact. *Composite Structures*, 94(9):2902–2913.

[128] Silvestre, N. and Camotim, D. (2002a). First-order generalised beam theory for arbitrary orthotropic materials. *Thin-Walled Structures*, 40(9):755–789.

[129] Silvestre, N. and Camotim, D. (2002b). Second-order generalised beam theory for arbitrary orthotropic materials. *Thin-Walled Structures*, 40(9):791–820.

[130] Simo, J., Wriggers, P., and Taylor, R. (1985). A perturbed lagrangian formulation for the finite element solution of contact problems. *Computer methods in applied mechanics and engineering*, 50(2):163–180.

[131] Simo, J. C., Wriggers, P., Schweizerhof, K. H., and Taylor, R. L. (1986). Finite deformation post-buckling analysis involving inelasticity and contact constraints. *International journal for numerical methods in engineering*, 23(5):779–800.

[132] Song, K., Li, Y., and Rose, C. (2011). Continuum damage mechanics models for the analysis of progressive failure in open-hole tension laminates. In *52nd AIAA/ASME/ASCE/AHS/ASC Structures, Structural Dynamics and Materials Conference 19th AIAA/ASME/AHS Adaptive Structures Conference 13t*, page 1861.

[133] Stadter, J. and Weiss, R. (1979). Analysis of contact through finite element gaps. *Computers & Structures*, 10(6):867–873.

[134] Su, Z., Tay, T., Ridha, M., and Chen, B. (2015). Progressive damage modeling of open-hole composite laminates under compression. *Composite Structures*, 122:507–517.

[135] Sun, X. and Hallett, S. (2017). Barely visible impact damage in scaled composite laminates: Experiments and numerical simulations. *International Journal of Impact Engineering*, 109:178–195.

[136] Sun, X. C., Wisnom, M. R., and Hallett, S. R. (2016). Interaction of inter-and intralaminar damage in scaled quasi-static indentation tests: Part 2–numerical simulation. *Composite Structures*, 136:727–742.

[137] Swindeman, M. J., Iarve, E. V., Brockman, R. A., Mollenhauer, D. H., and Hallett, S. R. (2013). Strength prediction in open hole composite laminates by using discrete damage modeling. *AIAA journal*, 51(4):936–945.

[138] Tan, W., Falzon, B., Chiu, L., and Price, M. (2015). Predicting low velocity impact damage and Compression-After-Impact (cai) behaviour of composite laminates. *Composites Part A: Applied Science and Manufacturing*, 71:212–226.

[139] Tao, F., Zhang, H., Liu, A., and Nee, A. Y. (2018). Digital twin in industry: State-of-the-art. *IEEE Transactions on Industrial Informatics*, 15(4):2405–2415.

[140] Timmis, A. J., Hodzic, A., Koh, L., Bonner, M., Soutis, C., Schäfer, A. W., and Dray, L. (2015). Environmental impact assessment of aviation emission reduction through the implementation of composite materials. *The International Journal of Life Cycle Assessment*, 20(2):233–243.

[141] Timoshenko, S. (1921). On the correction for shear of the differential equation for transverse vibration of prismatic bars. *Philosophical Magazine Series*, 41:744–746.

[142] Timoshenko, S. and Goodier, J. (1970). *Theory of Elasticity*. McGraw-Hill, New York.

[143] Wang, H. W., Zhou, H. W., Ji, H. W., and Zhang, X. C. (2014). Application of extended finite element method in damage progress simulation of fiber reinforced composites. *Materials & Design*, 55:191–196.

[144] Wang, L., Zheng, C., Luo, H., Wei, S., and Wei, Z. (2015). Continuum damage modeling and progressive failure analysis of carbon fiber/epoxy composite pressure vessel. *Composite Structures*, 134:475–482.

[145] Whitcomb, J. D. (1991). Iterative global/local finite element analysis. *Computers & structures*, 40(4):1027–1031.

[146] Whitcomb, J. D. and Woo, K. (1993). Application of iterative global/local finite-element analysis. part 1: Linear analysis. *International Journal for Numerical Methods in Biomedical Engineering*, 9(9):745–756.

[147] Wiggenraad, J. and Bauld Jr, N. (1993). Global/local interlaminar stress analysis of a grid-stiffened composite panel. *Journal of reinforced plastics and composites*, 12(2):237–253.

[148] Williams, K. V., Vaziri, R., and Poursartip, A. (2003). A physically based continuum damage mechanics model for thin laminated composite structures. *International Journal of Solids and Structures*, 40(9):2267–2300.

[149] Wriggers, P. (2006). *Computational Contact Mechanics*. Springer-Verlag.

[150] Wriggers, P., Rust, W., and Reddy, B. (2016). A virtual element method for contact. *Computational Mechanics*, 58(6):1039–1050.

[151] Wriggers, P. and Simo, J. (1985). A note on tangent stiffness for fully nonlinear contact problems. *Communications in Applied Numerical Methods*, 1(5):199–203.

[152] Wriggers, P. and Zavarise, G. (1997). On contact between three-dimensional beams undergoing large deflections. *Communications in numerical methods in engineering*, 13(6):429–438.

[153] Xu, X., P, A., Sun, X., and Wisnom, M. (2020). An experimental study of scaling effects in notched quasi-isotropic carbon/epoxy laminates under compressive loads. *Composites Part A: Applied Science and Manufacturing*, 137:106029.

[154] Xu, X., Wisnom, M. R., Li, X., and Hallett, S. R. (2015). A numerical investigation into size effects in centre-notched quasi-isotropic carbon/epoxy laminates. *Composites Science and Technology*, 111:32–39.

[155] Xue, J. and Kirane, K. (2020). Proceedings of the american society for composites. In *Thirty-Fifth Technical (Virtual) Conference*, pages 1493–1510.

[156] Yan, Y., Pagani, A., and Carrera, E. (2017). Exact solutions for free vibration analysis of laminated, box and sandwich beams by refined layer-wise theory. *Composite Structures*, 175:28–45.

[157] Yu, W., Volovoi, V., Hodges, D., and Hong, X. (2002). Validation of the variational asymptotic beam sectional analysis. *AIAA journal*, 40(10):2105–2112.

[158] Zappino, E., Cavallo, T., and Carrera, E. (2016). Free vibration analysis of reinforced thin-walled plates and shells through various finite element models. *Mechanics of Advanced Materials and Structures*, 23(9):1005–1018.

[159] Zappino, E., Li, G., and Carrera, E. (2018). Node-dependent kinematic elements for the dynamic analysis of beams with piezo-patches. *Journal of Intelligent Material Systems and Structures*, 29(16):3333–3345.

[160] Zavarise, G. and Wriggers, P. (1998). A segment-to-segment contact strategy. *Mathematical and Computer Modelling*, 28(4-8):497–515.

[161] Zavarise, G. and Wriggers, P. (2000). Contact with friction between beams in 3-d space. *International Journal for Numerical Methods in Engineering*, 49(8):977–1006.

[162] Zobeiry, N., Vaziri, R., and Poursartip, A. (2015). Characterization of strain-softening behavior and failure mechanisms of composites under tension and compression. *Composites Part A: Applied Science and Manufacturing*, 68:29–41.

Appendix A

List of Publications

A.1 Journal articles

1. **Nagaraj, M. H.**, Carrera, E. & Petrolo, M. (2020). Progressive damage analysis of composite laminates subjected to low-velocity impact using 2D layer-wise structural models. *International Journal of Non-Linear Mechanics*, 103591.

2. Carrera, E., Petrolo, M., **Nagaraj, M. H.** & Delicata, M. (2020). Evaluation of the influence of voids on 3D representative volume elements of fiber-reinforced polymer composites using CUF micromechanics. *Composite Structures*, 112833.

3. Qi, L., **Nagaraj, M. H.**, Carrera, E., Gao, C. F. & Petrolo, M. (2020). Numerical analysis of disbonding in sandwich structures using 1D finite elements. *Composite Structures*, 112717.

4. **Nagaraj, M. H.**, Reiner, J., Vaziri, R., Carrera, E. & Petrolo, M. (2020). Progressive damage analysis of composite structures using higher-order layer-wise elements. *Composites Part B: Engineering*, 107921.

5. **Nagaraj, M. H.**, Kaleel, I., Carrera, E. & Petrolo, M. (2020). Nonlinear analysis of compact and thin-walled metallic structures including localized plasticity under contact conditions. *Engineering Structures*, 203, 109819.

6. **Nagaraj, M. H.**, Kaleel, I., Carrera, E. & Petrolo, M. (2020). Contact analysis of laminated structures including transverse shear and stretching. *European Journal of Mechanics-A/Solids*, 80, 103899.

7. Carrera, E., Fiordilino, G. A., **Nagaraj, M. H.**, Pagani, A. & Montemurro, M. (2019). A global/local approach based on CUF for the accurate and efficient analysis of metallic and composite structures. *Engineering Structures*, 188, 188-201.

8. de Miguel, A. G., Kaleel, I., **Nagaraj, M. H.**, Pagani, A., Petrolo, M. & Carrera, E. (2018). Accurate evaluation of failure indices of composite layered structures via various FE models. *Composites Science and Technology*, 167, 174-189.

9. Petrolo, M., **Nagaraj, M. H.**, Kaleel, I. & Carrera, E. (2018). A global-local approach for the elastoplastic analysis of compact and thin-walled structures via refined models. *Computers & Structures*, 206, 54-65.

A.2 Conference Proceedings

1. **Nagaraj M.H.**, Carrera, E., Petrolo, M., "A Multiscale Framework for the Progressive Damage Analysis of Fiber-Reinforced Composites Using a Component-Wise Approach", In: Proceedings of the American Society of Composites Thirty-Fifth Technical Conference, 14-17 September 2020.

2. **Nagaraj M.H.**, Carrera E., Petrolo M., "High-fidelity impact analysis of composite structures using refined structural theories", In: Proceedings of the First European Conference on Crashworthiness of Composite Structures – ECCCS-1, Belfast, UK, 19-21 November 2019.

3. **Nagaraj M.H.**, Reiner J., Vaziri R., Carrera E., Petrolo M., "High-fidelity damage analysis of composites using a ply-based continuum model", In: Proceedings of the XXV International Congress of Aeronautics and Astronautics, AIDAA 2019, Rome, Italy, 9-12 September 2019.

4. **Nagaraj M.H.**, Kaleel I., Carrera E., Petrolo M., "Contact modelling of composite structures using advanced structural theories", In: Proceedings of the XXV International Congress of Aeronautics and Astronautics, AIDAA 2019, Rome, Italy, 9-12 September 2019.

5. Carrera E., Kaleel I., **Nagaraj M.H.**, Petrolo M., "A Global-Local Strategy for the Elastoplastic Analysis of Complex Metallic Structures via Component-Wise Approach", In: Proceedings of ASME 2018 International Mechanical Engineering Congress and Exposition IMECE 2018, Pittsburgh, PA, USA, 9-15 November 2018.

6. Kaleel I., **Nagaraj M.H.**, Petrolo M., Carrera E., Waas A.M., "An efficient multiscale virtual testing platform for composites via component-wise models", In: Proceedings of the American Society for Composites (ASC) 33rd Annual Technical Conference, Seattle, USA, 24-26 September 2018.

7. Carrera E., Kaleel I., **Nagaraj M.H.**, Petrolo M., "A virtual testing framework for the analysis of damage in composite structures", In: Proceedings of the 13th World Congress in Computational Mechanics (WCCM), New York, USA, 22-27 July 2018.

8. Kaleel I., **Nagaraj M.H.**, Petrolo M., Carrera E., "Contact modelling within displacement-based refined one dimensional beam models", In: Proceedings of the First International Conference on Mechanics of Advanced Materials and Structures (ICMAMS), Torino, Italy, 17-20 June 2018.

9. **Nagaraj M.H.**, Kaleel I., Petrolo M., Carrera E., "Global-local techniques for macroscale analysis and key performance indicator evaluation of composite structures", In: Proceedings of the First International Conference on Mechanics of Advanced Materials and Structures (ICMAMS), Torino, Italy, 17-20 June 2018.

10. Kaleel I., de Miguel A.G., **Nagaraj M.H.**, Pagani A., Petrolo M., Carrera E., "A component-wise formulation for virtual testing of composites", In: Proceedings of the First International Conference on Mechanics of Advanced Materials and Structures (ICMAMS), Torino, Italy, 17-20 June 2018.

11. Carrera E., Fiordilino G.A., **Nagaraj M.H.**, Pagani A., Petrolo M., "Nonlinear global/local analysis of composite structures", In: Proceedings of the 6th European Conference on Computational Mechanics (ECCM 6), Glasgow, UK, 11-15 June 2018.

12. Carrera E., Petrolo M., Pagani A., Zappino E., Fiordilino G.A., de Miguel A.G., **Nagaraj M.H.**, Kaleel I., "Local refinement of classical FEM solution using node-dependent kinematics elements", In: Proceedings of the European Conference on Spacecraft Structures, Materials and Environmental Testing - ECSSMET 2018, Noordwijk, The Netherlands, 28 May - 1 June 2018.

13. Carrera E., Cinefra M., Filippi M., Pagani A., Petrolo M., Zappino E., de Miguel A.G., Kaleel I., **Nagaraj M.H.**, Li G., Guarnera D., Viglietti A., Valvano S.. "Advanced numerical methods for failure analysis of metallic and composite aerospace structures Technical Interchange Meeting (TIM) on Fracture Control of Spacecraft, Launchers and their Payloads and Experiments". (2017), ESTEC Noordwijk (Holland), November 2-3, 2017